Mathematical Modeling of the Kinetics of Martensite Transformation and the Thermomechanical Properties of a Low Alloy Medium-Carbon Steel

by

Jia Hong LIU

MANUSCRIPT-BASED THESIS PRESENTED TO ÉCOLE DE TECHNOLOGIE SUPÉRIEURE IN PARTIAL FULFILLMENT FOR THE DEGREE OF DOCTOR OF PHILOSOPHY
Ph.D.

MONTREAL, DECEMBER 1ST, 2023

ÉCOLE DE TECHNOLOGIE SUPÉRIEURE
UNIVERSITÉ DU QUÉBEC

BOARD OF EXAMINERS

THIS THESIS HAS BEEN EVALUATED

BY THE FOLLOWING BOARD OF EXAMINERS

Mr. Mohammad Jahazi, Thesis Supervisor
Department of Mechanical Engineering, École de Technologie Supérieure

Mr. Sègla Jean-Luc Kpodjedo, President of the Board of Examiners
Department of Software and IT Engineering, École de Technologie Supérieure

Mr. Henri Champliaud, Member of the Jury
Department of Mechanical Engineering, École de Technologie Supérieure

Mr. Jacques Lanteigne, External Examiner
Hydro-Québec Research Institute (IREQ)

THIS THESIS WAS PRESENTED AND DEFENDED

IN THE PRESENCE OF A BOARD OF EXAMINERS AND THE PUBLIC

ON NOVEMBER 28TH, 2023

AT ÉCOLE DE TECHNOLOGIE SUPÉRIEURE

ACKNOWLEDGMENTS

The end of this long journey was only possible due to the countless support and guidance from several people for whom I would like to say thanks.

I'd like to express my most sincere gratitude to my thesis supervisor, Prof. Mohammad Jahazi, who welcomed me into the research group and gave me this opportunity to learn under his supervision. The generous help and patience have made this project a unique and enriching experience.

I am also grateful to the members of the NUSAQ project, Prof. Réné Billardon, Prof. Denis Delagnes, Prof. Henri Champliaud, Prof. Antoine Tahan, Jean-Sébastien Lemyre Baron, Morteza Sadeghifar as well as Nicolas Binot for the numerous insightful discussions and feedback which have been a major contributor to the success of this project.

I would like to thank the members of the committee for agreeing to be my examiners, for kindly giving their time for the reading of this thesis and for the comments and suggestions.

Many thanks to all the members of the CM2P research group for the hangouts and humorous conversations over the past few years. Special thanks to Ameth Fall, Mohammad Saadati, Radu Romanica and Prashant Dhondapure for all the technical assistance.

Finally, I would like to thank my entire family for their continuous support and encouragement and to whom I dedicate this thesis.

MODÉLISATION MATHÉMATIQUE DE LA CINÉTIQUE DE TRANSFORMATION MARTENSITIQUE ET DES PROPRIÉTÉS THERMOMÉCANIQUES D'UN ACIER FAIBLEMENT ALLIÉ À MOYEN CARBONE

Jia Hong LIU

RÉSUMÉ

Les processus de traitement thermique sont essentiels pour les aciers afin d'obtenir des propriétés mécaniques souhaitables pour les applications nécessitant des charges mécaniques importantes. Cela est particulièrement vrai pour les entreprises opérant dans l'industrie aérospatiale, où les exigences de performance attendues sont très élevées. Cependant, les traitements thermiques ne sont pas sans effets indésirables. En effet, ils sont également sources de pièces rejetées en raison de l'apparition de distorsions non désirées et non quantifiées dépassant des tolérances souvent très serrées. La présence de distorsions est un problème pour les entreprises car la productivité en souffre, et des coûts supplémentaires peuvent être nécessaires pour couvrir le remplacement des pièces rejetées. La prédiction des distorsions dues à un traitement thermique est également très difficile, car elle fait intervenir plusieurs champs physiques avec une multitude d'interactions qu'il faut évaluer. Pour pouvoir quantifier et prédire ces déformations, la simulation est obligatoire car c'est la méthode la plus rentable par rapport à la pratique par essais et erreurs. Cependant, pour des simulations précises, des données de matériau fiables sont nécessaires. Par conséquent, des expériences doivent être réalisées et des modèles doivent être proposés selon le processus de fabrication actuel de l'entreprise. Pour ce projet, l'objectif principal est de fournir des modèles précis pour la cinétique de transformation de phase et pour les propriétés thermomécaniques d'un acier faiblement allié à moyen carbone utilisé dans la fabrication d'un train d'atterrissage.

La première partie de cette étude se concentre sur la transformation de phase durant une trempe. En raison de la taille industrielle du composant avec une géométrie complexe et différentes épaisseurs, une distribution non uniforme de la température est observée. Cela conduit également à une transformation de phase non uniforme se produisant à différents moments et à différentes vitesses pendant tout le processus de trempe. Pour mieux comprendre l'évolution de la microstructure, la transformation de phase a été caractérisée par dilatométrie. La transformation de phase en cours peut être simplement observée par le changement de dilatation. Différentes vitesses de refroidissement sont également utilisées sous la température de début de transformation martensitique, représentant mieux les conditions de trempe d'un train d'atterrissage. Les résultats ont montré une décélération significative de la transformation qui décroit davantage avec la diminution des taux de refroidissement. Ce comportement rarement documenté a été attribué au partitionnement du carbone de la martensite fraîche vers l'austénite restante pendant l'auto-revenu.

Suite à cette observation, un nouveau modèle mathématique est proposé sous la forme d'une routine. Bien qu'il existe déjà quelques modèles pour la prédiction des transformations de phase martensitiques, ils sont incapables de décrire avec précision la décélération. Dans le présent

modèle, des équations décrivant les différents mécanismes présents lors de la transformation sont implémentées. La fraction de martensite est décrite par l'équation de Koistinen-Marburger. Cependant, en raison du mécanisme sous-jacent du partitionnement du carbone, la vitesse de transformation est affectée et diminue avec l'augmentation de la concentration de carbone dans l'austénite restante. L'avantage du modèle proposé est mis en évidence par sa capacité à prédire les fractions instantanées de martensite pour une vaste gamme de chemins de refroidissement car il ne dépend que des paramètres du matériau.

La deuxième partie du projet couvre l'ensemble des étapes de la détermination des propriétés thermo-mécaniques de l'austénite et de la martensite pour la gamme de température du processus de trempe, 25°C à 875°C. Les principales propriétés mécaniques sont le module d'Young, la contrainte visqueuse, la contrainte de durcissement cinématique, la contrainte de durcissement isotrope et la limite d'élasticité mathématique. Les expériences sont menées sur le Gleeble et, comme dans la section précédente, des modèles sont proposés pour les propriétés extraites.

Mots-clés: Acier Faiblement Allié à Moyen Carbone, Traitement Thermique, Dilatométrie, Martensite, Diffusion, Transformation de Phase, Partitionnement du Carbone, Modélisation, Propriétés thermomécaniques, Contraintes Mécaniques, Plasticité de Transformation

MATHEMATICAL MODELING OF THE KINETICS OF MARTENSITE TRANSFORMATION AND THE THERMOMECHANICAL PROPERTIES OF A LOW ALLOY MEDIUM-CARBON STEEL

Jia Hong LIU

ABSTRACT

Heat treatment processes are essential for steels in order to achieve desirable mechanical properties for applications requiring important mechanical loadings. This is especially true for companies operating in the aerospace industry where the expected performance requirements are very high. However, heat treatments are not without detrimental effects. Indeed, they are also sources of rejected parts due to the introduction of unwanted and unquantified distortions exceeding tolerances that are often very tight. The presence of distortions is a problem for companies because productivity suffers, and additional costs may be needed to cover for the replacement of rejected parts. The prediction of distortions from a heat treatment is also very difficult, because it involves several physical fields with a multitude of interactions that needs to be assessed. To be able to quantify and predict these distortions, simulation is mandatory as it is the most cost-effective method in comparison to the trial-and-error practice. However, for accurate simulations, a reliable material data is required. Therefore, experiments must be caried out and models must be proposed based on the current manufacturing process of the company. For this project, the main objective is to provide accurate models for the kinetics of phase transformation and for the thermo-mechanical properties of a low alloy medium-carbon steel used in the manufacturing of a landing gear.

The first part of this study focuses on the phase transformation of a quenching process. Due to the industrial size of the component with complex geometry and different thicknesses, non-uniform temperature distribution is observed. This also leads to a non-uniform phase transformation occurring at different moments and at different rates during the whole quenching process. For a better understanding of the microstructure evolution, the phase transformation has been characterized by dilatometry. The ongoing phase transformation can simply be observed by the change in dilatation. Different cooling rates are also used under the martensite start temperature, better representing the quenching conditions of a landing gear. The results showed a significant deceleration in the transformation which increases with decreased cooling rates. This rarely documented behaviour has been attributed to the carbon partitioning from fresh martensite to the remaining austenite during auto-tempering.

Following this observation, a new mathematical model is proposed in the form of a routine. Although, there are already some existing models for the prediction of martensitic phase transformations, they are unable to accurately depict the deceleration. In the present model, equations describing the different mechanisms present during the phase transformation are implemented. The fraction of martensite is described by the Koistinen-Marburger equation. However, due to the underlying mechanism of carbon partitioning, the rate of transformation is affected and decreases with increase carbon concentration in the remaining austenite. The benefit of the proposed model is highlighted by its capability to predict the instantaneous

factions of martensite for a wide range of anisothermal cooling routes as it is solely dependent on material parameters.

The second part of the project covers the entire steps for the determination of the thermo-mechanical properties of austenite and martensite for the temperature range of the quenching process, 25°C to 875°C. The main mechanical properties are the Young's modulus, viscous stress, kinematic hardening stress, isotropic hardening stress and the mathematical yield stress. The experiments are conducted on the Gleeble and similarly to the previous section, models are proposed for the material properties extracted.

Keywords: Low Alloy Medium-Carbon Steel, Heat treatment, Dilatometry, Martensite, Diffusion, Phase Transformation, Carbon Partitioning, Modeling, Thermomechanical Properties, Transformation Induced Plasticity

TABLE OF CONTENTS

Page

LIST OF TABLES

Page

LIST OF FIGURES

Page

LIST OF ABBREVIATIONS

CR	Cooling rate
TMM	Thermo-metallo-mechanical
Ms	Martensite start temperature
Mf	Martensite finish temperature
K-M	Koistinen-Marburger
FCC	Face-centered cubic
BCC	Body-centered cubic
BCT	Body-centered tetragonal
TTT	Time-Temperature-Transformation
CCT	Continuous cooling transformation
JMAK	Johnson-Mehl-Avrami-Kolmogorov
CLTE	Coefficient of linear thermal expansion
XRD	X-Ray diffraction
RA	Retained austenite
TRIP	Transformation induced plasticity

INTRODUCTION

Steel is often regarded as the most versatile material for different purposes. The abundance of iron ore available and its low cost are among many factors which contribute to this material's choice as a prime candidate for various applications. For heavy load applications, such as landing gear main fittings, high mechanical properties are required which can be obtained by performing heat treatments. This process, also called a quenching process, is a combination of heating and cooling operations applied to the metal in its solid state With a sufficiently high cooling rate (CR), a metastable and hard phase called martensite is formed which provides the high strength sought (Bhadeshia & Honeycombe, 2006). Steel used in aerospace industries undergoes through several heat treatments in order to achieve the desired mechanical properties.

Although heat treatments are a way for material properties improvement, they are also a source of parts rejection. If no precautions are considered during the design process, the shape and size of the component could be out of match after heat treatment due to the distortions induced. This could lead to additional costs, especially in the aerospace industry where tolerances are strict. Being able to predict these distortions is therefore an essential key for maintaining a high level of competitiveness in that company. However, distortions prediction is difficult, and it is also very costly if it is assessed by trials and errors. For a cheaper alternative, simulations are employed. It's a very complex method as it involves several physical fields and numerous interactions between them.

For an accurate simulation, a complete understanding of the thermal, metallurgical and mechanical fields as well as the mechanisms involved around these fields during a heat treatment process must be established and modeled (Nallathambi, Kaymak, Specht, & Bertram, 2008). Unfortunately, the constitutive models as well as the parameters needed to make such simulations are hardly available or they are unreliable due to the difference in chemical composition. Due to this lack of reliable material data, tests must be conducted, and

mathematical equations must be identified based on the manufacturing process and the need of the company.

Several commercial software packages exist for the simulation of heat treatments: HEARTS, DANTE, DEFORM-HT, SYSWELD and TRAST (Gür & Şimşir, 2012). Most of them were developed in the early 1980's and unfortunately, oftentimes the experimental and simulation results do not always agree. Verification of the constitutive models is also often impractical due to the inaccessibility of the implemented models. This is an issue known as the "black box" nature of some commercial software packages. For this reason, the main goal of the present project is the development of a thermo-metallo-mechanical (TMM) model for finite element implementation. The benefit of having a self-built model ensures that the simulation encompasses the entirety of the phenomenological aspects of a heat treatment, which is not an easy task to verify. Moreover, with easy access to the implemented models, adjustments and improvements to the models can be made in order to extend simulations to other processes such as welding.

The following thesis will be divided into 5 chapters, as detailed below.

Chapter 1 provides a first section on a literature review of the general knowledge regarding the microstructures of steel and the different heat treatment processes. On the second section, the main mechanisms which leads to potential distortions during heat treatment will be discussed. Finally in the last section, the concepts of modeling will be summarized with a list of existing equations commonly used in heat treatment simulations for the prediction of distortions.

Chapter 2 presents an overview of the material studied and characterized in this project, as well as its manufacturing process. A description of each equipment used, and the experimental procedures will be provided allowing a better portrayal of the tests conducted in the following chapters. A review of the fundamentals of dilatometry will be presented as it is an essential method that is primary used in this project for the measurement of phase fractions.

Additionally, the selection of the sample geometries based on the type of mechanical tests will be explained.

Chapter 3 describes the martensitic phase transformation. Using dilatometry, the kinetics of martensite transformation has been assessed. Due to the large-sized component of a landing gear, the high variation in thickness leads to an important uneven cooling, and subsequently, to an uneven phase transformation. Unlike, conventional methods where different CRs are employed from the austenitization temperature, various CRs under the Ms are used instead. This better reflects the actual quenching conditions observed in the company. The results display a deceleration of the kinetics of martensite transformation which is more pronounced as the CR decreases.

Chapter 4 focuses on the modeling of the previously identified kinetics. As the kinetics is influenced by the CRs, conventional method of modeling cannot be applied, such as the usage of Koistinen-Marburger (K-M). Therefore, a series of equations have been devised which determines the fractions of martensite based on the material state instead. This model follows the actual change in carbon concentration in the remaining austenite which affects the Ms and the rate of transformation.

Chapter 5 details the numerous mechanical tests conducted for the acquisition of the thermo-mechanical properties of the investigated steel. As distortion predictions rely heavily on material data, the characterization of the investigated steel is inevitable. The different methodologies used to extract the Young's modulus, the viscous stress, the kinematic hardening stress, the isotropic hardening stress and the mathematical yield stress will be presented. Additionally, models will be provided for the prediction of the temperature-dependent mechanical parameters.

Annex A follows up on the modeling of the strain rates from the modeled kinetics of martensite transformation of Chapter 4. Ultimately, the prediction of distortions depends on

the strain rates. Therefore, the modeled kinetics are converted into strain rates using the volumetric change from the austenite-martensite transformation.

CHAPTER 1

LITERATURE REVIEW

1.1 Phase Transformations Overview

In order to discuss phase transformations, it is important to introduce the iron-carbon diagram as shown in Figure 1.1. It is an incomplete diagram which covers carbon concentrations up to 6.7 %, corresponding to the composition of cementite. This diagram shows the equilibrium phases present at different temperatures. For steel, the portion of interest in the diagram rests around the eutectoid point and with carbon content lower than 2.11%. At higher carbon concentration, the material would not be considered steel but cast irons.

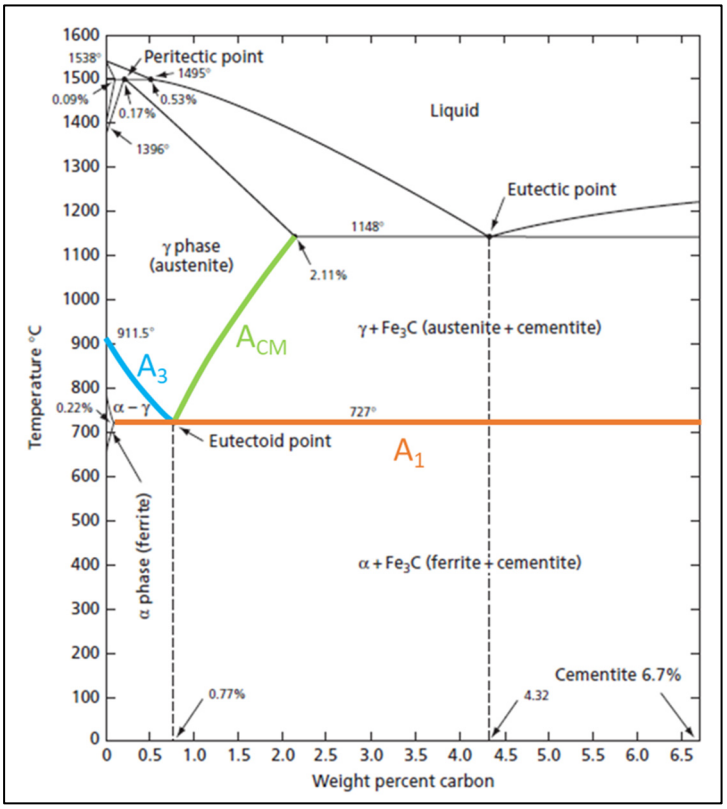

Figure 1.1 Iron-carbon phase diagram
Adapted from Chipman (1972, p. 56)

For pure iron, during heating and upon reaching temperatures higher than 911.5 °C, a crystal structure called face-centered cubic structure (FCC) is formed. At lower temperature, the crystal structure at lower temperature is the body-centered cubic crystal (BCC). These structures are also known as the phases austenite (γ), and ferrite (α), respectively. There's another phase (δ) with similar structure to ferrite but only appears at temperature ranges above 1396 °C and under 1538 °C which is the melting point (Bhadeshia & Honeycombe, 2017). This volume change is the key element for the determination of the phase fractions by dilatometry, which will be discussed in later sections.

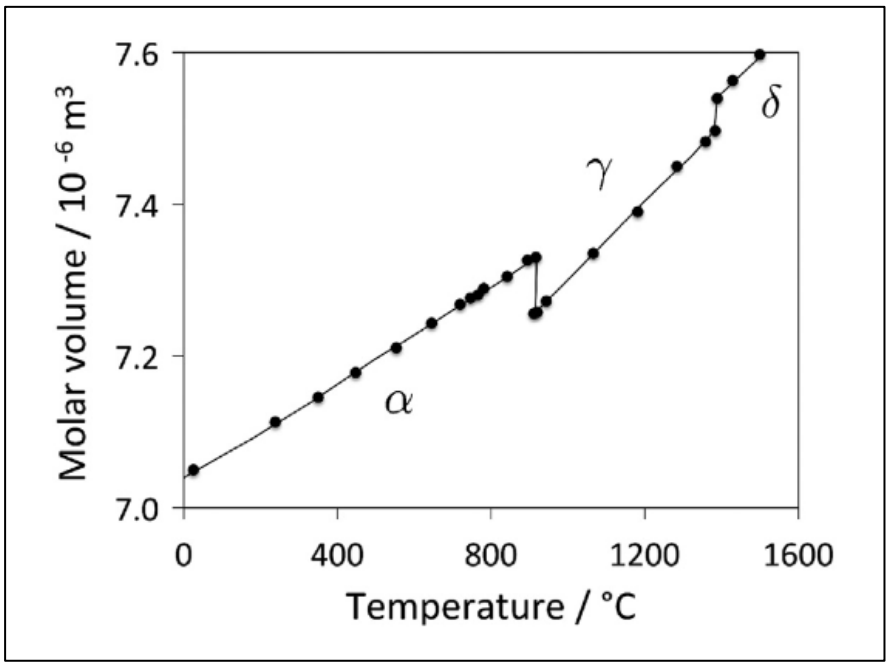

Figure 1.2 Volume change due to phase transformation
Taken from Bhadeshia and Honeycombe (2017, p. 6)

With addition of carbon, the previously identified temperature boundaries changes. For instance, as the carbon concentration increases from 0% to 0.77%, the austenite temperature range decreases. This boundary is also referred as A_3, a separation between γ and γ+α. The lowest point reached for austenite is at 727 °C, corresponding to the eutectoid point. At carbon concentrations higher than this point and until 2.11%, there's another boundary, A_{CM}, which

separates the γ and Fe_3C, known as cementite. The A_1 boundary represents the lowest temperature at which austenite can be present.

While the phase diagram helps visualize the phases present, it can only be achieved by super slow cooling or under equilibrium cooling conditions. In practice and in most cases of heat treatment applications, the cooling nature does not follow the equilibrium conditions. At higher CRs or under non-equilibrium conditions, different microstructures are produced. This is often intentionally done to acquire desirable mechanical properties. The formation of these microstructures can be classified into two mechanisms, diffusive or displacive.

In the diffusive or reconstructive transformation mechanism, a rearrangement by diffusion of atoms takes place giving birth to a new crystal structure which is different from the parent. This can only be achieved at temperatures where the mobility of the atoms is still possible or at least, at a reasonable rate. As a result of this rearrangement, the composition also changes due to the preferential partitioning of some elements in parent phase and others in the product phase (Soffa & Laughlin, 2014).

As for the displacive or diffusionless transformation mechanism, it occurs by deformation of the parent phase without the diffusion of atoms. This transformation by shear deformation and dilatation is called the invariant plane strain. Such transformation is only possible only at low temperatures as it associated with high strain energy and requires a large driving force. Without any rearrangement of atoms, the composition of the product phase is similar to that of the parent. A schematic illustration of both transformation mechanisms is shown in Figure 1.3.

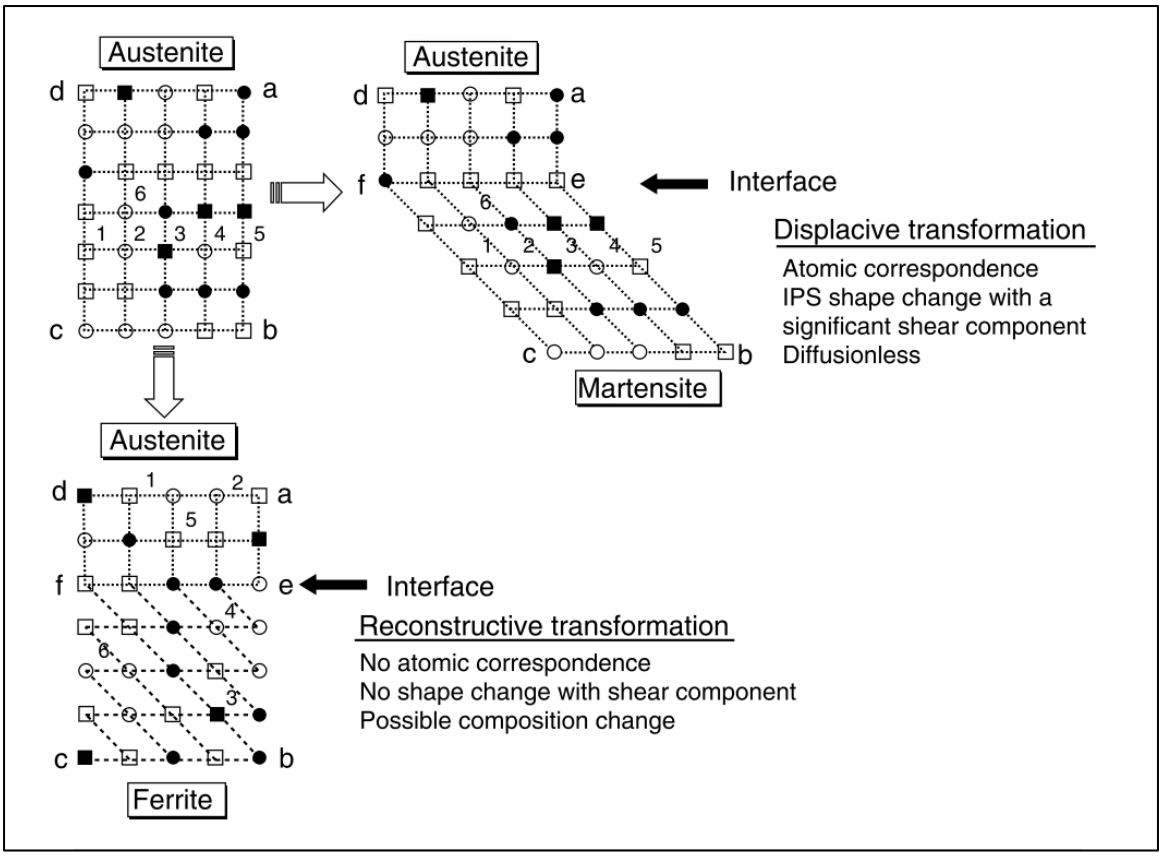

Figure 1.3 Schematic illustration of the reconstructive and displacive mechanisms
Taken from Totten (2007, p. 95)

1.1.1 Ferrite and Pearlite

Upon slow cooling of austenite, ferrite and cementite are formed. At high temperature, when steel is completely austenitized, the solubility in carbon is rather high in comparison to ferrite. When cooled, carbon atoms in the austenite lattice must diffuse due to the lower solubility of ferrite and form cementite.

For steels with carbon concentration lower than 0.77% (hypoeuctectoid steel), slow cooling would initially form ferrite when the temperature reaches the A_3 boundary. The formation of ferrite increases the carbon concentration on the remaining austenite. When the temperature reaches 727 ºC, its carbon concentration in austenite now corresponds to 0.77%, the

concentration at the eutectoid point. Further cooling will now transform from austenite to pearlite (Reed-Hill & Abbaschian, 2009). The final microstructure at room temperature will consist of proeutectoid ferrite and pearlite. Figure 1.4 shows an example of the decomposition of austenite into ferrite and pearlite for a hypoeutectoid steel.

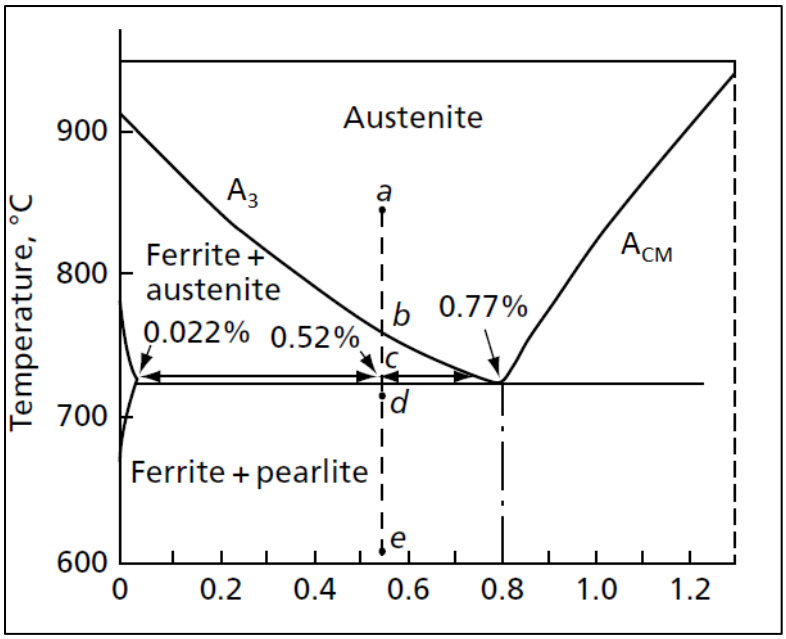

Figure 1.4 Transformation of a hypoeutectoid steel
Taken from Reed-Hill and Abbaschian (2009, p. 594)

On the other hand, if the carbon concentration is higher than 0.77% (hypereutectoid), cementite will form upon reaching the A_{CM} curve. This will decrease the carbon concentration in austenite instead. Therefore, at room temperature, the final microstructure consists of proeutectoid cementite and pearlite.

The morphology of pearlite is a mixture of ferrite and cementite in the form of plates which alternates between them. Decomposition of austenite to pearlite occurs with nucleation at the grain boundaries, and the colony grows until it impinges on adjacent colonies (Advner, 2008). Figure 1.5 shows an example of the microstructure of pearlite.

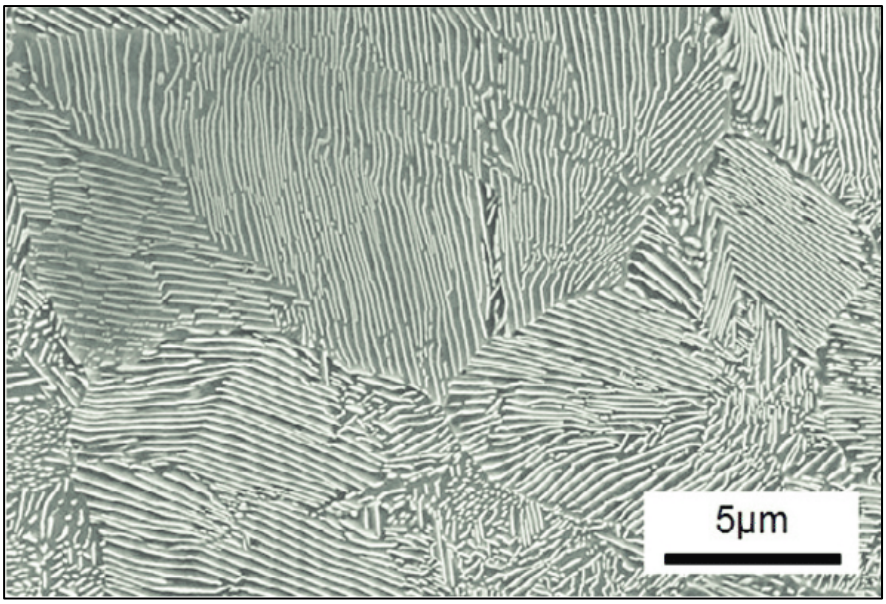

Figure 1.5 Microstructure of pearlite
Taken from Hamada, Sasaki, Ueda, and Noguchi (2011, p. 1468)

1.1.2 Martensite

Martensite is the hardest constituent and is a meta-stable phase which forms athermally at a temperature range constrained by the Ms and the Mf (martensite finish temperature). This means it is dependent on the temperature of undercooling and not influenced by time. The transformation occurs during a quenching process where the CR is sufficiently high enough to avoid the formation of pearlite and bainite (discussed next). It is also a diffusionless transformation, therefore sharing a similar composition with its parent phase, austenite. Carbon atoms are trapped within the FCC structure of austenite from the inability of carbon diffusion due to the high CR. The result of the transformation leads to a body-centered tetragonal (BCT) structure as shown in Figure 1.6 (Pereloma & V. Edmonds, 2012). The degree of tetragonality is also linearly proportional to the carbon content (Pereloma & V. Edmonds, 2012; Porter & Easterling, 2009).

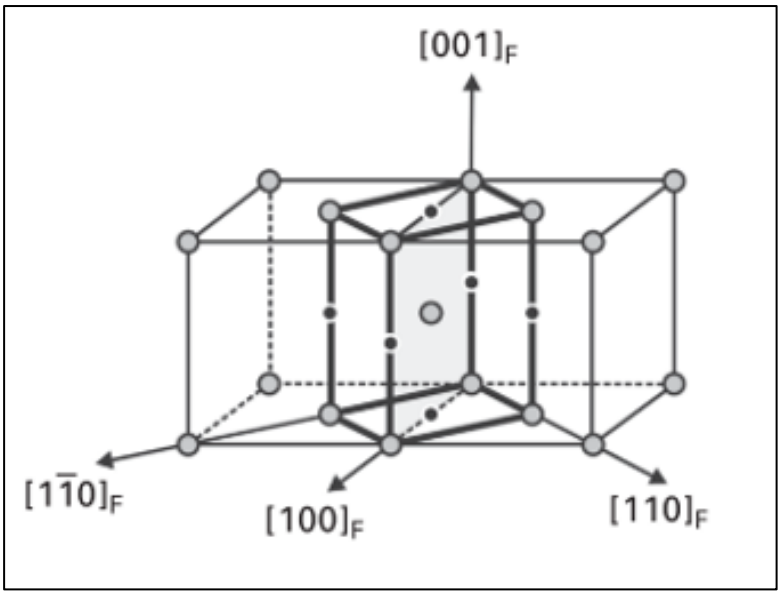

Figure 1.6 BCT structure of martensite shown within 2 FCC structures of austenite
Adapted from Pereloma and V. Edmonds (2012, p. 12)

This highly distorted structure is the main factor that contributes to the high strength of martensite. However, this also accompanied by a poor ductility which makes it brittle. Therefore, tempering processes are required after a quench to improve the toughness. This process reheats the as-quenched steel at temperatures 150-700 °C, below the lower critical temperature, A_1 (Bhadeshia & Honeycombe, 2006).

Two major morphologies are also distinguishable for martensite, lath martensite or plate martensite (Krauss & Marder, 1971). The morphology outcome after quench is related to the carbon concentration of austenite. Generally, the former is obtained with carbon concentrations below 0.6% wt. and as for the latter, at higher concentrations, 0.6-1.8% wt. Figure 1.7 shows a schematic of the observable morphology of martensite as a function of the carbon concentration in austenite.

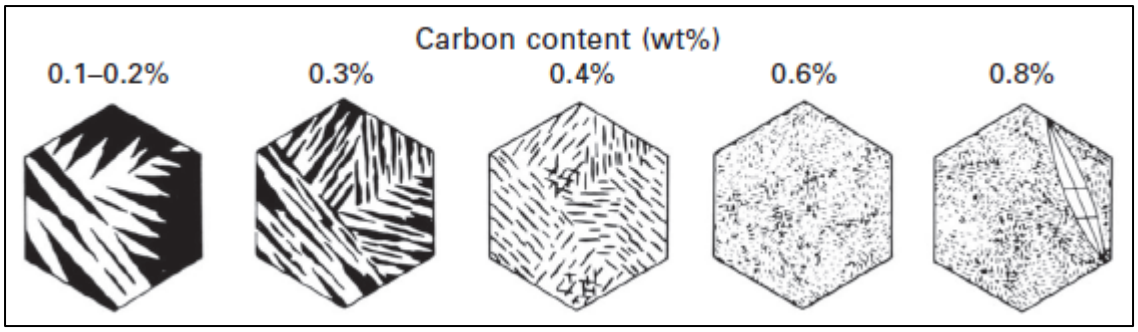

Figure 1.7 Schematic diagram showing a change in microstructure as a function of the carbon concentration
Taken from Pereloma and V. Edmonds (2012, p. 39)

1.1.3 Bainite

Bainite is the name given to the observed microstructure consisting of an "acicular, dark etching aggregate" in honor of E.S. Davenport and E.C. Bain who were first to identify its presence (Bhadeshia, 2015). The microstructure was obtained when heat treated isothermally at a temperature below pearlite and above martensite transformations. Although the microstructure resembles the microstructure of both, pearlite and martensite, it was neither one of them.

Two distinct bainite forms can be observed, the upper and lower bainite during isothermal transformations. Their presence is determined by the temperature of transformation. The former is typically obtained around temperatures between 400 and 550 °C while the latter can be obtained at 250 and 400 °C (Bhadeshia & Honeycombe, 2006). Both, the upper and lower, consists of clusters of laths or aggregates of plates of ferrite called sheaves. Plates, in between sheaves, are called sub-units and share a common crystallographic orientation.

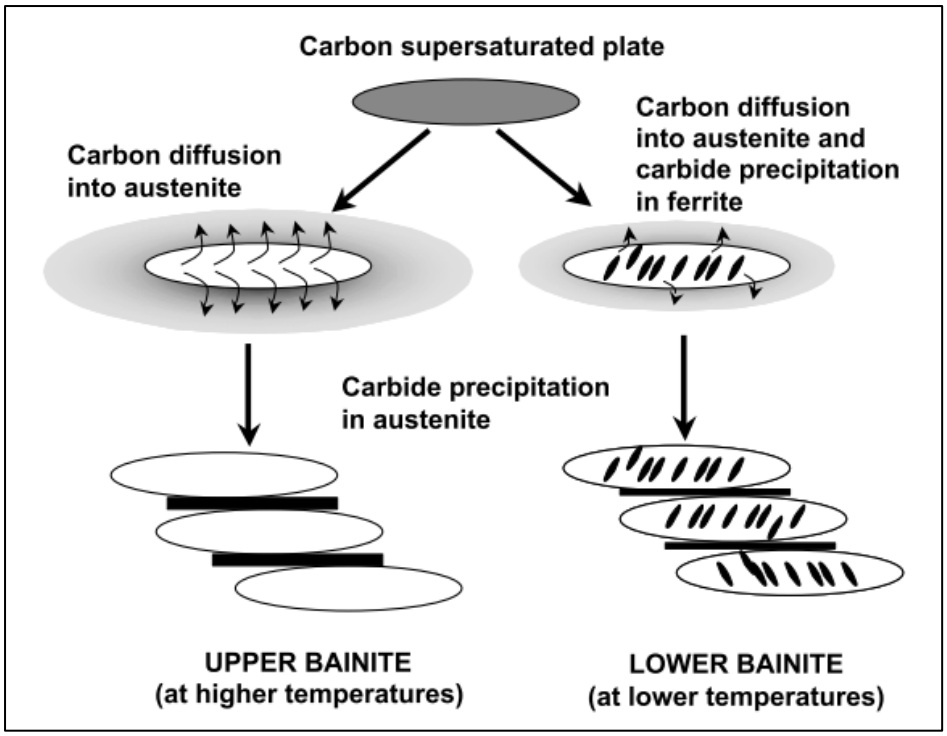

Figure 1.8 Schematic representation of transition between upper and lower bainite
Taken from Takahashi (2004, p. 215)

The classification of upper and lower bainite is usually associated with the location of the carbides in the ferrite matrix as shown in Figure 1.8. It was shown that carbides precipitate from austenite enriched in carbon with the bainite ferrite free of precipitates. At lower temperatures, carbides also precipitate from the enriched austenite but with some carbides precipitating within the ferrite plates (Bhadeshia, 2015).

As for the transformation, there has been some controversy between researchers. For some, the transformation is controlled by diffusion and for others, it's diffusionless (Caballero, Miller, Garcia-Mateo, & Cornide, 2013; Fielding, 2013; Takahashi, 2004). It is now generally accepted that the transformation is diffusionless but with the possibility of carbon to diffuse from the bainitic ferrite into the retained austenite (RA) or precipitate as carbides. The bainitic reaction has similar characteristics of a nucleation and growth process. Sheaves are constructed by the accumulation of sub-units which initially forms at the grain boundary. Once the growth of a sub-unit ends, another one nucleates at its tip and continues the process.

1.1.4 Transformation Diagrams

Figure 1.9 shows a time-temperature-transformation (TTT) diagram, which is used to determine the type of structures, ferrite (α), pearlite, bainite and martensite. The curves indicate the start and the end of transformation of each phase for a given temperature. By plotting the heat treatment cycle or the cooling route over the diagram, it is possible to identify the phase transformed. It is, however, a diagram which is useful for heat treatments which involves isothermal transformations.

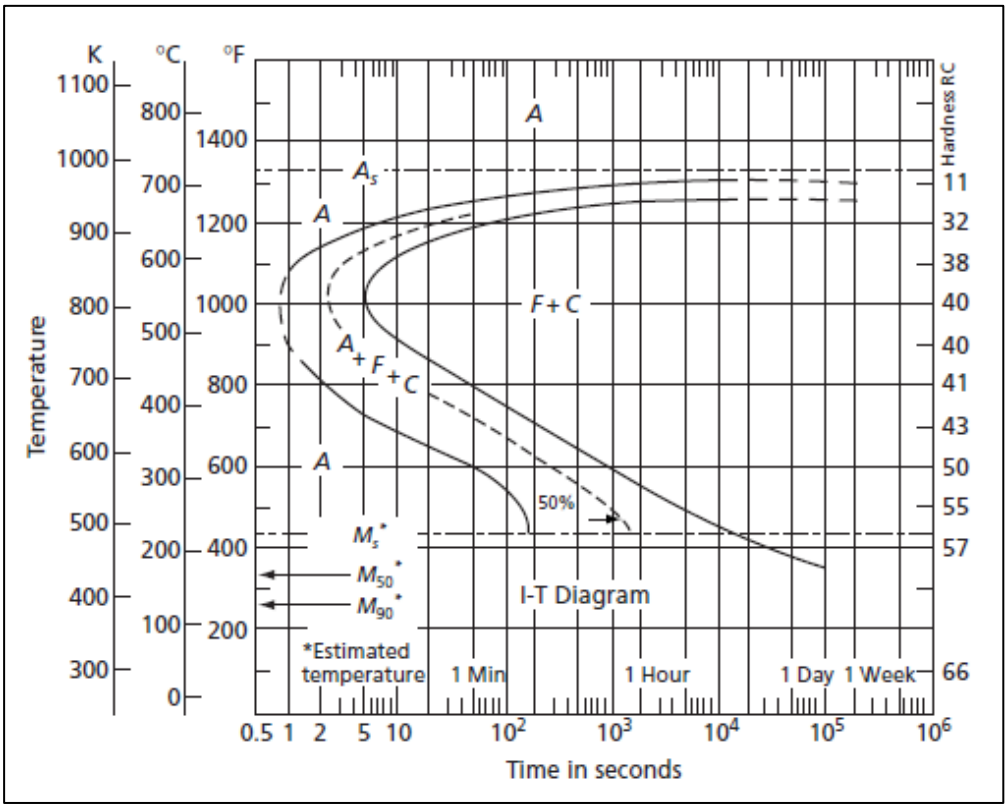

Figure 1.9 Time-temperature-transformation diagram (TTT diagram)
Taken from American Society for Metals (1977, p. 16)

A more appropriate diagram for industrial applications is the continuous cooling transformation (CCT) diagram as illustrated in Figure 1.10. The approach is similar, an overlay

of the cooling route on the diagram would identify the phases obtained. The main difference is instead of holding the temperature for time period, the temperature keeps decreasing. The diagram also enables the determination of a critical CR which is defined as a transformation which would create a purely martensitic steel (Reed-Hill & Abbaschian, 2009).

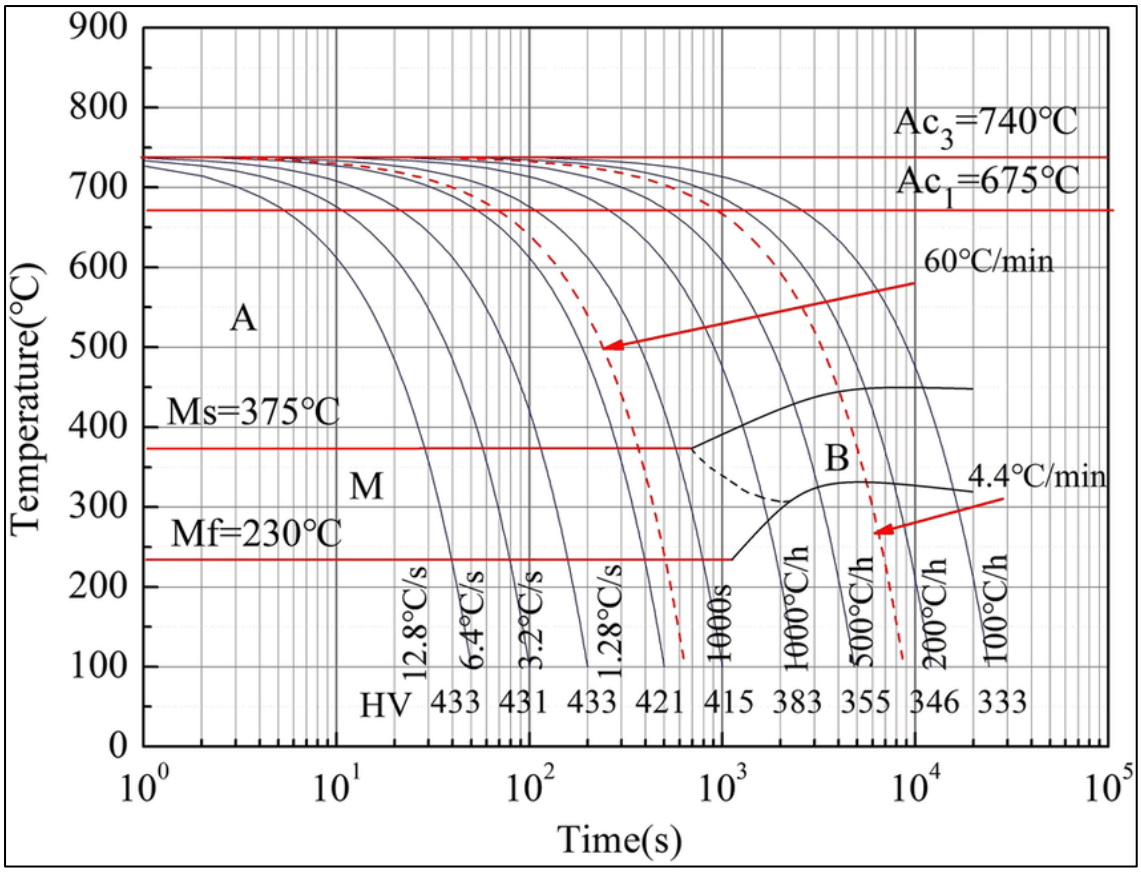

Figure 1.10 Continuous cooling transformation diagram (CCT diagram)
Taken from Z. Yang, Liu, He, Qiao, and Xie (2018, p. 2)

1.2 Distortion Sources and Mechanism

The simulation of a heat treatment is a complex process which involves many physical fields. Although distortions are particularly striking after heat treatment, the source of distortions can also come from any manufacturing processes prior to heat treatment. Every manufacturing step could have a contribution that leads to the change of shape or geometry. Distortions could be

summarised through three basic mechanisms, relief of residual stress, change in volume due to temperature gradient and change in volume due to phase transformation (Totten, 2007).

1.2.1 Relief Residual Stresses

Any metal working processes that is not hot-worked will result in residual stresses within the material, and will remain despite the absence of any external loadings. Such internal stresses are gradually relieved as the material is heated for during annealing or normalisation. However, the material properties, in this case the yield stress, also decrease with the increase of temperature. This leads to the possibility of plastic deformation when the residual stress exceeds the yield stress.

1.2.2 Distortion Induced by Temperature Gradient

Without the implication of any other phenomenon, the high temperature gradient is a high potential source of deformations and internal stresses. After austenitization, the part or the component has a uniform temperature throughout the whole volume. During a quench, the outer surface of the part is in direct contact with a colder environment. This causes a different rate of heat transfer along the section of the part and thus a temperature gradient is observed.

For instance, Figure 1.11 illustrates the representation of residual stresses for a part divided into two sections, the center and the surface (Barralis & Maeder, 1999). Initially, the surface has a lower temperature which implies that it’s contracting. Meanwhile, the center is still at a higher temperature which prevents the surface from contracting, leading to tension stresses at the surface. If the tension stresses surpass the yield stress, then plastic deformation ensues. In turn, the center will start cooling down and eventually contract. It will, however, be prevented by the surface which is now plastically stretched. To maintain compatibility of both sections after the process, the surface must be in compression and the center in tension.

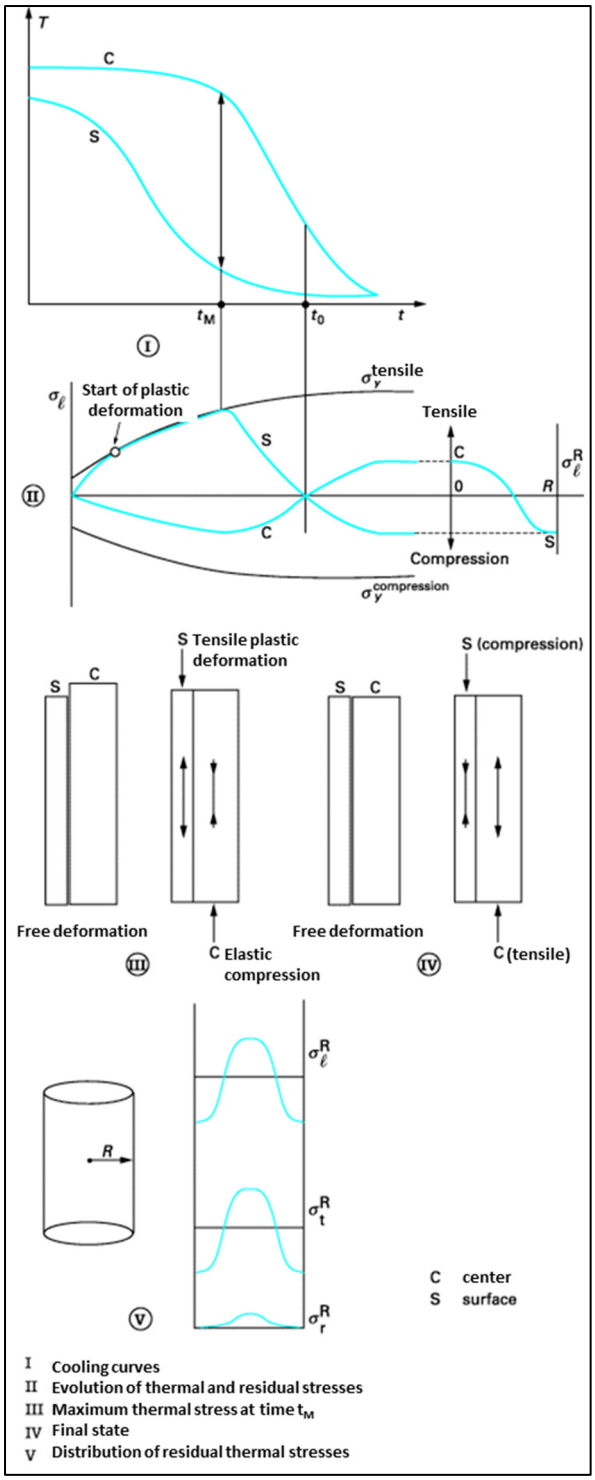

Figure 1.11 Representation of the residual stresses induced by the temperature gradient during a quenching process
Adapted from Barralis and Maeder (1999, p. 18)

1.2.3 Distortion Induced by Phase Transformation

The same approach could be used to explain the source of residual stresses and distortions by correlating volume changes to phase transformation (Barralis & Maeder, 1999; Peterli, Hora, & Volk, 2017; Totten, 2007). In this case, no temperature gradient is involved, and the change of volume is solely dependent on the type of phases obtained. The idea behind a quenching process is the formation of martensite by cooling rapidly the material from the austenite phase.

As previously mentioned, this phase forms when the temperature reaches Ms and with it, a specific volume changes is accompanied (Lement, 1959). Figure 1.12 shows the influence of carbon content on the specific volume of different phases. For any carbon content in a steel, the specific volume of martensite is always higher than the austenite phase.

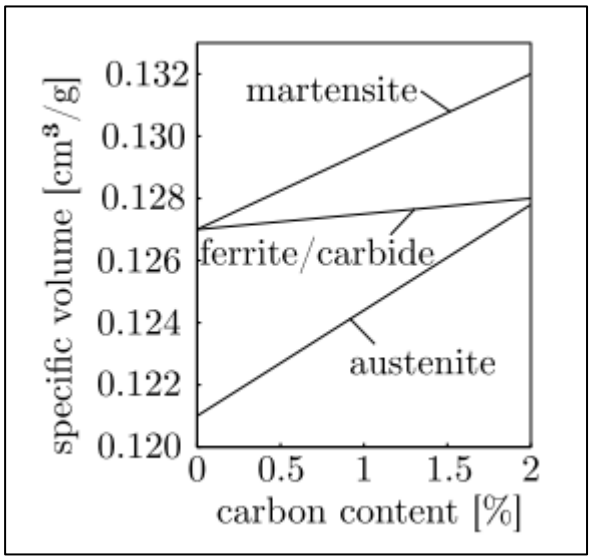

Figure 1.12 Specific volume for various phases as a function of the carbon concentration at room temperature
Taken from Lement (1959, p. 39)

Similarly to the gradient temperature, the surface's temperature decrease at a higher speed in comparison to the temperature at the center. When the temperature reaches the Ms, martensite phase starts to form, and a volume increase is perceived on the surface leading to minimal

compressive stresses as the austenite phase is rather soft as shown in Figure 1.13. As the core temperature reaches the Ms, the volume increases but is prevented by the surface which is now a hard phase. The distribution of residual stresses would then be in tension at the surface and in compressive at the core. The distribution of residual stresses is also in the opposite direction to the residual stresses by temperature gradient.

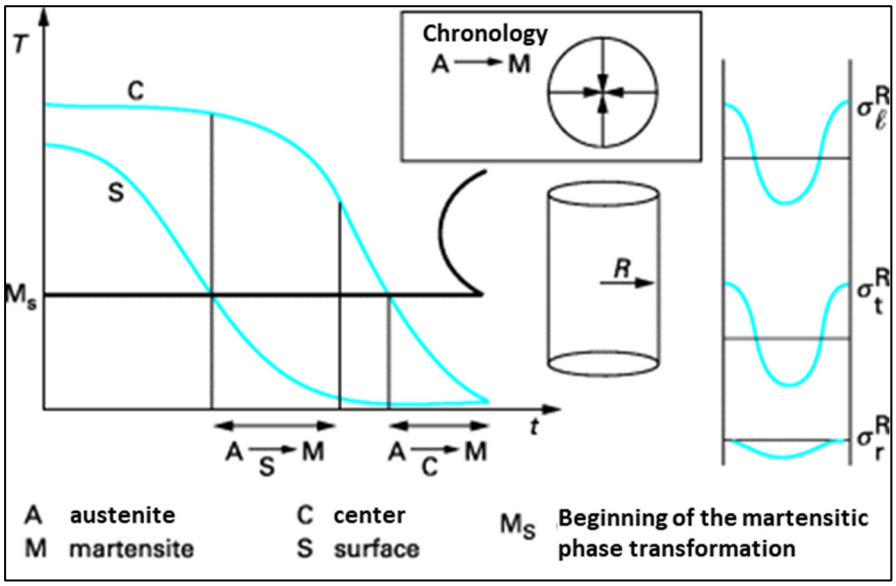

Figure 1.13 Representation of the residual stresses induced by the phase transformation during a quenching process
Adapted from Barralis and Maeder (1999, p. 18)

In real conditions of quench, both phenomena occur simultaneously which results in complex interactions. This is without accounting other factors such as the geometry, the quenching medium, the type of steel, etc. The combination of all makes the distortions much harder to predict.

1.3 Physical Fields and Interactions

As previously explained, distortions occurrence is related to the change in temperature. In that regard, the three main physical fields, the thermal field, the metallurgical field and the

mechanical field, are mandatory in order to correctly model the final distortion (Caner Şimşir & Cemil Hakan Gür, 2008). Figure 1.14 shows the relation between these three physical fields. This includes several interaction aspects between two main physical fields such as latent heat, transformation induced plasticity and heat induced by deformation, etc.

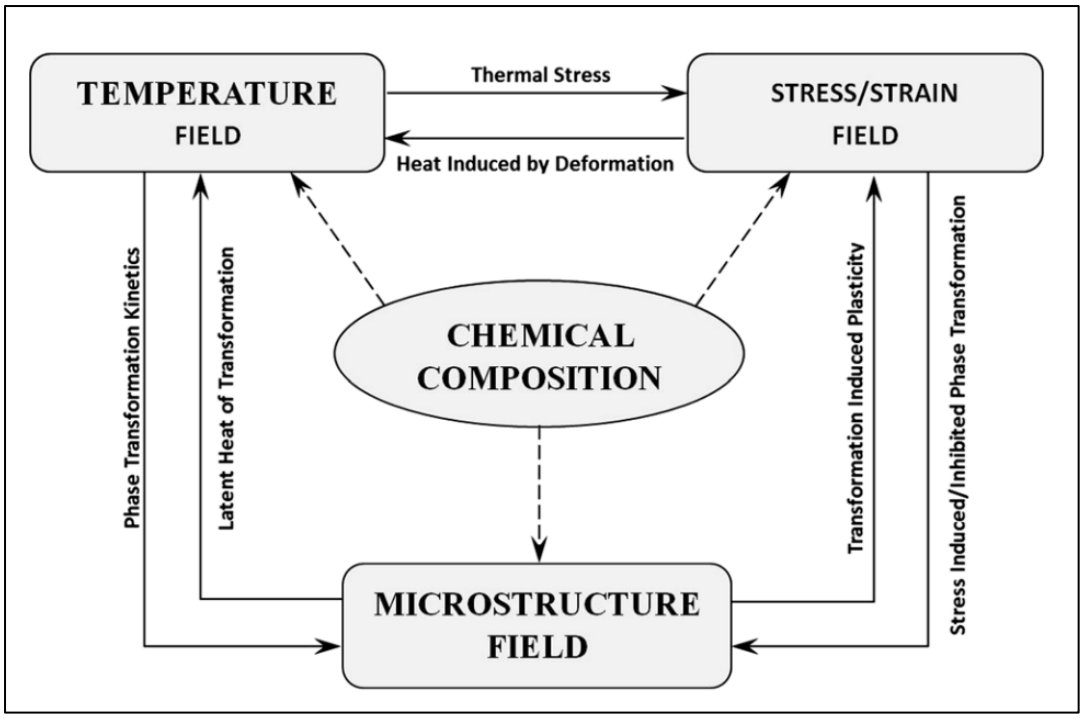

Figure 1.14 Main physical fields and couplings during heat treatments
Taken from Nie, Wang, Lin, and Rong (2015, p. 4881)

The creation of such models would only be valid for a specific chemical composition. The different material related properties would be slightly different for one steel to another and therefore, substitute material properties are not entirely applicable for precise prediction of distortions.

1.3.1 Heat Transfer

The temperature change is the main driving force which leads to all subsequent processes during quenching. As the high temperature steel is immersed on a cooler liquid, convective heat transfer takes place on the interface between the part and the cooling medium. Within the material, conductive heat transfer follows, and a temperature gradient is perceived from the outer surface to the inner core. The high temperature gradient across the section of the part would cause contraction/tension.

1.3.1.1 Convection

The heat convection is modeled using the heat loss from an interface between the part and the environment which can be written as:

$$q"_{conv} = h(T - T_{\infty}) \tag{1.1}$$

where $q"_{conv}$ is the heat flux of the part, h is the heat coefficient, T and T_{∞} are the temperature of the surface and the temperature of the environment respectively (Incropera et al., 2011; Sanchez Sarmiento, Gaston, & Totten, 2011).

During the immersion, different stages of heat transfer occur with varying heat fluxes as illustrated in Figure 1.15 (Caner Şimşir, 2008). Initially, a vapor blanket forms as the temperature of the part is much higher than the liquid medium's boiling point. This is known as the Leidenfrost effect (Leidenfrost, 1966). In this stage, the vapor blanket acts as an isolator which limits the heat transfer. This stage ends once the temperature of the part reaches the Leidenfrost temperature, and the vapor blanket collapses and nucleate boiling stage begins. At this point, the heat transfer is at its maximum. Lastly, the final stage is the natural convection as the temperature approaches to the boiling point of the liquid. The transfer rate is reduced significantly and is highly dependent on the agitation or flow of the quenchant.

Aside from the different stages of heat transfer, other effects such as the geometry, size, quenchant flow direction and flow rate, all affect the heat transfer. Thus, the determination of the heat coefficient h remains one of the main challenges in the simulation heat treatments and prediction of distortions (Hasan, 2009).

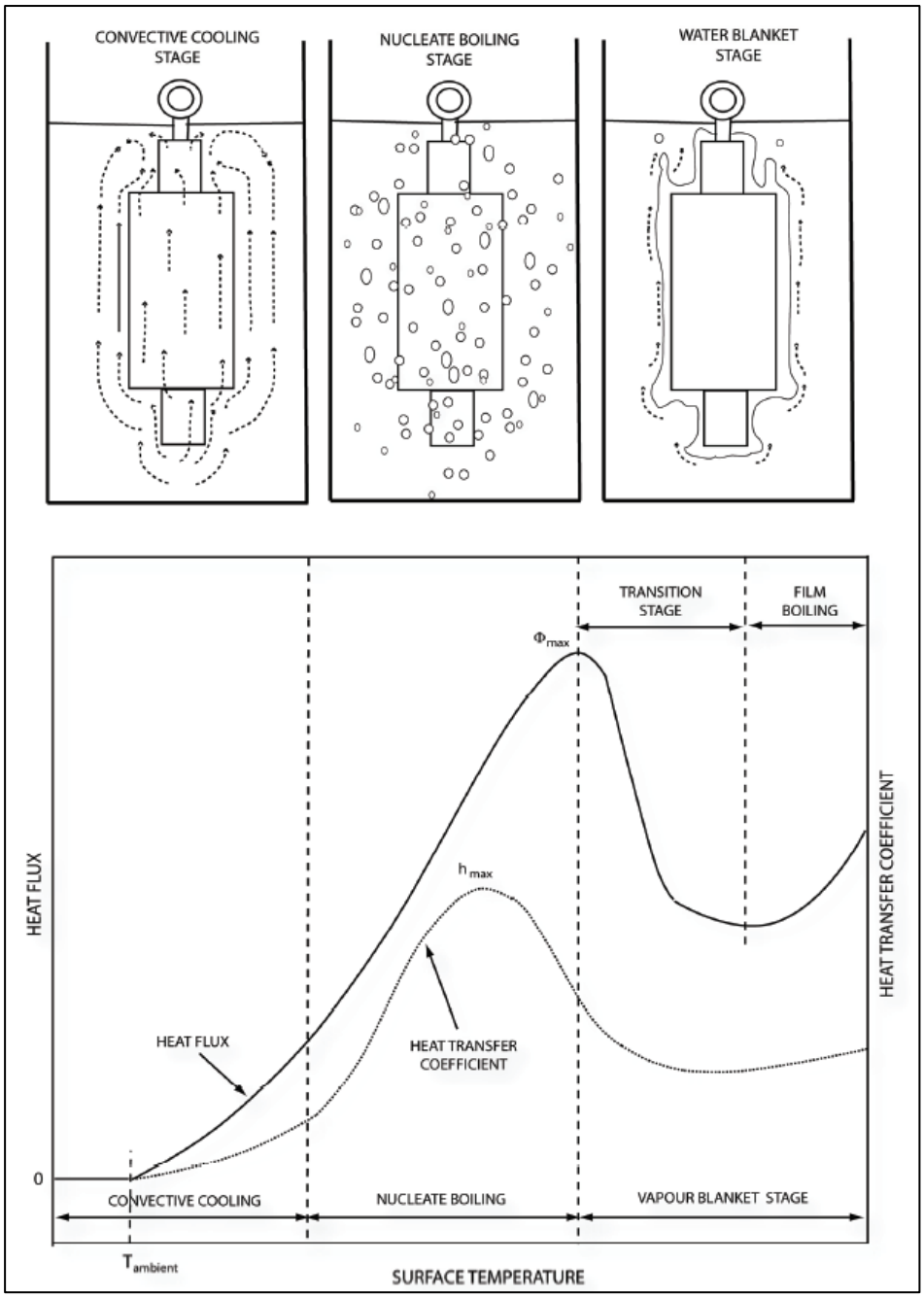

Figure 1.15 Different stages of immersion quenching with the associated heat flux
Taken from Caner Şimşir (2008, p. 16)

1.3.1.2 Radiation

Radiation is usually included in models to incorporate the duration of air transfer of the part from the furnace to the quenchant. Moreover, during the vapor blanket stage where convective heat transfer is low, heat transfer by radiation is the primary contributor. The general radiation heat flux can be expressed as:

$$q"_{rad} = \sigma_{SB}\ \varepsilon\ (T^4 - T_\infty^4) \tag{1.2}$$

where σ_{SB} represents the Stefan-Boltzmann constant and ε is the emissivity (Incropera et al., 2011). As for the inclusion of radiation during the vapor blanket stage, a pseudo convective coefficient could be used instead (Vanoverberghe, 2008).

$$h' = h + \sigma_{SB}\ \varepsilon\ (T + T_\infty)(T^2 + T_\infty^2) \tag{1.3}$$

1.3.1.3 Conduction

The temperature distribution of the part is expressed using the Fourier heat equation:

$$\rho\ c_p\ \frac{\partial T}{\partial t} = \lambda\ \nabla T + Q_{int} \tag{1.4}$$

where λ, ρ and c_p are the thermal conductivity, the density and the specific heat capacity respectively. These physical parameters are material and temperature dependent. ∇T is the temperature gradient and Q_{int} represents the internal heat source to accommodate for the latent heat released during phase transformation (Peterli et al., 2017; Caner Şimşir, 2008).

1.3.2 Phase Transformation

For ferrite and pearlite, transformation occurs with diffusion where carbon atoms could move from the austenite's crystal lattice. For martensite, the transformation happens too quickly for carbon atoms to diffuse and they are embedded within the crystal lattice at room temperature.

The determination of temperatures can be obtained by either extracting the values from the TTT diagram or CCT diagram. This, however, requires some laboratory testing when the values are unavailable in the literature.

1.3.2.1 Diffusional Transformation

Different methods are available for the modelling of diffusional phase transformations, isothermal transformation approach and anisothermal transformation approach. For an isothermal process, the application is very limited to laboratory use as it is a highly specific heat treatment with most industrial heat treatment processes being anisothermal. Approximations can still be obtained for anisothermal processes using isothermal equations by applying the additivity rule.

The modelling of a diffusional decomposition of phases can be separated into two steps, the incubation and the growth. The Johnson-Mehl-Avrami-Kolmogorov (JMAK) simplified equation is often used (Avrami, 1939; Fanfoni & Tomellini, 1998):

$$z_k = 1 - \exp(-b_k\ t^{n_k}) \tag{1.5}$$

where z_k corresponds to the fraction of phase k, b_k and n_k are coefficients which can be obtained from, either the TTT diagrams or the CCT diagrams. As part of this equation, additional parameters have been introduced in different studies to include initial phase mixtures and the amount of remaining austenite (Caner Şimşir, 2008; Vanoverberghe, 2008).

$$z_k = z_a \; z_k^{max}\left(1 - \exp\left(-b_k t^{n_k}\right)\right) \tag{1.6}$$

$$z_k = z_k^0 + \left(z_k^{max} - z_k^0\right)\left(1 - \exp\left(-b_k t^{n_k}\right)\right) \tag{1.7}$$

where z_a represents the amount of remaining austenite and z_k^{max} the maximum fraction of the phase k at the considered temperature.

The change in temperature through time can be modeled by incorporating the Scheil's additivity rule (Pietzsch, Brzoza, Kaymak, Specht, & Bertram, 2007; Roux & Billardon, 2007; Caner Şimşir, 2008). In this case, the incubation time required before phase growth can be implemented as:

$$\int_0^{t_n} \frac{dt}{\tau(T)} = 1 \tag{1.8}$$

where t_n corresponds to the end time of incubation. $\tau(T)$ is the incubation time in an isothermal condition at the temperature T. On a more practical approach, the rule can be simplified by using a series of steps as approximation:

$$\sum_{i=1}^{n_i} \frac{\Delta t_i}{\tau(T_i)} = 1 \tag{1.9}$$

where n_i is the number of steps used. When this addition equals 1, the transformation can now begin. This method also works for the growth time where t_n would be of a different value depending on the types of transformation. This is accomplished with the implementation of the JMAK equation.

1.3.2.2 Diffusionless Transformation

For martensitic phase transformation, the process is temperature dependant as opposed to the diffusional where it is greatly dependant on the time factor. The K-M equation is generally used for the modeling of the kinetics of martensite phase transformation and expressed as (Bhadeshia & Honeycombe, 2006; Koistinen & Marburger, 1959; Roux & Billardon, 2007; Caner Şimşir, 2008; Vanoverberghe, 2008):

$$z_m = z_a(1 - \exp(-\beta(M_s - T))) \tag{1.10}$$

where z_m is the fraction of martensite, z_a is the maximum fraction of martensite, M_s is the martensite start temperature, T is the temperature below the Ms to which the part is cooled, often the room temperature for a quenching process ($T \leq M_s$). β is the rate of transformation parameter and it was initially considered as a constant with a value of 0.011. It has been now demonstrated that the value changes according to the chemical composition (van Bohemen & Sietsma, 2013).

1.3.3 Mechanical Behaviour

Modeling heat treatment is an intricate process as the temperature covers a wide range. Models used must be chosen accordingly which are usually classified into three major categories, elasto-plastic models, elasto-viscoplastic models and unified plasticity models.

The choice of an elasto-plastic is of preference for a quenching process (Caner Şimşir, 2008). The rate independent model is based on the yield criterion where plastic flow occurs after passing the yield strength of the material. The von Mises yield surface is usually employed for the determination of plastic flow. If stress state lies within the surface, elastic flow is observed. If stress state lies on the boundary of the stress surface, plastic flow is observed. As for the hardening rule, purely isotropic hardening is used for a quenching process. However, purely isotropic hardening rarely occurs and the absence of kinematic hardening.

In elasto-viscoplasticity, a reference surface such as the previous yield surface is defined as an elastic potential surface. Any stress state within this surface generates a reversible deformation. Any stress state outside correspond to the plastic flow and the rate of plastic deformation would be dependent on the distance of the stress state and the elastic potential surface. For simulation relying on high CRs (quench simulation), elasto-viscoplasticity models are often omitted.

As for the unified plasticity models, it's the combination of plasticity and viscoplasticity into one set of equations (Alberg, 2003). Unfortunately, one common problem with the usage of such models is the large numbers of material data which are hard to obtain.

In a complex multiphysics problem, multiple events could lead to deformation. From there, it is usually assumed that the total strain is the additive decomposition of five strain components (Nallathambi, Specht, Bertram, & Kaymak, 2010).

$$\varepsilon = \varepsilon^e + \varepsilon^p + \varepsilon^{th} + \varepsilon^{pt} + \varepsilon^{tr} \tag{1.11}$$

where ε, ε^e, ε^p, ε^{th}, ε^{pt}, ε^{tr} represent the total, elastic, plastic, thermal, phase transformation and transformation induced plasticity strain.

1.3.3.1 Phase Mixture Modeling for Mechanical Properties

When dealing with a multiple phase material, global thermo-mechanical properties must be somehow approximated based on the thermo-mechanical properties of each phase. Different approaches could be used in order to determine the total strain.

The first one is based on a linear rule of mixture on the material properties. The thermo-mechanical properties are the result of the sum of all thermo-mechanical properties of each phase present (T. Inoue & Wang, 1986). Therefore, the properties' macroscopic value would be written as:

$$P_{macro}(T) = \sum_{k=1}^{n} z_k(T)\, P_k(T) \tag{1.12}$$

where P_k represents the material properties for the phase k. These properties are weighted by the volume fraction of the phase, denoted by z_k. The global properties would be used in order to determine their respective strain rates.

The second approach is based on the mixture of homogenous strains specific to a phase in a heterogeneous environment (Leblond, Mottet, & Devaux, 1986a, 1986b):

$$\varepsilon_{macro} = \sum_{k}^{n} \varepsilon_k \tag{1.13}$$

where ε_k is the total strain for the phase k which can be calculated as:

$$\varepsilon_k = \varepsilon_k^e + \varepsilon_k^p + \varepsilon_k^{th} + \varepsilon_k^{pt} + \varepsilon_k^{tr} \tag{1.14}$$

1.3.3.2 Transformation Induced Plasticity

Nowadays, transformation induced plasticity (TRIP) is a well-known phenomenon. This effect can be described as the development of plastic strain during phase transformation and under mechanical loads that is lower than the yield stress.

A first mechanism was proposed by Greenwood and Johnson (Greenwood & Johnson, 1965) which related the TRIP effect to the compactness of the parent and product phases, as illustrated in Figure 1.16. The incompatibility of deformation due to the different volume results in an eigenstrain which is compensated or accommodated with an irreversible strain.

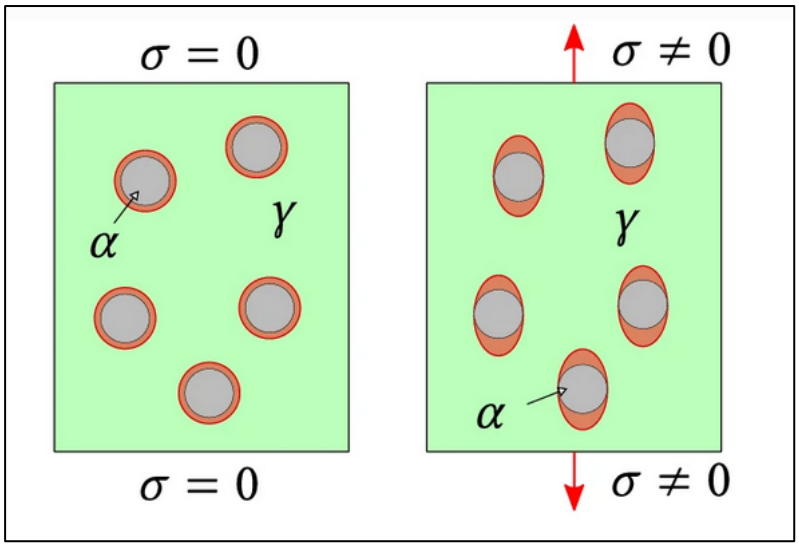

Figure 1.16 Greenwood and Johnson's mechanism of TRIP
Adapted from Wölfle, Krempaszky, and Werner (2021, p. 323)

Another mechanism is explained by Magee (Magee & Paxton, 1966), as shown in Figure 1.17. The martensitic plates are sheared during formation and with the dilatation due phase transformation, plastic strains are developed at the proximity following a preferential orientation if an external load is applied.

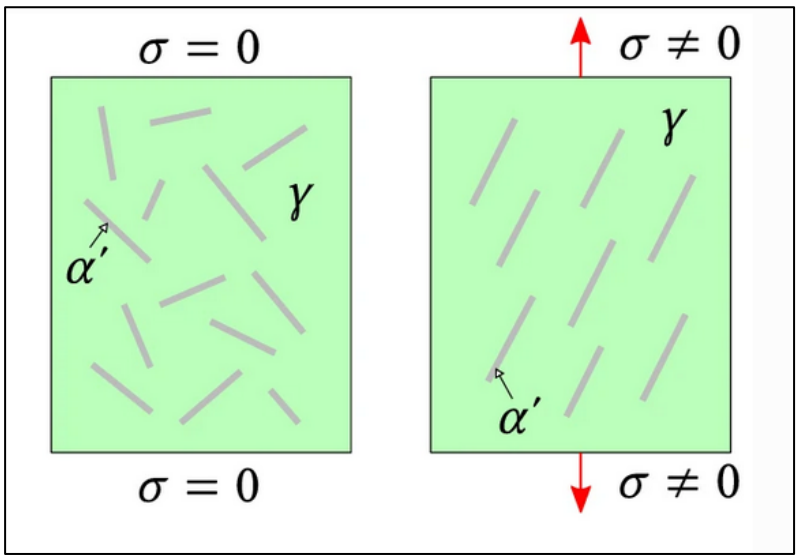

Figure 1.17 Magee and Paxton's mechanism of TRIP
Adapted from Wölfle et al. (2021, p. 323)

In general, the formulation for TRIP is written as follows (Simsir, 2017):

$$\varepsilon^{tr} = K\,\sigma\,\phi(z) \tag{1.15}$$

Where K represents the transformation plasticity parameter, σ the external stress applied to the material and $\phi(z)$, a value between 0 to 1 representing the progress of the transformation plasticity, with $\phi(0) = 0$ and $\phi(1) = 1$. The determination of parameter K can be done experimentally or through calculation using different models proposed by researchers.

Greenwood-Johnson mechanism is modeled as follows (Greenwood & Johnson, 1965):

$$\varepsilon^{tr} = \frac{5}{6}\frac{\Delta V}{V}\frac{\sigma}{\sigma_y^{min}} \tag{1.16}$$

with the parameter K being:

$$K = \frac{5}{6}\frac{\Delta V}{V}\frac{1}{\sigma_y^{min}} \tag{1.17}$$

where $\frac{\Delta V}{V}$ is the structural dilatation of the material under transformation and σ_y^{min} is the minimum yield strength of the weakest phase. The difference in volume can also be approximated using the densities of parent, ρ_a, and product phases, ρ_k:

$$\frac{\Delta V}{V} = \frac{\rho_a - \rho_k}{\rho_a} \tag{1.18}$$

Abrassart (Abrassart, 1972) proposed another model for the transformation induced plasticity:

$$\varepsilon^{tr} = \frac{1}{4}\frac{\Delta V}{V}(3z - 2z^{3/2})\frac{\sigma}{\sigma_y^{min}} \tag{1.19}$$

with K being in this case:

$$K = \frac{1}{4}\frac{\Delta V}{V}\frac{1}{\sigma_y^{min}} \tag{1.20}$$

In their model, the progress of transformation for a martensitic transformation, $\phi(z)$, corresponds to:

$$\phi(z) = 3z - 2z^{3/2} \tag{1.21}$$

Leblond also came up with a similar model (Leblond, Devaux, & Devaux, 1989):

$$\varepsilon^{tr} = \frac{2}{3}\frac{\Delta V}{V}z(1 - ln(z))\frac{\sigma}{\sigma_y^{min}} \tag{1.22}$$

$$K = \frac{2}{3}\frac{\Delta V}{V}\frac{1}{\sigma_y^{min}} \tag{1.23}$$

$$\phi(z) = z(1 - \ln(z)) \tag{1.24}$$

1.4 State of the Art, Challenges and Objectives

Simulations on distortions are often performed on small sized components with simple geometries or with simplifications on the implemented models. For instance, the earliest simulations were performed on cylinders. Inoue and Tanaka were among the first to simulate the residual stresses (Tatsuo Inoue & Tanaka, 1975). The simulation was performed on a 0.43 % carbon steel cylinder using thermal expansion coefficients for the phase transformation. However, latent heat was omitted during their simulation. Following their pioneering work, Fernandes et al. considered latent heat from phase transformation through a source term in the

heat transfer equation (Fernandes, Denis, & Simon, 1985). Their study also focused on cylinders by using the Scheil's additivity principle and the Johnson-Mehl-Avrami equation to model the incubation and growth duration for diffusional transformations. Diffusionless transformation was modeled using Koistinen-Marburger equation. Franz et al. showed the importance of including the transformation plasticity on residual stresses and distortions for steels with different carbon content (Franz, Besserdich, Schulze, Müller, & Löhe, 2005). Once more, the geometry used was a simple cylinder.

With increased computational power, geometries slowly diverged from cylinders. However, they still remain simple geometries, often with one or several symmetry axis. Nallathambi et al. studied the sensitivity of thermal, metallurgical and mechanical properties on the curvature of an L beam of a 100Cr6 steel (Nallathambi et al., 2010). da Silva et al. performed a simulation of the quenching of a 4140 steel C-ring using the DEFORM-HT software (da Silva et al., 2012). Material data was obtained with JMatPro software. Nie *et al.* (Nie et al., 2015) simulated the distortions in a nut's internal threads where precision is required to avoid assembly difficulties. They used the commercial software DANTE with user subroutines in ABAQUS/STD. Li and Ferguson (Z.-C. Li & Ferguson, 2011) used DANTE to simulate the heat treatment of a AISI 9310 carburized steel gear.

Very few studies on heat treatment simulation for distortions have been performed on large sized components for industrial applications with complicated shapes or geometries such as landing gear main fittings. Therefore, aspects, such as large temperature gradient and non-uniform phase transformation across the thickness were not of concern as the studied components were small.

As previously mentioned, the main objective of the current project is to develop TMM model for the simulation of quench induced distortions in a large sized component. More specifically, the project will focus on two of the three mandatory physical fields presented in the literature review, the metallurgical and mechanical fields. The detailed objectives of the project are as follows:

- The determination of the kinetics of martensite transformation during a quenching process with various CRs under martensite start temperature (Ms). This will provide a better understanding of the kinetics due to the influence of time and, therefore representing more accurately the actual behavior for large sized components during quench.

- The determination of the thermo-mechanical properties. These properties are crucial as they will determine the outcome of displacements and the distortions that ensues. Without available and reliable data, measurements must be acquired through numerous tests.

- The identification of constitutive models that precisely describes the previously identified kinetics of phase transformation and thermo-mechanical properties.

CHAPTER 2

MATERIAL AND EXPERIMENTAL METHODOLOGIES

2.1 Low Alloy Medium-Carbon Steel

In order to gain better mechanical properties with a great resistance to corrosion, a class of steels called high strength low alloy steels have been developed (Skobir, 2011). This class diverges from the common plain carbon steels with the addition of several alloying elements such as a combination of chromium, nickel, molybdenum, copper, nitrogen, vanadium, titanium and zirconium at a very low amount. The amount of alloying elements usually doesn't surpass 10%. The low alloy medium-carbon steel is a formidable choice for the manufacturing of landing gears due to its ultra-high strength with a high level of toughness and high resistance to fatigue (R. C. Chen, Hong, Li, Zheng, & Li, 2017; Flower, 2013). The as received material is obtained from slabs of different annealed and normalized forgings. The general chemical composition of the main alloying elements is shown in Table 2.1.

Table 2.1 General chemical composition of the investigated steel (wt. %)

Fe	C	Mn	Si	Ni	Cr	Mo
Balance	0.40	0.70	1.65	1.80	0.80	0.40

2.1.1 Heat Treatment Process

The current heat treatment process flow is illustrated in Figure 2.1. The landing gear main fitting and the rig is preheated at 500 °C and austenitized at 875 °C for several hours. It is then air transferred from the furnace to the oil tank for immersion, during which an initial non-uniform cooling takes place from the outer surface through the thickness of the part. The uneven temperature distribution across the thickness is particularly striking when the part is immersed in oil. In addition, various oil flows affect the CRs from parts to parts. Following

the oil quench, prior to the final machining, all parts are tempered twice. Between each of the tempering, the parts are air cooled to room temperature.

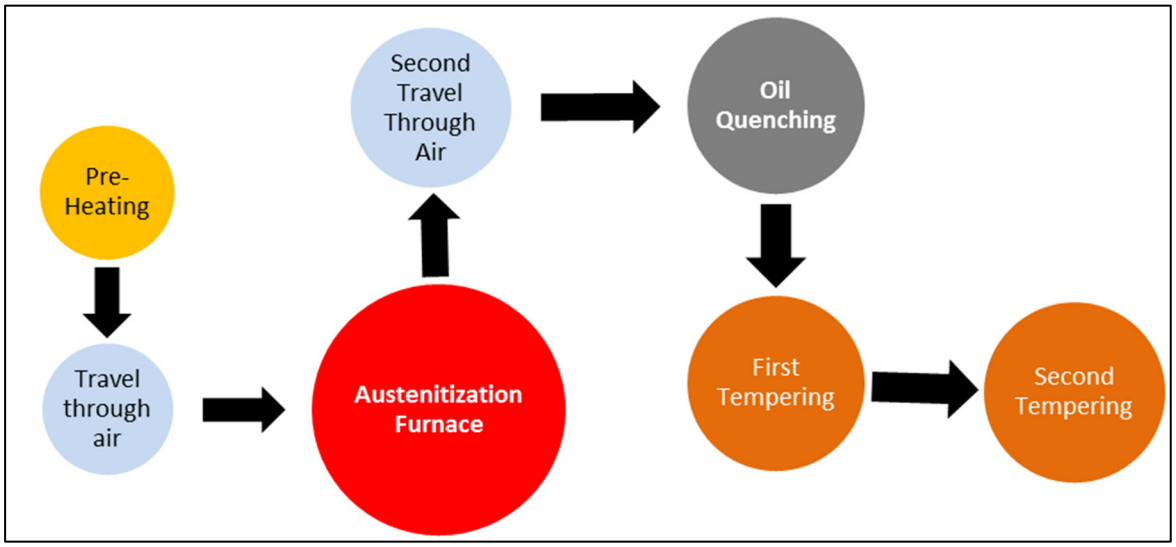

Figure 2.1 Typical heat treatment process flow for a landing gear main fitting

The non-uniform cooling through the thickness is shown in Figure 2.2. It was obtained by simulation using a cylinder with a thickness of 80 mm. The result behaviour resembles the actual condition of the landing gear main fitting when compared with the measured temperatures by various thermocouples. Aside from the non-uniform cooling, the massive size of a landing gear makes the cooling temperature stagnate at a temperature range between 300 °C and room temperature for several hours, as shown by the green colored area.

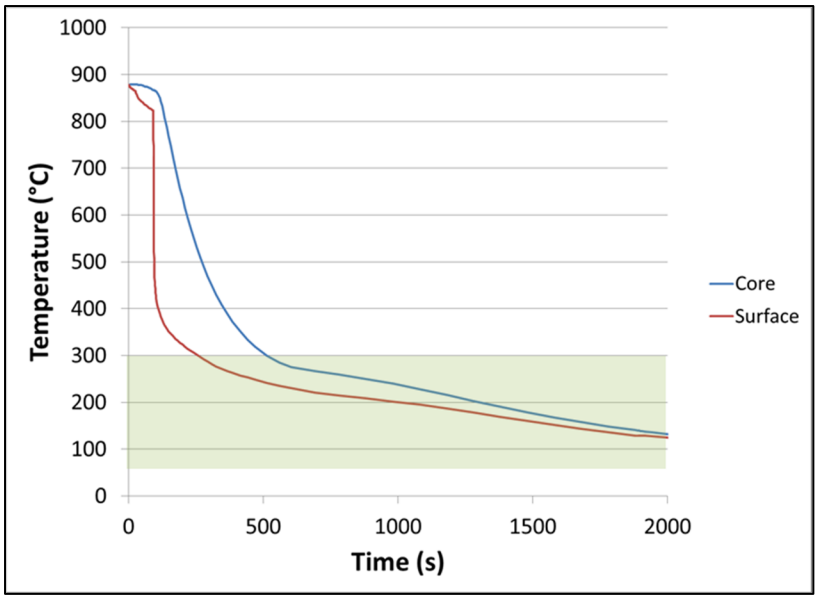

Figure 2.2 Schematic of the non-uniform cooling of a cylinder with a thickness of 80 mm obtained through simulation

2.2 DIL805 A/D

The DIL805 A/D is the main dilatometer used in this project for the assessment of the kinetics of phase transformation. The equipment is shown in Figure 2.3. This high-resolution dilatometer is able to measure dilatations as small as 0.01 µm per 0.05 °C and at a large temperature range of 20 - 1700 °C. The heating of an electrically conductive material is accomplished by induction through a water-cooled copper coil, reaching heating rates up to 100 °C/s. Before and during heating, a partial vacuum is created limiting the effect of oxidation at high temperatures. As for the cooling, inert gas such as helium or argon are released directly to the specimen via the copper coil. The heating and cooling are program controlled and the real-time temperature is measured by a k-type thermocouple, spot-welded to the surface of the specimen. The measurement of the dilatation is through two push rods, one that is fixed and the other one attached to a linear variable differential transducer. Held in between these rods, is the specimen which expands or contracts with temperature changes. The push rods are made of fused silica for low temperature (under 1200 °C) and alumina for higher temperature. The

standard sample geometry consists of a cylinder with a diameter of 4 mm with a length of 10 mm.

Figure 2.3 Dilatometer DIL805 A/D
Taken from TA Instruments (2023)

The system is also configurable with the possibility of adding of different modules such as a deformation module, a sub-zero module, a coefficient of thermal expansion measurement module and an optical measurement of dilatation module for higher accuracy with a possibility of measuring radial dilatation.

2.2.1 Dilatometry Fundamentals

The principle of dilatometry consists in measuring the dilatation or the change in length during continuous heating and continuous cooling of a material, in this case, steel. This works in the determination of phase transformation as the γ-iron, of a FCC structure, and α-iron, of a BCC structure, both have different specific volume as previously explained.

2.2.1.1 Critical Temperatures

By recording the dilatation, the temperature and time for a whole heat treatment cycle, it is then possible to determine the critical temperatures by plotting different graphs. With the change in length as a function of temperature, any change of slope is an indication of an instability of the current phase at that temperature, therefore corresponding to the start of phase transformation. Taking the initial length of the sample as a reference, the slope can be used to approximate the coefficient of linear thermal expansion (CLTE) using the following expression (James, Spittle, Brown, & Evans, 2001):

$$\alpha_L = \frac{1}{L}\frac{dL}{dT} \tag{2.1}$$

where L is the given length, dL and dT are the instantaneous change of length and temperature, respectively. This is with the assumption that the CLTE is constant for the given temperature range.

An example of a quench process is shown in Figure 2.4. The slopes of the green, blue and orange lines are used for approximating the CLTE of the base material phase, the austenite phase and the martensite phase, respectively. The change in the slope indicates the start and finish transformations.

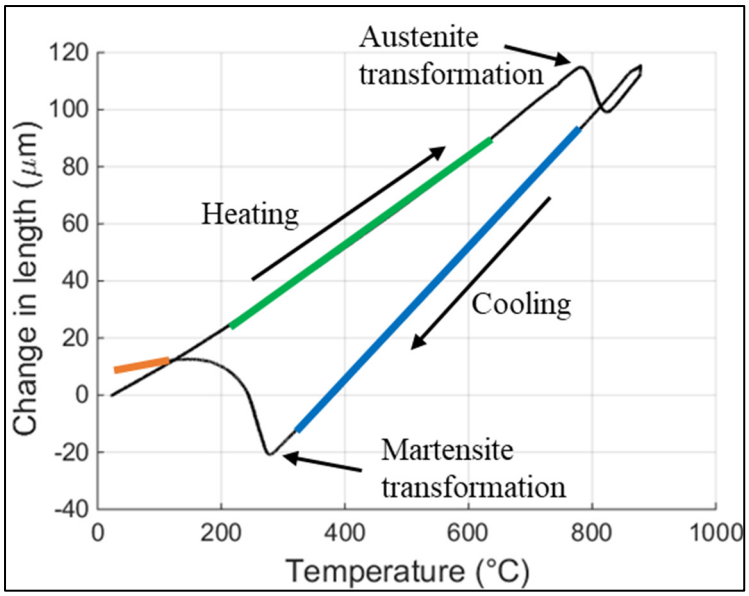

Figure 2.4 Typical dilatometry curve for a heat treatment cycle

2.2.1.2 Kinematics of Phase Transformation

From the start of a transformation, the transition of one slope to another corresponds to the ongoing phase transformation. One method which is often used to approximate the fraction is the lever rule (Mustak, Evcil, & Simsir, 2016; Suh, Oh, Han, & Kim, 2007):

$$f_m(T) = \frac{\Delta L(T) - \Delta L(T)_a}{\Delta L(T)_m - \Delta L(T)_a} \tag{2.2}$$

where $f_m(T)$ represents the fraction of martensite calculated at temperature T. $\Delta L(T)$ is the dilatation and a and m, represent the phases austenite and martensite.

The principle is simple, two segments are extended and the fraction of the transformed phase at a given temperature is the relative length of the vertical segment within the extended segments. Figure 2.5 illustrates the method where the extended segments correspond to the blue and red dashed lines. The vertical arrows correspond to the fraction of transformed phase (martensite) and the remaining phase (austenite) at that given temperature.

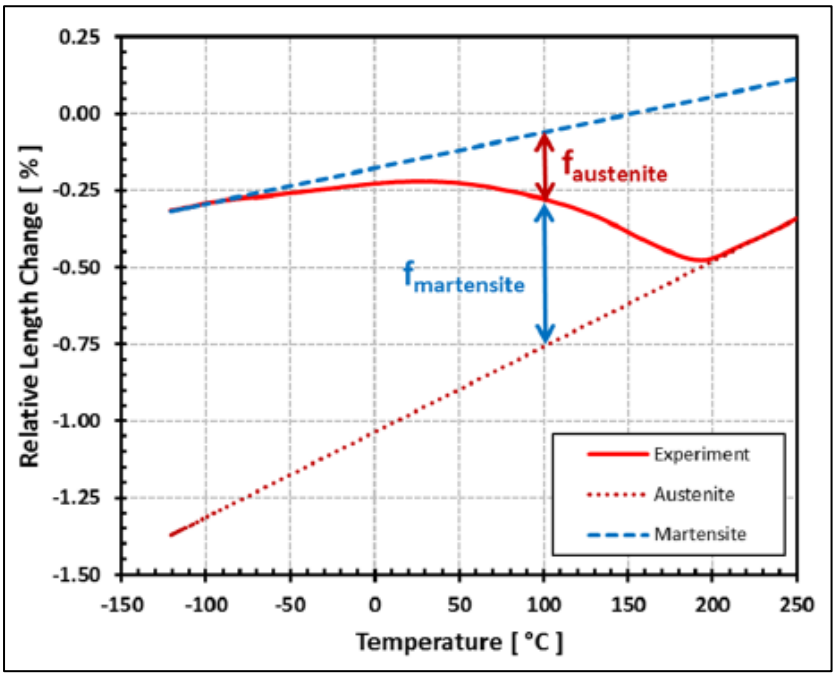

Figure 2.5 Determination of the fraction of martensite from a dilatometry curve
Taken from Mustak et al. (2016, p. 4)

The method is convenient as it is simple to use. It only works with the assumption that the final microstructure constitutes entirely of the transformed phase. In the example, martensitic transformation usually has RA at room temperature (Carlone, Palazzo, & Pasquino, 2010; Deng & Ju, 2013). This amount is not possible to quantify using the dilatometry curves only.

2.3 Gleeble 3800

The Gleeble 3800 is a thermo-mechanical simulator. The whole system can be seen in Figure 2.6. Similarly to the dilatometer, it measures the dilatation of a specimen during heating and cooling but also due to external mechanical loads exerted by the system which is able to reach as much as 20 tons. High heating rates exceeding 10 000 °C/s can be achieved by resistance heating and measured by a k-type thermocouple spot-welded to the surface of the specimen.

The system can be programmed through 3 control variables, the force applied, the stroke for the displacement and the temperature. Unfortunately, no more than one variable can be controlled at a time. The measurement of the displacement can be done with the internal linear variable differential transducer (LVDT) or with the addition of an external strain gauge extensometer attached to the specimen.

Figure 2.6 Thermo-mechanical simulator Gleeble 3800
Taken from Dynamic Systems (2023)

2.3.1 Temperature Gradient

Due to the Joule heating effect and the constant cooling of the anvils holding the sample, the temperature gradient across the length of the specimen is a high concern for the usage of this equipment (Kardoulaki, Lin, Balint, & Farrugia, 2014; Xiao, Fan, Zhan, Liu, & Zhang, 2021). If a high temperature gradient is present, the phase transformations as well as the mechanical responses will be inaccurate. For this matter, temperature gradient must be minimized. In this project, mechanical loadings are applied to 2 phases, austenite and martensite which are stable

at different temperature ranges. The following sections discuss about the determination of the sample geometries for each phase.

2.3.1.1 Lower Temperature Specimen Geometry

The initially tested sample has a cylindrical geometry with a reduced section in the gauged area as suggested by Dynamic Systems. The dimension of the sample is shown in Figure 2.7. Three thermocouples are welded in the center of the specimen with approximately 5 mm apart from each other to measure the temperature difference. The three thermocouples are labeled as TC1, TC2 and TC3, with TC2, being the control.

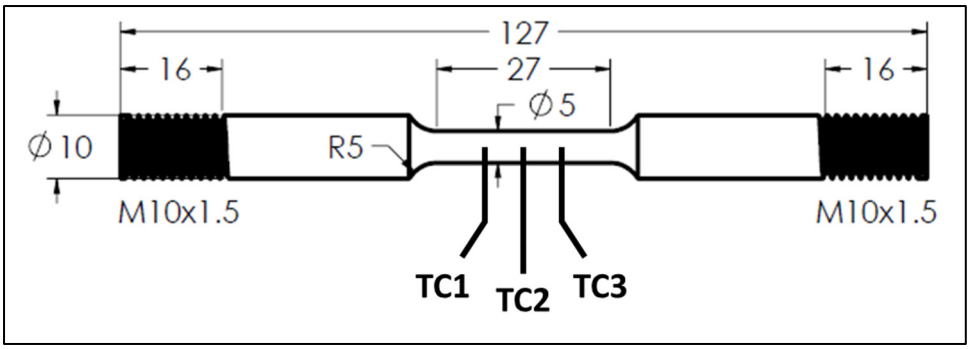

Figure 2.7 Cylindrical geometry with reduced section sample

The specimen is then heated to a temperature of 878 °C, soaked for 10 min and oven cooled to room temperature. The temperatures measured by all 3 thermocouples are shown in Figure 2.8. A significant difference of 23 °C is observed between TC1 and TC2 and an even higher difference of 35 °C for TC2 and TC3. The soaking time also did not mitigate the temperature difference as the sample is constantly cooled from the sides through the anvils. Due to this high temperature difference, the usage of this geometry for high temperature tests is very limited. However, at lower temperature, such as 300 °C and lower (showed by the dash line), the temperature difference is considerably lower, less than 4 °C difference. Therefore, this geometry has been used for thermo-mechanical tests on martensite. Moreover, this geometry is also very convenient for mechanical tests on martensite as the deformation is highly

localized in the gauge length and reduced section where displacements are measured. For other sample geometries, due to the high strength and low ductility of martensite, deformation and possible ruptures often occur at the threads instead.

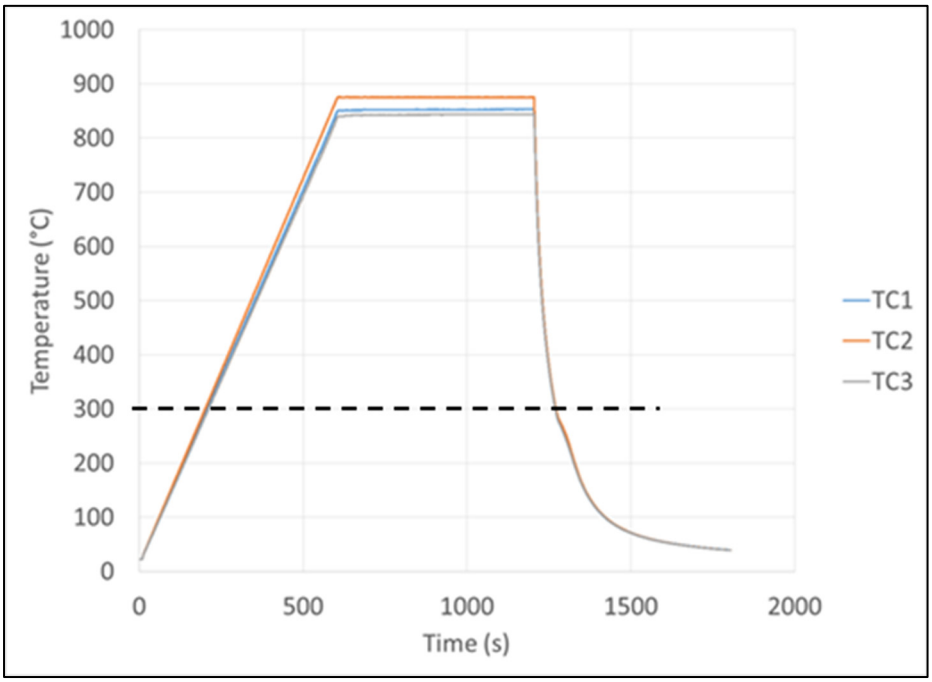

Figure 2.8 Temperature measurements for a cylindrical with reduced section specimen

2.3.1.2 High Temperature Specimen Geometry

As for high temperature tests, it is obvious that the previous geometry would provide inaccurate mechanical results due to the high temperature gradient. To reduce the amount of cooling from sides, the surface area has been reduced and a constant diameter geometry has been adopted, as shown by Figure 2.9. Using the same procedure of three thermocouples (TC1, TC2 and TC3) with 5 mm apart, the temperature difference is measured.

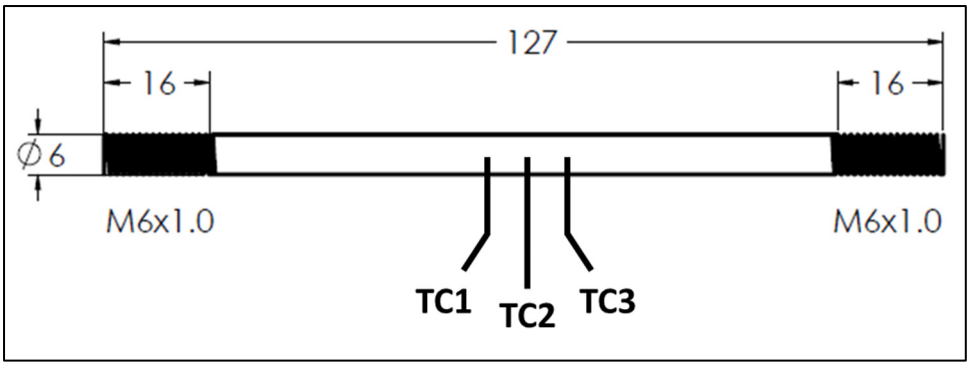

Figure 2.9 Constant diameter geometry sample

The sample is heated to 878 °C and soaked for 10 min. It was subsequently cooled to 500 °C and held for another 5 min before oven cooled to room temperature. This 5 min isothermal holding provided information regarding the temperature difference but as well as the duration permitted for conducting the mechanical test before phase transformation. The highest difference in temperature was less than 3 °C and observed at 878 °C. Therefore, the geometry of a constant diameter was deemed favorable for high temperature tests on austenite. Also, as austenite is a more ductile material and with a higher temperature at the center of the sample, the deformation is always localized within the measured area of the extensometer (center of the specimen) even without the reduction in diameter.

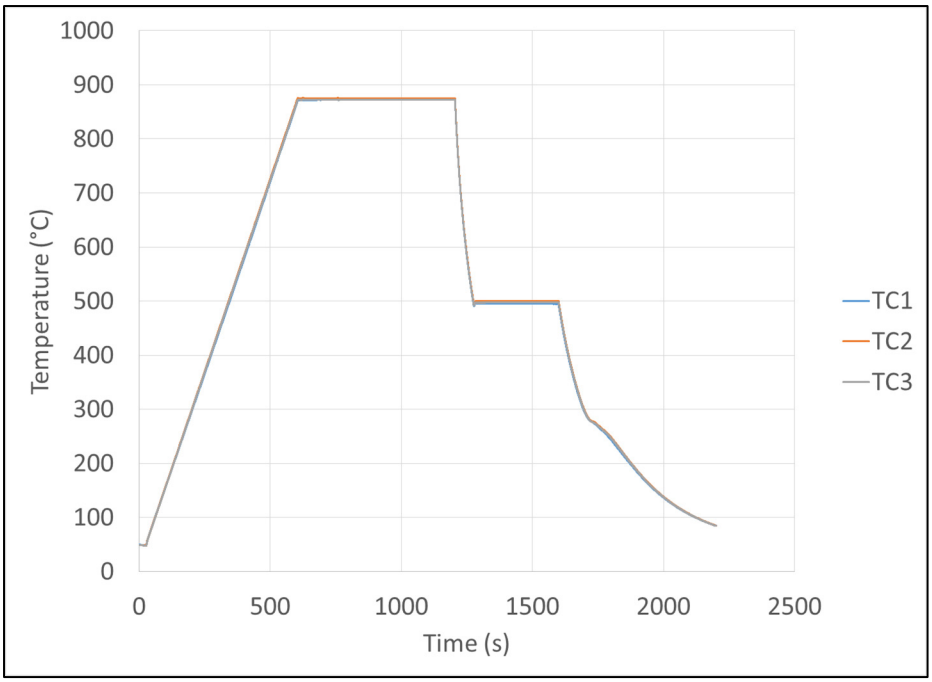

Figure 2.10 Temperature measurements for a constant diameter geometry

CHAPTER 3

INFLUENCE OF THE COOLING RATE BELOW MS ON THE MARTENSITIC TRANSFORMATION IN A LOW ALLOY MEDIUM-CARBON STEEL

Jia Hong Liu[a], Nicolas Binot[b], Denis Delagnes[c], Mohammad Jahazi[d]

[a, d] Mechanical Engineering Department, École de technologie supérieure, 1100 Rue Notre-Dame Ouest, Montreal, H3C 1K3, QC, Canada
[b] Materials and Processes Laboratory, Safran Landing Systems, Etablissement de Bidos, 64400 Oloron-Sainte-Marie, France
[c] Institut Clément Ader (ICA), Université de Toulouse, CNRS, IMT Mines Albi, UPS, INSA, ISAE-SUPAERO, Campus Jarlard, 81013 Albi CT Cedex 09, France

Paper published in *Journal of Materials Research and Technology*, February 2021

Abstract— The influence of cooling rate *below* the martensite start temperature, Ms, on the kinetics of martensitic transformation in a medium carbon low alloy steel was determined using high resolution dilatometry, electron microscopy and X-ray diffraction techniques. A two-stage transformation was observed for slow cooling rates while at higher cooling rates, martensitic transformation occurred through a single stage process. It is shown that the Koistinen-Marburger equation cannot adequately describe the observed two-stage transformation. A new equation is proposed in order to model the evolution of martensitic transformation by considering the influence of post Ms cooling rate. The method considers contributions both from initial austenite and the carbon enriched austenite. The underlying mechanisms are discussed and validated with experimental findings.

Keywords— Kinetics; Modeling, Martensitic Phase Transformation, Dilatometry, Retained Austenite

3.1 Introduction

Martensitic transformation is generally depicted as a diffusionless mechanism that is solely defined by the degree of undercooling which takes place upon reaching the Ms during a quench (Seo, Cho, & De Cooman, 2016; Totten, 2007). A sufficiently fast cooling rate is necessary in order to avoid the formation of intermediate phases such as bainite. The conventional method of carrying quench experiments is by dilatometry using constant cooling rates from the austenitization to room temperature (Fredj, Nanesa, Shahriari, Morin, & Jahazi, 2017; van Bohemen & Sietsma, 2010). The dilatometric data is then used to construct continuous cooling rate diagrams and to model the evolution of the martensitic fraction as a function of temperature via the Koistinen-Marburger (K-M) equation (Bojack, Zhao, Morris, & Sietsma, 2012; Fredj et al., 2017). However, such experiments and modeling with K-M equation without considering the duration required to reach from Ms to Mf could be an over simplification for industrial applications. In fact, as the quenching is generally an uncontrolled process, variable cooling rates are observed throughout the process particularly, in the case of large size components. As the temperature decreases, the cooling rate is significantly reduced due to the small temperature differences between the component and the quenching medium. The process could then take several hours before the component actually reaches room temperature, lingering around the transformation range. Using a constant cooling rate from austenitization to room temperature to determine the kinetics of phase transformation could, therefore, lead to inaccurate estimations of phase changes. By using various cooling rates under Ms, it will be possible to better understand the effect of time on martensitic transformation and provide a more accurate representation of the quenching process. Such understanding is of critical importance when it comes to developing numerical models for predicting quench induced distortion of large size components with complex geometries made of medium carbon steels.

Knowing the kinetics of phase transformation is of great importance by allowing the development of models which provide means for engineers to predict and design materials accordingly. Dilatometry has become a necessary tool in the study of phase transformation. Researchers have used the dilatometry with the combination of optical and electron

microscopy and synchrotron X-ray diffraction to determine the microconstituent fractions (Obasi et al., 2019). Others have used dilatometry coupled with synchrotron X-ray diffraction to study the kinetics of austenite reversion and its stability (Conde et al., 2019; Escobar et al., 2019; Escobar et al., 2017).

In the simplest form, the kinetics of martensite transformation are often obtained by relating the length change of the sample during the dilatometry test to the progress of martensite transformation. The standard reverse S shape is usually observed when using a constant cooling rate from austenitization to room temperature (Celada-Casero, Sietsma, & Santofimia, 2019; Y. B. Guo, Sui, Liu, Chen, & Zhang, 2015; van Bohemen & Sietsma, 2014). However, some researchers have observed "unusual" (Loewy, Rheingans, Meka, & Mittemeijer, 2014) and "abnormal" (Villa, Pantleon, Reich, Kessler, & Somers, 2014) kinetics in which irregularities have been noticed on the dilatometry curves during the martensitic transformation. These variations in the fractions of formed martensite as a function of temperature have the particularity of occurring in the form of steps interpreted as the acceleration or deceleration of the transformation. The steps are easily discernable as peaks when the results are plotted with the first derivative, representing the rate of transformation. Loewy et al. (Loewy et al., 2014) related such observations to the simultaneous formation of martensite blocks in different packets. Furthermore, they reported that the overall transformation rate was independent from the employed cooling rates. Villa et al. (Villa et al., 2014) described the anomalous deceleration martensite formation as the effect of strain and interfacial energy while the acceleration was related to the autocatalytic nucleation of martensite. Liu et al. (Chenxi Liu, Liu, Zhang, & Yan, 2012), associated the splitting behaviour of martensitic transformation to the precipitation M_3C particles. Although some studies report unusual behaviour in dilatometry diagrams, most studies focus mainly on the athermal aspect of the transformation and very little attention has been paid to the influence of post Ms cooling rates on the transformation.

In the present work the influence of cooling rate (i.e. the time factor) between the martensite start (Ms) and martensite finish (Mf) temperatures on the evolution of martensitic

transformation was investigated. A new equation is proposed that more accurately describes changes in martensite fraction during the quench process.

3.2 Experimental Procedures

The studied material is a wrought low alloy medium-carbon steel, with the following chemical composition: Fe–0.43C–0.71Mn–0.006P–0.001S–1.63Si–1.81Ni–0.83Cr–0.40Mo–0.07V–0.11Cu (wt. %). Dilatometric experiments were carried out using the high resolution Bähr DIL 805A/D dilatometer with samples of 4 mm in diameter and 10 mm in length, extracted from the as received material. Details of the applied thermal cycles are shown in Figure 3.1. The colored lines represent the different cooling rates after the Ms temperature. All samples were heated from room temperature to 878 °C with the same heating rate of 1.42 °C/s and then soaked for 600 s, both under vacuum. The samples were then cooled using helium with an identical cooling rate of -2.27 °C/s until 300 °C. The temperature of 300 °C was determined based on preliminary dilatometry tests that showed this temperature is slightly above the actual Ms. Subsequent cooling rates of -2.27 °C/s, -0.33 °C/s, -0.16 °C/s and -0.11 °C/s were then used to study the effect of cooling rates below Ms on the kinetics of martensitic transformation. For easier reading purposes, these cooling rates will be henceforth labeled as CR1, CR2, CR3 and CR4, as also indicated in the inset of Figure 3.1.

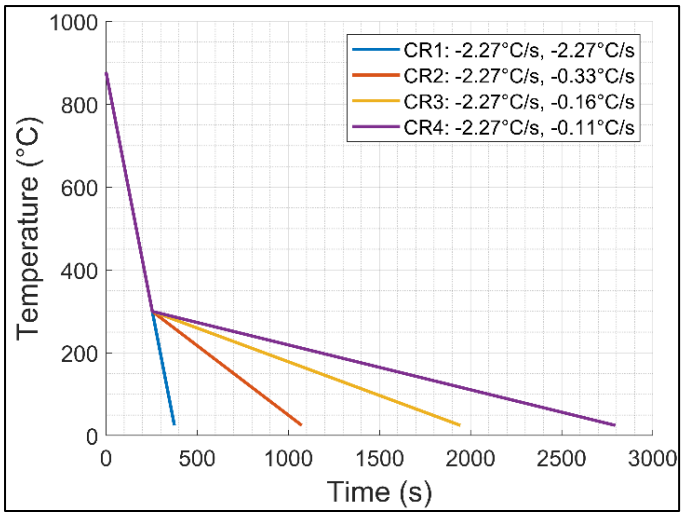

Figure 3.1 Planned thermal cooling cycles in which they share an initial and identical cooling rate of -2.27 °C/s until the temperature of 300 °C; it is then followed by cooling rates of -2.27 °C/s, -0.33 °C/s, -0.16 °C/s and -0.11 °C/s for the color blue, red, orange and purple, respectively

Following the dilatometry experiments, the samples were cut in half for microstructural investigations. Each sample were manually ground to P4000 SiC grit paper and finished by polishing down to 1 μm with a diamond solution. The samples were then etched using a 3% Nital solution for 7 s at room temperature. Optical micrographs are acquired using a laser scanning confocal microscope, Olympus LEXT OLS4100.

The other halves of the cut dilatometry samples are also used for quantitative X-ray diffraction (XRD) tests in order to determine the amount of retained austenite (RA). Measurements were performed with a Malvern Panalytical's X'Pert^3 MRD diffractometer with Co K-α radiation under a current of 40 mA and a voltage of 45 kV. A 2θ scan range of 48° to 108° with a scanning speed of 1.3°/min was used. The software HighScore was used for background removal as well as identification of the peaks' position. The volume fraction of RA was then calculated using XRD peak intensities following the Ref. (ASTM, 2013).

3.3 Results

3.3.1 Dilatometry and Fractions of Martensite

Figure 3.2(a) shows the complete dilatation curves as a function of temperature during martensitic transformation for all four investigated cooling rates. An enlarged area of the transformation, indicated by a dashed circle, is shown in Figure 3.2(b). As observed, the kinetics of martensite transformation show different patterns with decreasing cooling rates. Specifically, for CR1, a conventional dilatation rate is identified where a strong and initial phase transformation is observed as soon as the temperature reaches the Ms and gradually slows down as the remaining austenite is transformed. Transformation stops when the dilatation curve follows a straight line. However, for CR2, CR3 and CR4, discontinuities, in the form of acceleration and deceleration of transformation, can be observed. This behaviour is consistent with previous findings from other researchers (Caballero, Álvarez, Capdevila, & García de Andrés, 2003; Loewy et al., 2014; Villa et al., 2014); however, they were not associated with the cooling rates below Ms. It is interesting to note that the martensite fraction formed during the first stage does not solely decrease when lower cooling rates are used. In fact, for CR4 with a slower cooling rate than CR3, the observed fraction formed before the deceleration is higher than for CR3, which suggests the presence of an inflection point. The black crosses in Figure 3.2(b) indicate the local maxima used as estimations of the Mf. The measured maxima values are 163 °C, 151 °C, 131 °C and 117 °C for CR1, CR2, CR3 and CR4, respectively. The above finding reveals that as the cooling rate below Ms becomes lower the microstructure becomes more and more stable and the Mf is nearly reached. It must be mentioned that due to mechanical stabilization of RA a complete transformation (i.e., 100%) of austenite to martensite is not expected, unless reaching very low temperatures and therefore accurate determination of Mf is more challenging (Khan & Bhadeshia, 1990; Yi, Lee, & Bhadeshia, 2011). It was also found that the final length of the sample decreased as the cooling rate decreased. These length differences could be attributed to the stabilization of austenite due to carbon partitioning from supersaturated martensite (van Bohemen & Sietsma, 2014). Consequently, the length differences could provide an indication for the quantity of RA at

room temperature. The relation between the cooling rate and the amount of RA will be presented and discussed in the upcoming sections of this paper. The calculated RA from dilatometry will also be compared to the experimentally measured RA by XRD to validate this hypothesis.

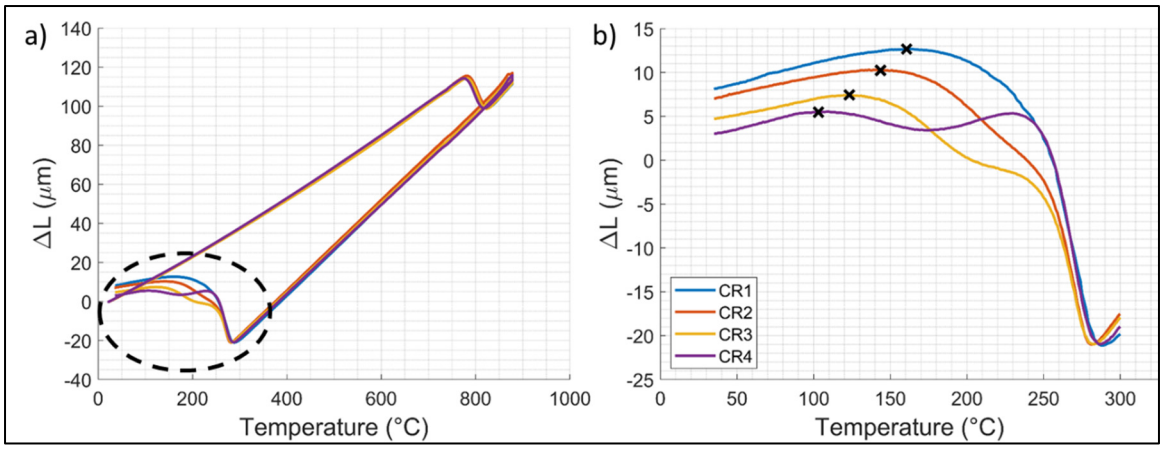

Figure 3.2 (a) Complete dilation curves for all four investigated thermal cycles; (b) Enlarged area corresponding to the martensitic transformation (dashed circle in Figure 3.2(a))

Further analysis of the results was conducted by using the lever rule to convert the dilatation curves into transformed phase fractions. For the incorporation of the length differences in the determination of RA, an initial known value of martensite fraction is needed from the set dilatometry of curves. However, such value is impossible to obtain based solely on dilatometry. Therefore, at this preliminary stage, without any additional information regarding the microstructure, it is assumed that CR1 results in a fully martensitic microstructure. This allows the determination of RA for the other curves in terms of proportions. The amount of RA for CR2, CR3 and CR4 due to the final length differences in comparison to CR1 was estimated using the following equation:

$$X_i = \frac{\Delta L(T)_{\mathrm{CR}i} - \Delta L(T)_{\mathrm{A,\,CR}i}}{\Delta L(T)_{\mathrm{M,\,CR1}} - \Delta L(T)_{\mathrm{A,\,CR}i}} \tag{3.1}$$

where X_i represents the calculated fraction of martensite for dilatation curve *i,* and CR*i* is the corresponding cooling rate. A and M represent the phase austenite and martensite, respectively. For instance, $\Delta L(T)_{\mathrm{A,\ CR}i} \mid_{i=3}$ is the change in length for the austenite phase from the dilatation curve of CR3, at temperature *T*. Calculated fractions derived from dilatation curves are reported in Figure 3.3(a). It can be seen that for CR1 the transformation kinetics represents a reverse S shape. However, as the cooling rate decreases the sharpness of the shape gradually fades away and a double reverse S shape is observed.

3.3.2 Modeling of the Kinetics of Phase Transformation

A common practice is to model the martensitic phase transformation as a function of temperature using the K-M equation (Koistinen & Marburger, 1959):

$$X = 1 - \exp\left[-\Omega\ (CM_s - T)\right] \tag{3.2}$$

where X is the calculated fraction of martensite, Ω is a transformation rate parameter, CM_s the calculated Ms temperature and T the temperature. Variants of this equation have also been devised in order to incorporate the amount of remaining austenite available to transform and a better description of the onset of transformation (Gür & Şimşir, 2012; Mustak et al., 2016). As expected, due to the high cooling rate of CR1, K-M is able to accurately predict the martensitic transformation with Ω = 0.031 K^{-1} and CM_s = *284.3* °C. However, with CR3, K-M equation cannot describe the second stage of transformation as shown in Figure 3.3(b). Only CR3 was shown here in order to alleviate the graph. It is clearly visible that modeling CR2 and CR4 with K-M equation will also result in a poor agreement.

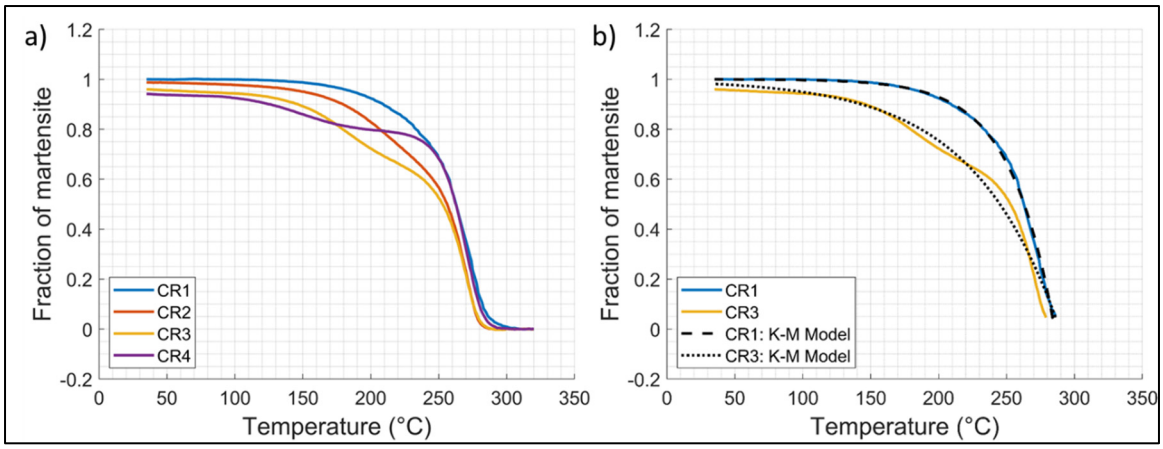

Figure 3.3 (a) Martensite fractions as a function of temperature calculated from dilatation curves and the final fraction achievable for CR2, CR3 and CR4 is determined with the assumption that CR1 forms a fully martensitic steel; (b) Modeling of the transformation kinetics using the K-M equation

The above findings clearly reveal the presence of a two-stage transformation process when the cooling rate below Ms is changed. This phenomenon is formalized in the form of an addition of a second term to the conventional K-M equation:

$$X = F\left(A\{1-\exp[-\Omega 1\,(CM_s 1 - T)]\} + (1-A)\left\{\frac{1}{1+\exp[-\Omega 2\,(CM_s 2 - T)]}\right\}\right) \tag{3.3}$$

where F indicates the maximum fraction of martensite transformed and A, the fraction by either sub-equation with both having values between 0 and 1. The parameters $\Omega 1$ and $\Omega 2$ represent the transformation rate for each stage. Lastly $CM_s 1$ and $CM_s 2$ are the calculated martensite start temperatures.

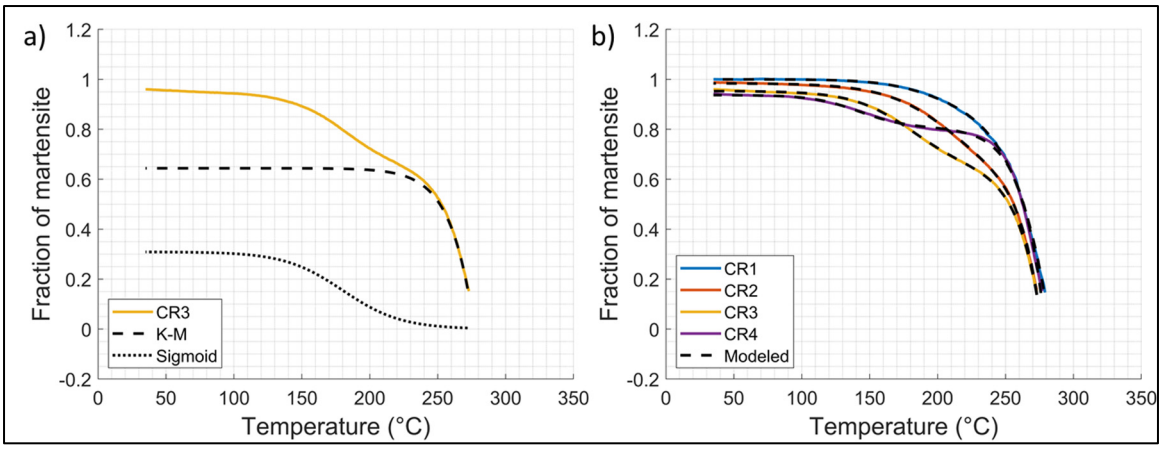

Figure 3.4 (a) Representation of the modeling method of CR3 by the decomposition of the proposed equation into both sub-equations; (b) Modeling of martensite transformation kinetics using the newly proposed equation with the least squares method

The rationale behind the proposed equation is illustrated in Figure 3.4(a). The equation is decomposed and both sub-equations are plotted separately with the dashed line representing conventional K-M equation and the dotted line, the new term. Again, only CR3 is shown for the sake of simplicity. This second term from the equation corresponds to the transformation of the second stage and takes the form of a general sigmoid equation. The proposed equation considers the transformation as a sum of two consecutive transformation. Similarly to the parameters from the K-M equation, the rate of transformation ($\Omega 2$) and start of the transformation (CM_s2) of the second stage is needed. The extraction of these parameters provides information regarding the kinetics of transformation for the second stage. For instance, a higher value of $\Omega 2$ means the transformation occurs at a higher rate.

The fractions contributed by each sub-equation were determined by the product of F with A and 1-A which, once added, gives the global fraction. A similar method was also proposed with the use of two K-M equations in Ref. (Bhadeshia, 2013). The main difference is that with a two K-M equations approach, two separate boundary conditions are needed in order to limit the application of each equation. Otherwise, negative phase fractions could be obtained, which are physically improbable. By introducing the sigmoid equation, as a second sub-equation, the above limitation is suppressed once the initial martensitic transformation has initiated. Thus,

in the present approach, K-M will always be used to model the first stage of transformation while the second term ensures the proper modeling of the second stage, if it is present. In such cases, it is expected that $CM_s1 > CM_s2$.

The values of the parameters in the new model for the present paper are reported in Table 3.1. As previously discussed, the parameter *F*, representing the maximum attainable phase fraction, progressively decreases with slower cooling rates.

Table 3.1 Values of the proposed equation's parameters

Cooling Cycle	*F*	*A*	$\Omega 1$ (K^{-1})	$\Omega 2$ (K^{-1})	CM_s1 (°C)	CM_s2 (°C)
CR1: -2.27 °C/s	1	0.942	0.035	0.078	282.8	246.8
CR2: -0.33 °C/s	0.984	0.598	0.073	0.040	276.0	209.6
CR3: -0.16 °C/s	0.953	0.676	0.068	0.046	276.9	179.3
CR4: -0.11 °C/s	0.937	0.861	0.058	0.063	279.3	137.2

When plotted as a function of cooling rate, it is hardly possible to distinguish a trend, as shown in Figure 3.5(a). However, as shown in Figure 3.5(b-d) when the parameters are plotted against the cooling durations, the influence of the cooling rate is better visualized and if any relation exists, it can be easily extracted and modeled, providing parameters that are now time dependent. By implementing these time dependent parameters in the proposed equation, it indirectly provides the kinetics of martensitic transformation. The durations correspond to the time required to cool from 300 °C to room temperature, depending on the applied cooling rate. As for *A,* $\Omega 1$ *and* $\Omega 2$, a more parabolic evolution is observed. This is also expected due to the presence of an inflection point, as previously mentioned. Thus, the inflection point would be somewhere between CR2 and CR3 where the maximum or minimum is located. For CM_s1, the values vary from 276.0 to 282.8 °C. As for CM_s2, it decreases considerably from 246.8 to 137.2 °C in an almost linear fashion.

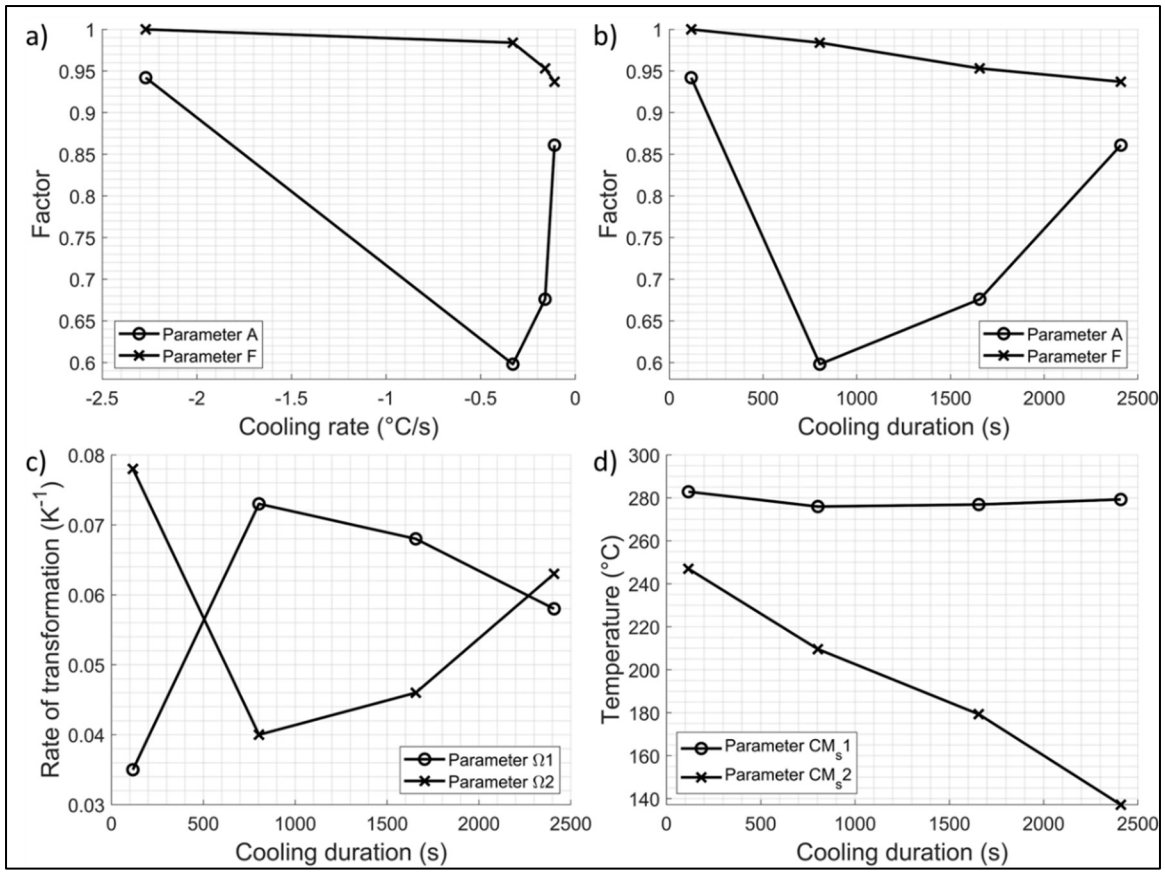

Figure 3.5 (a) Evolution of parameters *A* and *F* as a function of cooling rates; (b-d) Evolution of parameters, *A*, *F*, *Ω*1, *Ω*2, CM_s1 and CM_s2 as a function of cooling durations for the temperature range of 300°C to room temperature

3.3.3 Retained Austenite and XRD Measurements

The amount of RA is deduced from XRD measurements and used to complement the modeling previously performed from the dilatometry results. Within the full range of 2θ angle shown in Figure 3.6, a total of 6 peaks were identified which provides a higher accuracy regarding the determination of the volume fraction of RA at room temperature. The volume fractions derived from these peaks are 5.93%, 7.34%, 8.63% and 10.3% for CR1, CR2, CR3 and CR4, respectively. As expected, the volume fractions clearly increase with a slower cooling rate below Ms or with a longer cooling duration.

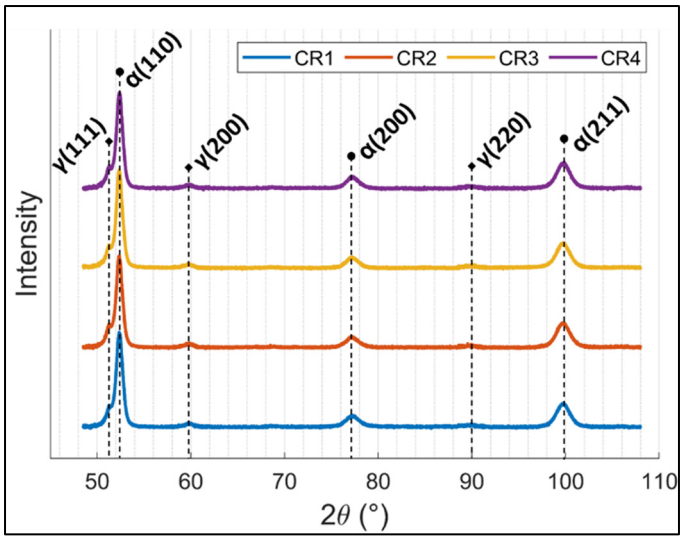

Figure 3.6 Retained austenite peaks for a 2θ scanning range of 48° to 108°

It was previously considered that the microstructure of CR1 is fully martensitic. Such assumption was useful in order to assess phase proportions based on length differences without any known measurement of the initial RA. However, now that a RA volume fraction of 5.93% has been measured, the initial assumption should be corrected. This new value from XRD was implemented for CR1, and the subsequent values from dilatometry are recalculated and rescaled by maintaining their proportions from the length difference. A total of 7.44%, 10.35% and 11.86% for CR2, CR3 and CR4 is calculated based on the new value of CR1. Figure 3.7(a) shows the evolution of the amount of RA as a function of the cooling duration. The full line with circles shows the calculated austenite from the final length differences measured by dilatometry experiments whereas the full line with crosses is the RA derived from the analysis of the diffraction peaks. As for the dash line with circle, it is the RA from dilatation scaled to the same initial value of XRD.

Visually, both methods display a very similar trend. Although there is some discrepancies in values for CR3 and CR4 between both methods, the approximation of the amount of RA using the final length difference is still plausible. However, with this approach, only proportions can be estimated between dilatation curves if the initial RA is unknown.

With more precise values with RA available, the modeling of the martensitic transformation from the proposed equation only requires changing the parameter *F*, corresponding to the maximum fractions of martensite. Figure 3.7(b) shows the final modeling with values for the parameter *F* of 0.941, 0.923, 0.897 and 0.881.

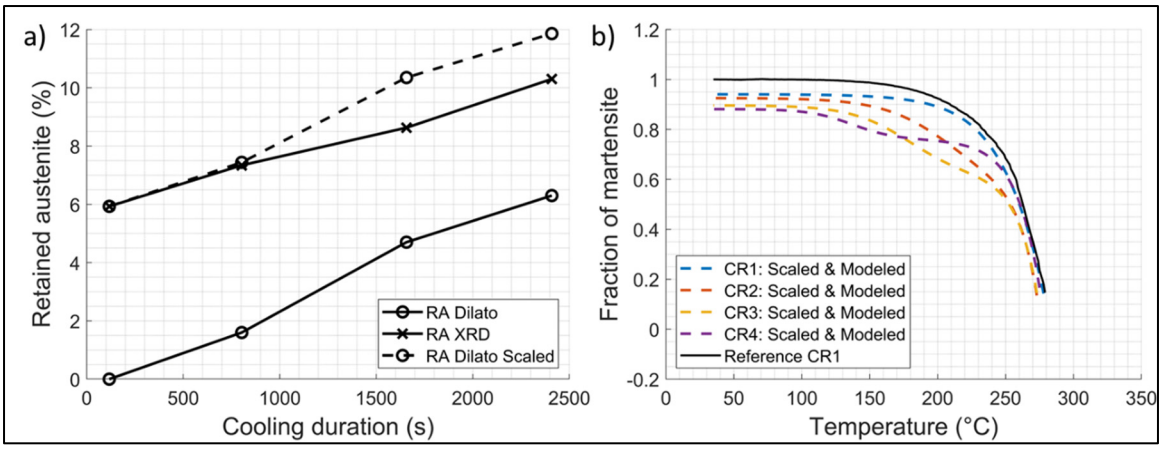

Figure 3.7 (a) Retained austenite as a function of cooling durations with the initial assumption of a fully martensitic steel for CR1 corrected to the measured values from XRD; (b) Modeling of martensite transformation kinetics using corrected values of the parameter F

Figure 3.8 shows optical micrographs of each dilatometry sample which are acquired in order to investigate the main mechanism responsible for the two-stage transformation as well as provide valuable insights of its effect on the microstructure. As expected, the main product formed consists of martensite. However, there's a noticeable difference in the microstructures as the cooling rate below Ms slows down from CR1 to CR4. As shown in Figure 3.8(a-b), for CR1 and CR2, the martensitic structure is mainly martensite laths grouped in packets as the material is a medium-carbon steel (Krauss & Marder, 1971; Stormvinter, Borgenstam, & Hedström, 2011; Vander Voort, 2001). For CR3 and CR4, a large amount of needle-like microstructure is clearly visible, indicated by the white and black arrows in Figure 3.8(c-d). These structures are similar to martensite plates which usually occur in high-carbon steels, above 0.6 wt. % (Stormvinter et al., 2011). This suggests that an increase of carbon content in the remaining untransformed austenite takes place during transformation.

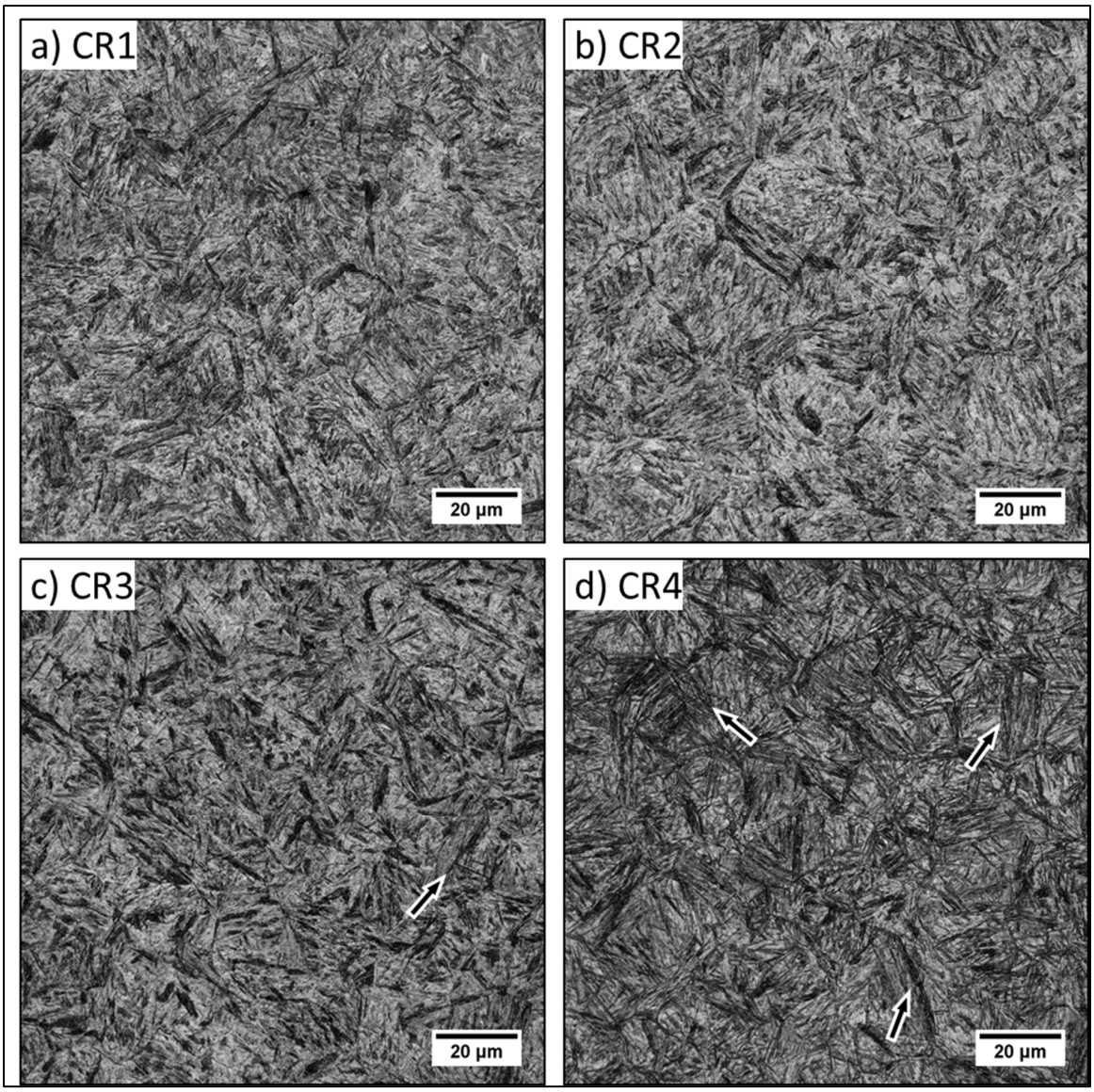

Figure 3.8 Optical micrographs of martensitic microstructures corresponding to each dilatometry sample: (a-b) A similar microstructure consisting of martensite laths is obtained; (c-d) An increasing number needle-like microstructure is observed

One simple method to estimate the carbon content in the austenite is to relate it to the Ms (Talebi, Jahazi, & Melkonyan, 2018; van Bohemen, 2013; J. Wang & Van Der Zwaag, 2001). Such approach is possible using the following equation proposed in Ref (J. Wang & Van Der Zwaag, 2001):

$$M_s\ (\mathrm{K}) = 273 + 545.8\ \mathrm{e}^{-1.362\,w_C} \tag{3.4}$$

where, w_C represents the carbon concentration in the austenite. With the values of the parameters collected by modeling the dilatation results and reported in Table 3.1, the second stage would correspond to the transformation from the carbon enriched austenite, therefore values from the parameters of the sigmoid sub-equation. In this case, the *CMs2* representing the calculated martensite start temperature of the second stage is to be used to estimate the carbon content at that precise moment. The calculated results for all 4 cooling rates are plotted in Figure 3.9. The increase in carbon content is rather significant with 0.58%, 0.70%, 0.82% and 1.02% for CR1, CR2, CR3 and CR4 respectively. The high amount of carbon content in CR3 and CR4 explains the microstructure previously identified. It is also important to note that despite the presence of a *CMs2* and an increase in carbon content for CR1, the majority of the transformation occurs during the first phase as shown with the single reverse S shape in Figure 3.3(a).

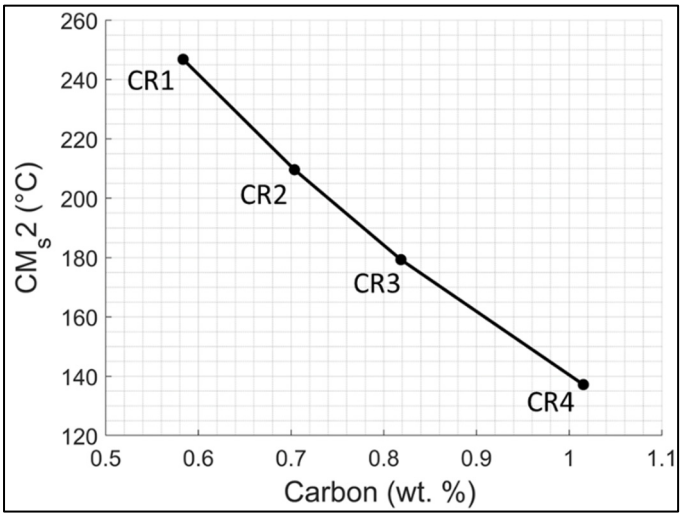

Figure 3.9 Decrease of the calculated martensite start temperatures for the second phase transformation due to the increase of carbon concentration in the remaining austenite during transformation

3.4 Discussion

In contrast to various modified K-M equations provided in the literature to model athermal martensitic transformation, the present equation addresses the complication of having more than one martensitic transformation. The acceleration and deceleration observed could be due to multiple mechanisms. Firstly, the prior austenite grain size is known to affect the Ms (Celada-Casero et al., 2019; S.-J. Lee & Van Tyne, 2011). However, in the present study, all the samples had a similar average grain size of 22 μm at room temperature and therefore, this factor was dismissed from the analysis.

The acceleration and deceleration is best explained by considering the auto-tempering of martensite formed from initial austenite blocks, also referred as massive austenite blocks (Caballero et al., 2003; García de Andrés, Caballero, Capdevila, & Álvarez, 2002). It implies the diffusion of carbon from the supersaturated martensite laths into the remaining or untransformed austenite (Ooi, Cho, Oh, & Bhadeshia, 2010; Seo et al., 2016). This is also evidenced by the observed microstructures from Figure 3.8 and the estimation of the carbon content from the modeling of the dilatation results from Figure 3.9.

The carbon enrichment contributes to the stability of the untransformed austenite and therefore lowers the Ms (Hsu, 1995; Morgan & Ko, 1953; van Bohemen & Sietsma, 2014). A higher degree of undercooling would then be necessary in order to reach the new Ms for the transformation to continue further. The formation of the inflection point could then be explained by relating between the Ms variation and the cooling rate. For CR1, as the cooling rate is high, carbon diffusion was unable to occur at a sufficiently high rate to slow down the transformation. For CR2 and CR3, carbon diffusion from the initial fraction of martensite to the remaining austenite was able to lower the Ms at a higher rate than the cooling rate, thus resulting in a Ms lower than the actual temperature which slows the transformation. In comparison to CR4 with a much slower cooling rate, the first stage has a high fraction of transformed martensite. This is due to the fact that with a lower cooling rate, the initial fraction of transformed martensite is also small, meaning that a lower amount of carbon atoms are able

to diffuse to the remaining austenite. The Ms would then only slightly decrease. The deceleration does eventually happen when a larger amount of martensite is transformed.

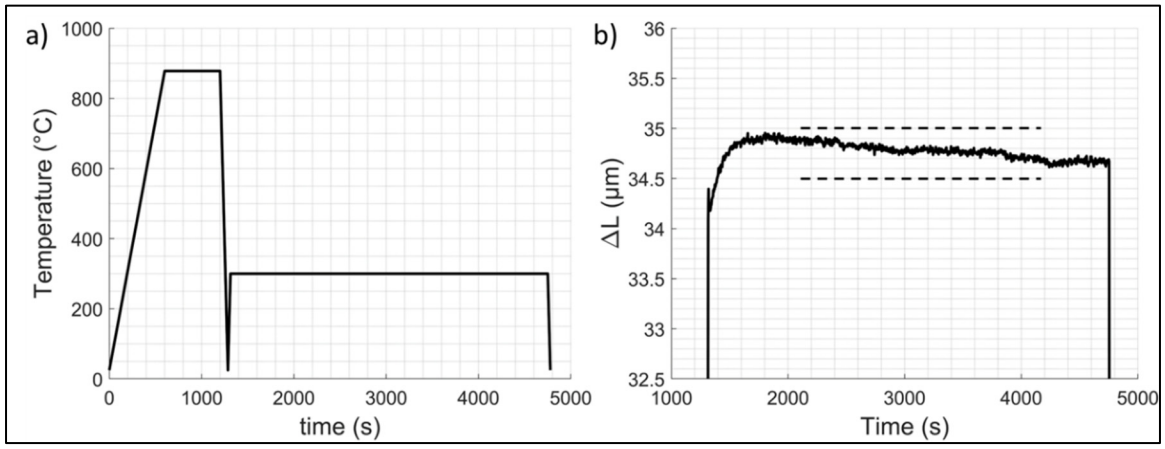

Figure 3.10 (a) Thermal cycle to determine the volume loss due to the effect of auto-tempering; (b) Dilatation results for the interval of tempering of the previously shown thermal cycle

In addition to the austenite stability due to carbon diffusion, a second concurrent effect of auto-tempering is the volume loss which directly correlates to the length decrease measured by dilatometry (Jung, Lee, & Lee, 2009). The possible influence of martensite-auto tempering was validated in the present study by performing a quench and tempering cycle, as shown in Figure 3.10(a). It is assumed that after the quench, the microstructure is fully martensitic. The total sample length change for the selected interval of tempering was about 0.5 μm, as shown in Figure 3.10(b). The obtained results clearly reveal that, the length change due to volume loss is not significant and unable to totally explain the martensitic transformation behaviour.

3.5 Summary

Through the use of dilatometry, the different cooling rates below Ms revealed a two-stage martensitic transformation. The commonly used K-M equation to model the fraction of martensite as a function of temperature was unable to accurately predict the transformation and a new equation was therefore proposed. This new equation demonstrated a good capability to

model the transformation. The second stage transformation was related to the carbon enrichment of austenite from the auto-tempering effect. This has been consistent with the findings from the microstructures which consist of martensite laths for fast cooling rates and martensite plates.

CHAPTER 4

A NEW ANALYSIS AND MODELING OF THE KINETICS OF MARTENSITIC TRANSFORMATION COUPLED WITH AUSTENITE STABILIZATION FOR A LOW ALLOY MEDIUM-CARBON STEEL

Jia Hong Liu[a], René Billardon[b], Denis Delagnes[c], Henri Champliaud[d], Antoine Tahan[e], Mohammad Jahazi[f]

[a, d, e, f] Mechanical Engineering Department, École de technologie supérieure, 1100 Rue Notre-Dame Ouest, Montreal, H3C 1K3, QC, Canada

[b] Safran Group, Safran Transmission Systems, 18 boulevard Louis Seguin, 92707 Colombes Cedex, France

[c] Institut Clément Ader (ICA), Université de Toulouse, CNRS, IMT Mines Albi, UPS, INSA, ISAE-SUPAERO, Campus Jarlard, 81013 Albi CT Cedex 09, France

Paper submitted for publication in *Acta Materialia*, June 2023

Abstract— In this paper, high resolution dilatometry with various controlled cooling rates between martensite start temperature and martensite finish temperature were conducted on a low alloy medium-carbon steel. Results revealed the presence of a deceleration in the observed ongoing phase transformation as a function of the temperature of a martensitic transformation. Single equation models such as the Koistinen-Marburger model have been proven to be unable to predict the kinetics with the presence of decelerations. To mitigate this problem, a new model is proposed to predict the instantaneous martensite fractions. It revolves around the determination of the carbon concentration in the remaining austenite. This increase in carbon concentration is based on the partitioning of carbon that occurs during the auto-tempering process. The result of this model provides accurate predictions for a quenching process with anisothermal coolings.

Keywords— Modeling, Martensitic Phase Transformation, Dilatometry, Carbon Partitioning, Modified Koistinen-Marburger

4.1 Introduction

Quenching is an important process in the manufacturing of steel components in order to achieve high levels of strength. It is also a process that often induces irreversible distortions to the component. This distortion must be taken into consideration during the design to avoid parts rejection. However, to accurately predict the magnitude and direction of distortion is still a major challenge. The key aspects of a successful and accurate simulation, such as the prediction of distortions during quenching, as well as the prediction of the post-welding complex microstructure, stem from the mathematical phase transformation models proposed in recent years by different researchers (Z. Guo, Saunders, Miodownik, & Schille, 2009; Pietzsch et al., 2007; Schenk, 2011; C. Şimşir, 2014).

Regarding the models for phase transformation in steel, extensive studies have been done on the kinetics of diffusive phases like ferrite and pearlite. A common practice used to predict the ongoing phase transformation of diffusive phases is the Johnson-Mehl-Avrami-Kolmogorov equation (Carlone et al., 2010; Gür & Şimşir, 2012; Jung, Lee, Lee, & Moon, 2018; Nallathambi et al., 2008). Such equation coupled with Scheil's additivity method allows the incorporation of the incubation time for *anisothermal* cooling routes using the material's time-temperature-transformation diagram (Obasi et al., 2019; C. Şimşir, 2014; Caner Şimşir & C. Hakan Gür, 2008). Other equations for diffusive transformation are also employed such as the Leblond and Brachet model which has the benefit of being in a differential form rather than an integral form, allowing the prediction of the instantaneous fractions (Brachet et al., 1998; Leblond & Devaux, 1984).

As for martensite, its transformation is often considered as *athermal*, a diffusionless transformation with only a dependency to the undercooling temperature and obtained by quenching processes (Bhadeshia & Honeycombe, 2006). The kinetics of martensitic transformation is generally modeled by using the Koistinen-Marburger (K-M) equation (Huyan, Hedström, & Borgenstam, 2015; Koistinen & Marburger, 1959; S. J. Lee, 2013). In general, from a fully homogenized austenite, the equation provides accurate modeling to most

cases due to the fast-cooling nature of the quenching process, which is required to avoid the formation of other phases, such as bainite. For this matter, studies regarding the modeling of martensite phase transformation have been scarce and are often focused on determining the values of the rate of transformation coefficients and the martensite start (M_s) or finish (M_f) temperatures for different steel compositions (van Bohemen & Sietsma, 2013). Newly proposed models are usually adjustments to the K-M equation with the addition of different parameters to obtain similar trends to the experimental findings (Bubnoff, Carvalho, de Castro, & Lourenço, 2016; S.-J. Lee & Van Tyne, 2011; Mustak et al., 2016; Caner Şimşir & Cemil Hakan Gür, 2008). For instance, Şimşir et al. have added a term representing the amount of remaining austenite in the case where there is more than one phase transformed during cooling, such as bainite and pearlite (Caner Şimşir & Cemil Hakan Gür, 2008). Lee et al. have proposed the addition of an exponent to the K-M equation in order to model more accurately the onset of transformation (S.-J. Lee & Van Tyne, 2011). Li et al. have included a correctional term to adjust the differences observed in the predicted martensite volume fractions in comparison with experimental results (Y. Li, Xu, Jin, & Lu, 2015).

In more recent studies, changes in the kinetics of martensitic transformation have been reported (J. H. Liu, Binot, Delagnes, & Jahazi, 2021; Loewy et al., 2014; Peng, Xu, Han, & Gu, 2019; Tao, Han, & Gu, 2015; Villa et al., 2014). These appear in the form of steps on the dilatometry curve and are described as decelerations that occur during phase transformation. This phenomenon has become more visible when the cooling rates *after* M_s are much slower. With these findings, modeling with the conventional K-M equation has proven to be inaccurate as it cannot model a multi-staged transformation.

The variation of carbon concentration in austenite before and during quenching influences the rate of transformation parameter in the K-M equation. Bhadeshia et al. have proposed the usage of two K-M equation in order to model a transformation of two martensite with different M_s by setting up proper boundary conditions for each equation (Bhadeshia, 2013). Liu et al. have proposed a single equation using a K-M equation coupled with a sigmoid shape equation to avoid such restrictions (J. H. Liu et al., 2021). Kaar et al. have developed a model for the

prediction of the microstructural evolution in a quench and partitioning process (Kaar, Krizan, Schneider, & Sommitsch, 2022). Their newly developed model addresses the importance of taking into account the stabilization of austenite due to carbon enrichment. Their work follows the original idea proposed by Hsu et al. who suggested the addition of 2 parameters to the K-M equation describing the carbon concentration before and after quenching for low-carbon steels (Hsu, 1995). However, oftentimes, as the equations are in their integral form, the models can only be used if the whole history of the quenching cycle and its dilatation are known. Such information is very rarely available and therefore, the application of these models at the industrial scale are very limited.

In this paper, to overcome the limitations of the previously stated models, the kinetics of martensitic transformation is modeled by differential equations. The deceleration is addressed by modeling the continuous carbon enrichment of the remaining untransformed austenite due to the partitioning of carbon from the fresh martensite (Caballero et al., 2003; J. H. Liu et al., 2021). This approach allows for a more accurate modeling of the martensitic transformation for an anisothermal cooling.

4.2 Experimental Procedures

4.2.1 Material and Dilatometry

The usual method to assess the kinetics of martensitic transformation is by dilatometry as it elegantly relates, in real time, the change in dilatation to the phase transformation that takes place. In the present work, a high-resolution Bähr DIL 805A/D dilatometer was used for the experiments. The investigated material is a wrought low alloy medium carbon steel cut from an industrial slab whose chemical composition (wt. %) is shown in Table 4.1. As per the standards of the equipment, specimens were machined to a cylindrical shape with dimensions of 4 mm in diameter and 10 mm in length. All specimens prior to quenching had the same heating and holding conditions of 1.5 $°Cs^{-1}$ to 875 °C and soaked for 5 min, under vacuumed condition. With the usage of helium as a cooling medium, the initial part of the quenching

process was similar for all specimens with a cooling rate -2.5 °Cs^{-1} until the temperature reached 300 °C. This temperature is less than 5 degrees above the M_s, estimated from our preliminary experiments with the same steel. From this temperature, different subsequent cooling rates were then used until room temperature: -2.5 °Cs^{-1}, -0.6 °Cs^{-1}, -0.3 °Cs^{-1} and -0.2 °Cs^{-1}. Throughout the rest of the paper, the mentioned cooling cycles will be referred to as CR1, CR2, CR3 and CR4, respectively. The complete heat treatment cycles are shown in Figure 4.1. The blue area represents the initial cooling which is similar for all four samples and the green area, the subsequent coolings.

Table 4.1 Chemical composition of the investigated steel (wt. %)

Fe	C	Mn	Si	Ni	Cr	Mo	V
Balance	0.43	0.69	1.55	1.79	0.81	0.39	0.071

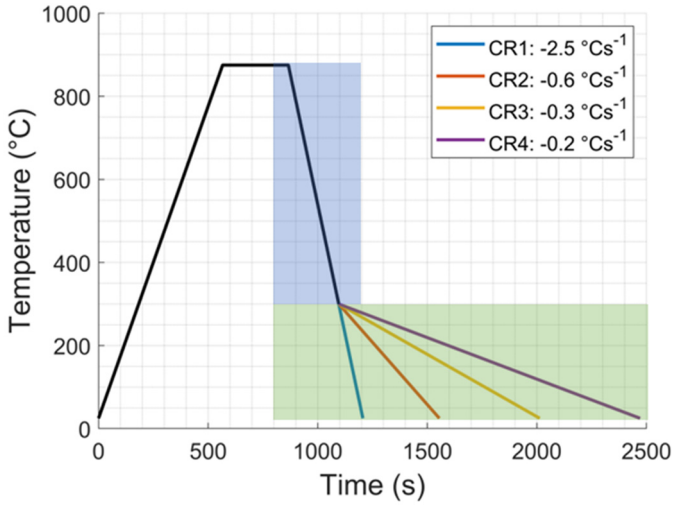

Figure 4.1 Complete heat treatment cycles for each specimen with a similar heating rate and soaking time used for all specimens

4.2.2 SEM and EBSD

After dilatometry experiments, the samples were cut along their longitudinal direction for microstructural observations. They were manually ground to P4000 SiC grit paper, polished

down with a 1 µm diamond solution and ion-milled for 30 min with an Ion Beam Milling System (IM4000Plus, Hitachi). SEM observations and EBSD measurements were conducted in a scanning electron microscope, SU8230 Cold Field Emission SEM, equipped with a Bruker e-Flash EBSD detector and a quad energy-dispersive X-ray spectroscopy detector (QUANTAX FlatQUAD). The annular design for high solid angle (>1.1 sr) and the high-count rate (up to 2.4 million cps) of quad detectors allows for an efficient and precise analysis of fine particles. The operating parameters for EBSD were an accelerating voltage of 20 keV, a current of 25 µA and a step size of 0.11 µm. For SEM observations, the samples were etched for 7 s using a 5 % Nital solution.

4.3 Modeling Approach

The different cooling rates employed under M_s serve to quantify the effect of time on the kinetics of martensitic transformation. The basic rationale of our model is that carbon partitioning from martensite, formed by the initial austenite phase, can occur during the cooling stage after the M_s point is reached (i.e., 300 °C) through an auto-tempering process (Ooi, Cho, Oh, & Bhadeshia, 2013; van Bohemen & Sietsma, 2014). The diffusion of carbon ensues from the supersaturated martensite laths to the remaining untransformed austenite. The continuous carbon enrichment of the austenite contributes to its stability (Hsu, 1995; Ribamar et al., 2023; Speer, De Moor, & Clarke, 2014; van Bohemen & Sietsma, 2014). This stability affects the M_s which evolves and decreases constantly during the cooling treatment process. Therefore, once the M_s decreases sufficiently and surpass the current temperature, the transformation halts or ceases completely. This has been described in the present work as decelerations in the kinetics of martensitic transformation. A higher degree of undercooling is then required and once the temperature reaches the M_s anew, the transformation pursues and is described as the acceleration. However, if the quenching process is completed in a very short duration or is accomplished with very high cooling rates, this phenomenon has very little impact as the movement of carbon atoms is very limited within this timeframe. For this occurrence, no decelerations would then be apparent on the dilatometry curves as martensite is formed from the same homogenized austenite.

The modeling approach proposed in this paper revolves around the above depiction of martensitic transformation: a displacive transformation process with an underlying *diffusive* mechanism which affects its rate of progress. It is important to emphasize that, despite the incorporation of a diffusional mechanism, the discussed martensitic transformation isn't considered as a diffusional transformation. Therefore, the progress of the martensitic phase transformation is only driven by the degree of undercooling or a change in temperature. Moreover, the model only considers a quenching process for which intermediate phases such as pearlite and bainite are not permitted and the transformation is from austenite to martensite.

It must be noted that as the focus of the study was on the kinetics of martensitic transformation after M_s, with the view to avoid 'overloading' the modeling work with second order parameters, some variables were considered constant. For example, only one austenitization temperature was used resulting in one prior austenite grain size; while, it is well-known that it modifies the M_s (Celada-Casero et al., 2019; H. Yang & Bhadeshia, 2009). A second consideration is that possible formation of carbides does not induce any significant measurable dilatation for which a constitutive equation would be needed. It has been demonstrated that the loss of tetragonality during tempering of martensite produces very minor effect on the dilatometry curve (Grajcar, Morawiec, Jimenez, & Garcia-Mateo, 2020; J. H. Liu et al., 2021); therefore, volume loss due to partial loss of tetragonality during very slow cooling rate tests was not considered in the model. Lastly, carbon is considered as the only element that is partitioned during the transformation. Therefore, the effect of other alloying elements is averaged in the constitutive equations of carbon concentration evolutions.

4.3.1 Koistinen-Marburger and Phase Fractions

The current model describes the interaction of two phases, austenite and martensite, influenced by temperature and time with a focus on carbon diffusion from martensite to austenite during transformation. From a phase balance point of view, the total fraction should stay the same

regardless of the cooling route. Eq.(4.1) refers to the fractions for both phases with f_m and f_a corresponding to the fractions of martensite and austenite, respectively.

$$f_m + f_a = 1 \tag{4.1}$$

The equation used for the prediction of martensite fractions is presented in Eq.(4.2). It is the standard K-M equation, modified with the addition of a parameter f_{max} representing the maximum fractions of martensite that can be obtained. This parameter, as shown in Eq.(4.3), allows for the incorporation of the retained austenite (R_a) as a function of the cooling rate, which will be discussed later. Unlike the standard K-M equation, the parameters representing the rate of transformation (Ω), and the material characteristic M_s are not considered as constants. The decrease in M_s is taken into consideration in the K-M equation. It is modeled as a function of the carbon concentration in austenite. As for Ω, for many years, it was assumed that the rate of transformation was constant and had a value of 0.011 K^{-1}, regardless of the composition of the steel. It has been proven, however, that such value is not accurate for steels of different compositions (van Bohemen & Sietsma, 2013). In this case, it was also modeled as a function of the carbon content in austenite.

$$f_m = f_{max}\left(1 - \mathrm{e}^{-\Omega\,(M_s - T)}\right) \tag{4.2}$$

$$f_{max} = 1 - R_a \tag{4.3}$$

4.3.2 Martensite Start Temperature and Rate of Transformation

With a higher carbon concentration in austenite, the M_s can not be considered equal to the initial M_s, as assumed in the conventional K-M model. Generally, the M_s decreases with additional alloying elements or with higher carbon concentrations (Capdevila, Caballero, & García De Andrés, 2013; Frenzel et al., 2015; Chengcheng Liu, Huang, Ren, Ren, & Zhang, 2022). Therefore, the evolution of M_s is expressed as a decrease with increasing carbon

concentration in austenite, x_a, as shown in Eq.(4.4). Here, M_{s0} represents the initial temperature where martensite first starts to transform with its corresponding initial carbon concentration x_0 (0.43 wt. % as shown in Table 4.1). The parameter C is a material constant describing the change of M_s. It is also from this basis that the deceleration of the kinetics is described. If M_s decreases sufficiently, it is possible to completely halt the transformation.

$$M_s = M_{s0} - C\ (x_a - x_0) \tag{4.4}$$

The rate of transformation parameter (Ω) had been a constant value for each specific steel. However, with the same explanation as M_s, as the material changes constantly, the parameter Ω must change according to the carbon concentration of austenite. van Bohemen et al. have determined the values of Ω for different steels (van Bohemen & Sietsma, 2013). It is shown that its value decreases with higher carbon concentrations. Therefore, to consider the evolution of carbon concentration in austenite, a new relation is proposed and shown in Eq.(4.5). In this equation, Ω_0 is the initial rate of transformation parameter and Q is a material constant describing the change of Ω as a function of x_a.

$$\Omega = \Omega_0 - Q\ (x_a - x_0) \tag{4.5}$$

It must be reminded that carbon is not the only element whose concentration in austenite could change and other elements therefore affect Ω; however, their contributions are assumed to be much less and are not considered in the modeling and the variations of Ω are approximated solely by the change in carbon concentration.

4.3.3 Carbon Enriched Austenite

Upon reaching the initial M_s, a certain fraction of martensite is formed. Due to the slow cooling regimes of CR2 to CR4, carbon atoms from the supersaturated martensite could partition to the remaining austenite. The rate of transfer is described by an increase in carbon concentration

for the remaining austenite. The expression of this rate of increase is shown in Eq.(4.6) where the term $D\mathrm{e}^{\frac{-E}{RT}}$ share a similarity to a diffusion coefficient, but with different units. This coefficient varies as a function of temperature. D and E are material constants and R is the universal gas constant. The second term, $\left\langle \frac{T-T_{eq}}{T_{eq}} \right\rangle_{+}^{L}$ is used as an equilibrium condition where T_{eq} represents the equilibrium temperature in Kelvin and is also considered as a constant. The temperature T is in Kelvin as well, with $T > T_{eq}$. Upon reaching this equilibrium temperature during cooling, the whole process of carbon diffusion would cease.

Lastly, we have the fractions of martensite as well as the fraction of austenite as a dependency. If there is no martensite, then no carbon can be partitioned from as there are only 2 phases and therefore, the fractions of martensite and austenite would not evolve anymore. On the other hand, if there's no more austenite, there's no more sites for carbon to partition into. L, M and N are constant exponents used in order to give an order of importance to each term.

$$\dot{x}_a = D\mathrm{e}^{\frac{-E}{RT}} \left\langle \frac{T-T_{eq}}{T_{eq}} \right\rangle_{+}^{L} (1-f_m)^M \, {f_m}^N \tag{4.6}$$

4.4 Results

4.4.1 Dilatometric Results

The complete dilatometry results for all four corresponding heat treatment cycles are shown in Figure 4.2(a). For the interest of this paper, Figure 4.2(b) shows the enlarged area corresponding to the martensitic transformation encapsuled within the dashed rectangle of Figure 4.2(a). Only the results relevant to the cooling are shown. The difference in the kinetics for all four cooling rates is clearly apparent. For fast cooling rates such as CR1, the conventional reverse S shape is quickly recognizable. For CR2 to CR4, which requires a longer duration to cool to room temperature, a gradual and steady decrease in the initial transformation

is observed which corresponds to the deceleration. The degree of deceleration is also dependent on the cooling rates as evidenced by CR4, where the first step of the transformation is noticeably lower than the others. Furthermore, the final length at room temperature is not the same. Visually, the decrease in length is estimated to be proportional to the duration required to cool to room temperature.

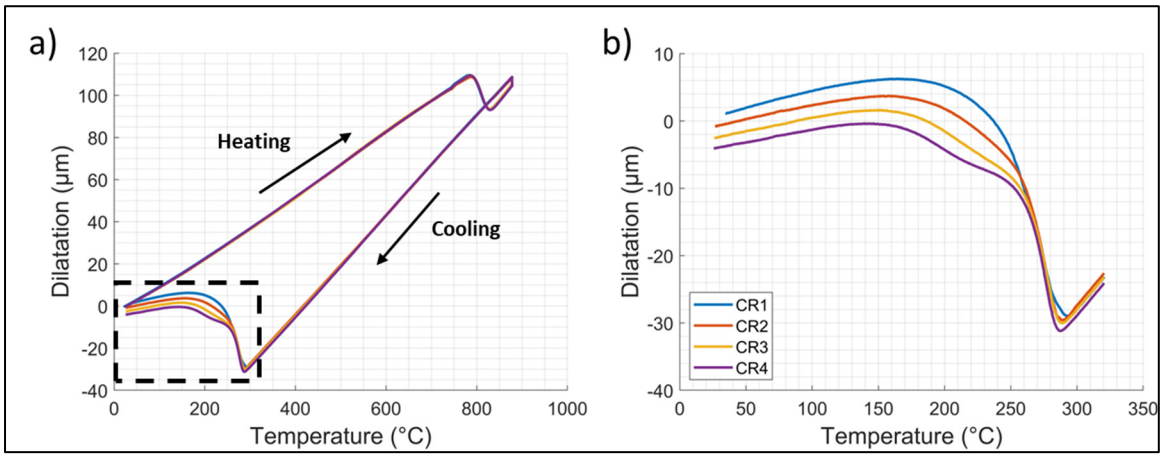

Figure 4.2 (a) Complete dilatation curves obtained from the thermal cycles presented in Figure 4.1; (b) Enlarged area of the dilatation curves corresponding to the martensitic phase transformation

From dilatometry curves, the measured dilatations are used to quantify the amount of austenite and martensite during cooling. The conversion of dilatation into fractions is accomplished using the lever rule method and the coefficient of linear thermal expansion of each phase (Isasti, Jorge-Badiola, Taheri, & Uranga, 2013; L. Liu & Guo, 2021). For simplification purposes, the linear thermal expansion coefficients of both phases are considered constants and measured using the dilatation curves. The conversion would then be calculated according to Eq.(4.7). Furthermore, it is well known that the amount of R_a increases with slower cooling rates due to the increase in stability (Morawiec, Wojtacha, & Opiela, 2021; Schastlivtsev, Kaletina, Fokina, & Kaletin, 2014). This behaviour is consistent with the observed final length at room temperature which decreases with slower cooling rates. Thus, the length differences at room temperature, in comparison from one dilatation curve to another, can be interpreted as

additional amounts of R_a. For this matter, CR1 was taken as reference in the determination of R_a for CR2, CR3, and CR4.

$$f_{m,i} = \frac{\Delta L(T)_{CRi} - \Delta L(T)_{a,\,CRi}}{\Delta L(T)_{m,\,CR1} - \Delta L(T)_{a,\,CRi}} \tag{4.7}$$

$$R_a = F\ \mathrm{e}^{G\,\dot{T}} \tag{4.8}$$

Here, $f_{m,i}$ refers to the fraction of martensite of the investigated CR curve i, with $i \in [1, \dots, 4]$ going from 1 to 4 (four curves). $\Delta L(T)_{CRi}$ is the dilatation of the same CR curve i and a and m, refers to the phase austenite and martensite. In this paper, as CR1 displays a conventional reverse S shape curve during transformation without any visible deceleration, it is assumed that it produces a fully martensitic microstructure, hence the comparison to $\Delta L(T)_{m,\,CR1}$ in Eq.(4.7). With proper measurements of retained austenite through x-ray diffraction or magnetic field, results can be later rescaled. These measurements have not been done as it was not the focus of this study. The result of the conversion using the lever rule is shown in Figure 4.3(a). Using Eq.(4.7), the calculated total fractions of martensite are 100 %, 99.59 %, 98.29 % and 97.69 % for CR1 to CR4, respectively. Complementary to the fractions of martensite, the determined amount of R_a is of 0 %, 0.41 %, 1.71 % and 2.31 %.

As the R_a increases with slower cooling rates, an exponential type equation, Eq.(4.8), was determined which models closely the experimentally calculated R_a. R_a represents the fractions of retained austenite, F and G are material constants and $\dot{T}$ is the cooling rate. The calculated fractions of R_a are plotted as a function of the cooling rates in Figure 4.3(b). As mentioned previously, the maximum fraction of martensite was calculated based on the amount of R_a. The values of the parameter F and G were acquired using a best fit approach. The obtained values are 0.0624 and 3.716 for F and G, respectively. The evolution of retained austenite modeled based on Eq.(4.8) is shown as the red plot in Figure 4.3(b).

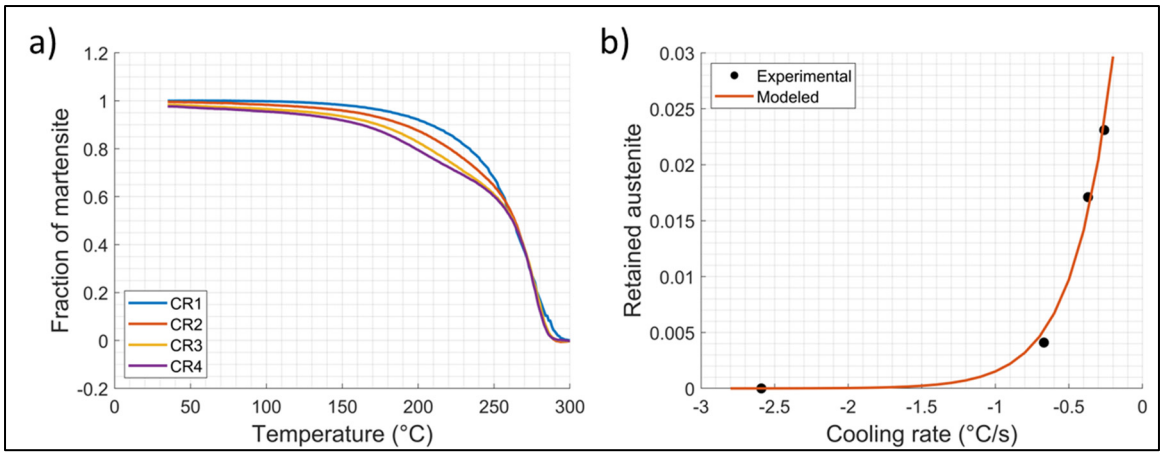

Figure 4.3 (a) Fractions of martensite as a function of temperature; (b) Each point represents the fraction of retained austenite at room temperature calculated from the length differences and modeled by the red curve

4.4.2 Microstructural Observations

The microstructure for each sample (CR1 to CR4) was investigated by SEM and shown in Figure 4.4. The microstructure consists of martensite laths formed in packets and blocks enclosed within a prior austenite grain. Carbides could also be seen in all four samples as small bright dots. However, a noticeably higher amount of carbides can be observed on slower cooling rates, such as CR3 and CR4, as indicated by the white arrows in Figure 4.4(c-d). This indicates that carbides precipitate during cooling and auto-tempering. The carbides were cementite enriched in Cr and Mo elements (Clarke et al., 2014; Ning et al., 2021; Zhu et al., 2007). They were identified via energy dispersive X-ray spectroscopy (EDS) using the quad detector that has the capability to analyze particles as fine as 6-8 nm (Terborg et al., 2017). Figure 4.5 shows the analysis for CR3. Only CR3 is shown here as an example. The sizes of these carbides were measured to be around 150-300 nm and had a spheroidal shape.

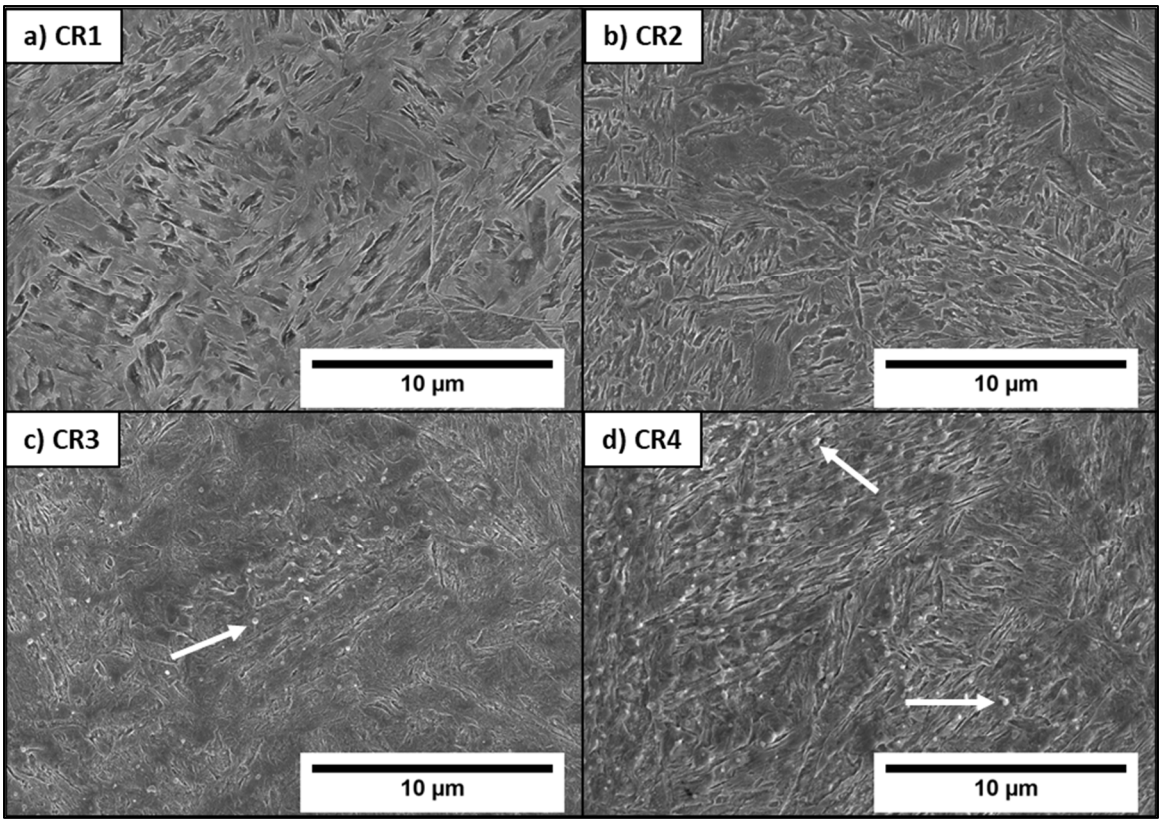

Figure 4.4 SEM micrographs of all 4 samples where a higher number of carbides can be observed for slower cooling rates such as CR3 and CR4

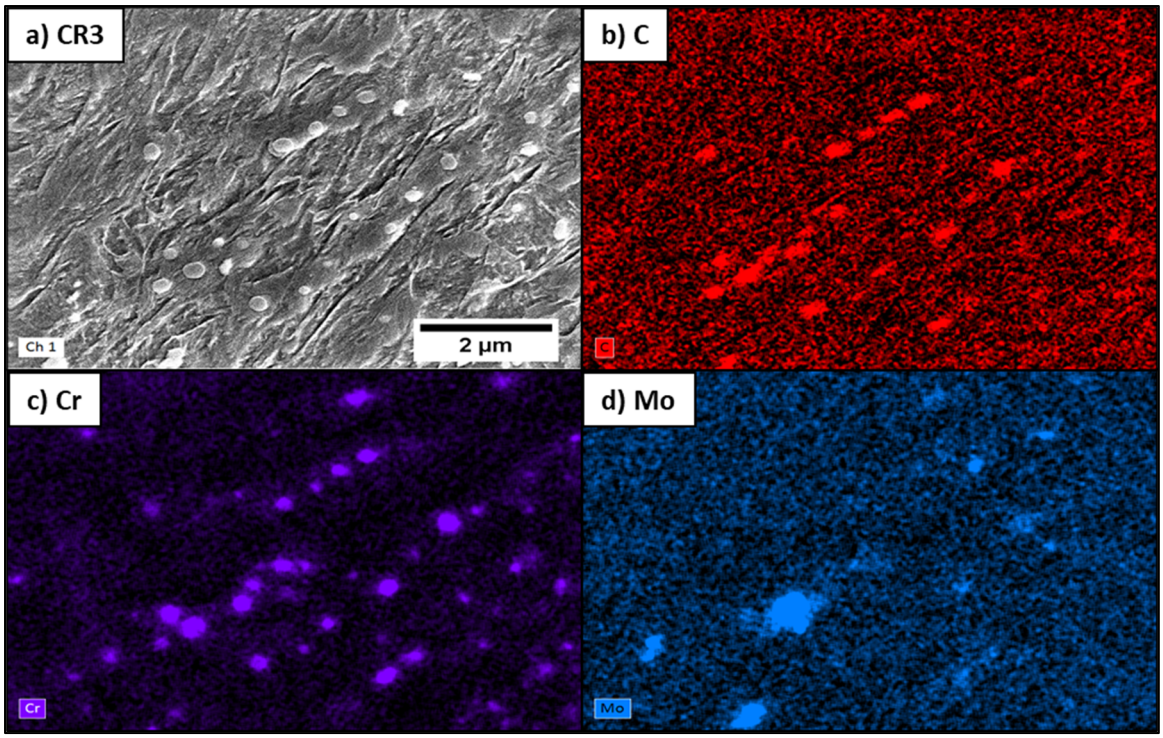

Figure 4.5 (a) SEM with visible precipitates; (b-d) EDS analysis showing the presence of C, Cr and Mo

The inverse pole figure (IPF) maps in the reference of the axis direction are shown in Figure 4.6. The prior austenite grain boundaries were reconstructed using the crystallographic orientation relationships of austenite and martensite following Kurdjumov-Sachs model using the MTEX 5.8.2 companion toolbox in MATLAB (Graf, Kuntz, Autenrieth, & Müller, 2020; Gyhlesten Back & Engberg, 2017). The threshold misorientation for high angle boundaries was set to 10° and the boundaries between martensite blocks were manually removed. The results show a similar grain size for all 4 samples, averaged at around 25 µm. Additionally, corresponding SEM images of the area is provided for CR1 and CR4, as seen in Figure 4.6(b,f). The SEM images were registered to the IPF maps using an affine transformation.

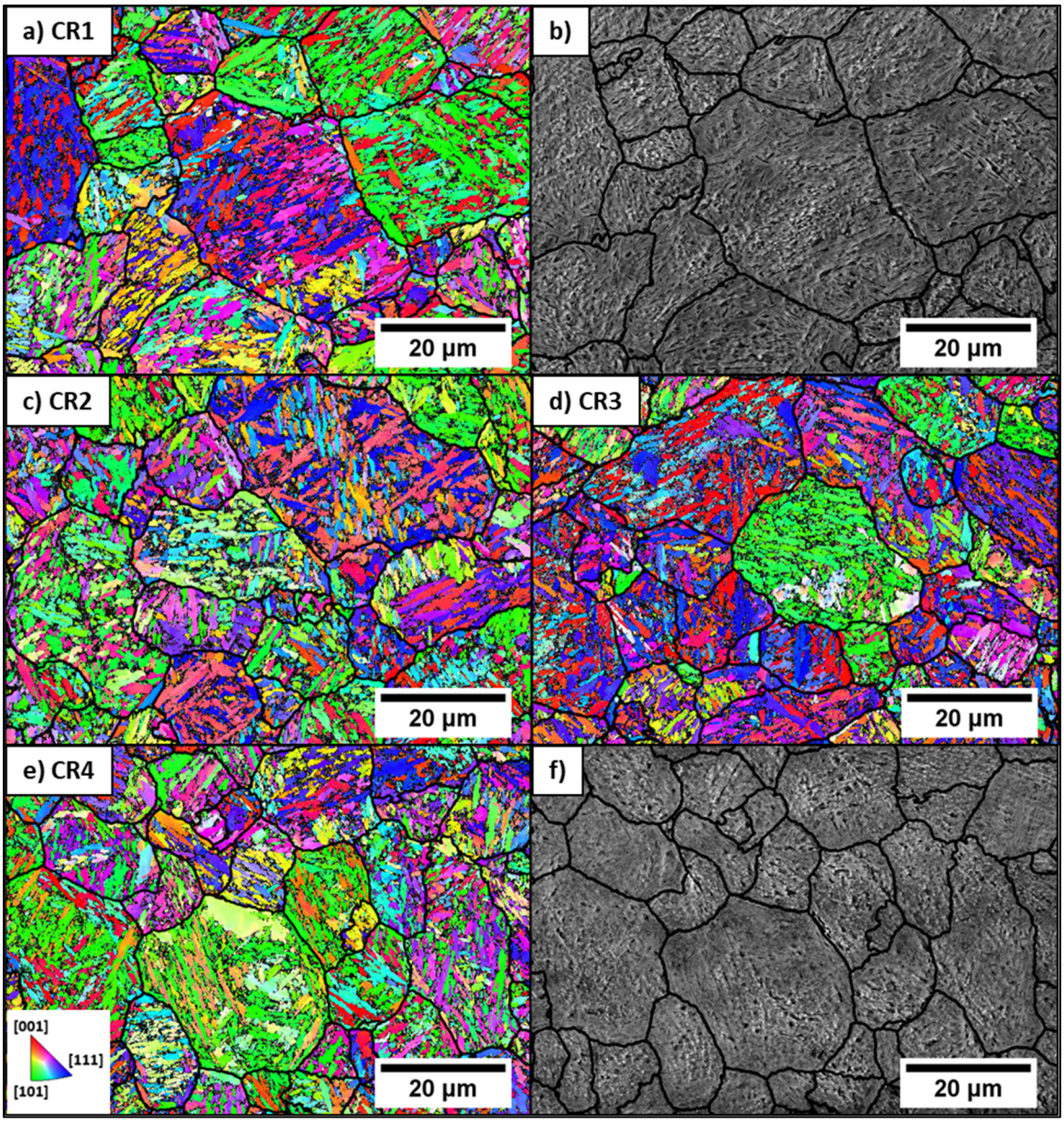

Figure 4.6 IPF maps of all 4 samples in the axis direction; b) and f) show the corresponding SEM maps for CR1 and CR4

4.4.3 Modeling of the Kinetics of Martensite Transformation

As the simulation is executed for any given moment in time, it is necessary to have the fraction of martensite transformed calculated based on the material state in that instance. Therefore, the

K-M equation previously established is now developed to its derivative form (Eq.(4.9)). This insures a proper prediction of the fraction of martensite regardless of the cooling rate, whether it's constant or not.

$$\begin{aligned}\dot{f}_m &= \frac{\partial f_m}{\partial T}\frac{\partial T}{\partial t} + \frac{\partial f_m}{\partial M_s}\frac{\partial M_s}{\partial t} + \frac{\partial f_m}{\partial \Omega}\frac{\partial \Omega}{\partial t} + \frac{\partial f_m}{\partial f_{max}}\frac{\partial f_{max}}{\partial t} \\ \dot{f}_m &= \left\{-\dot{T}\, f_{max}\, \Omega\, \mathrm{e}^{-\Omega\,(M_S - T)}\right\} \\ &+\left\{-C\, \dot{x}_a\, f_{max}\, \Omega\, \mathrm{e}^{-\Omega\,(M_S - T)}\right\} \\ &+\left\{-Q\, \dot{x}_a\, (M_S - T)\; f_{max}\, \Omega\, \mathrm{e}^{-\Omega\,(M_S - T)}\right\} \\ &+\left\{\ddot{T}\left(1 - \mathrm{e}^{-\Omega\,(M_S - T)}\right)\left(-F\, G\, \mathrm{e}^{G\,\dot{T}}\right)\right\}\end{aligned} \tag{4.9}$$

As the equations are condition dependent, the prediction of the martensite transformation is programmed as a routine with a schematic illustrated in Figure 4.7. The routine starts during cooling and as the temperature reaches the M_s, initial fractions of martensite, also called fresh martensite, start to form. If the cooling is slow enough, the constant enrichment increases the carbon concentration in the remaining austenite which lowers the M_s. If the cooling temperature hasn't reached the equilibrium temperature T_{eq}, it means that the enrichment continues and lowers the M_s furthermore which in return lowers the degree of undercooling. When the temperature is low enough, carbon diffusion is deemed too slow and therefore the enrichment ceases. However, transformation can still take place if the temperature is lower than the constantly decreasing M_s. Finally, once the total fraction of austenite, available for transformation has been reached, the routine ends.

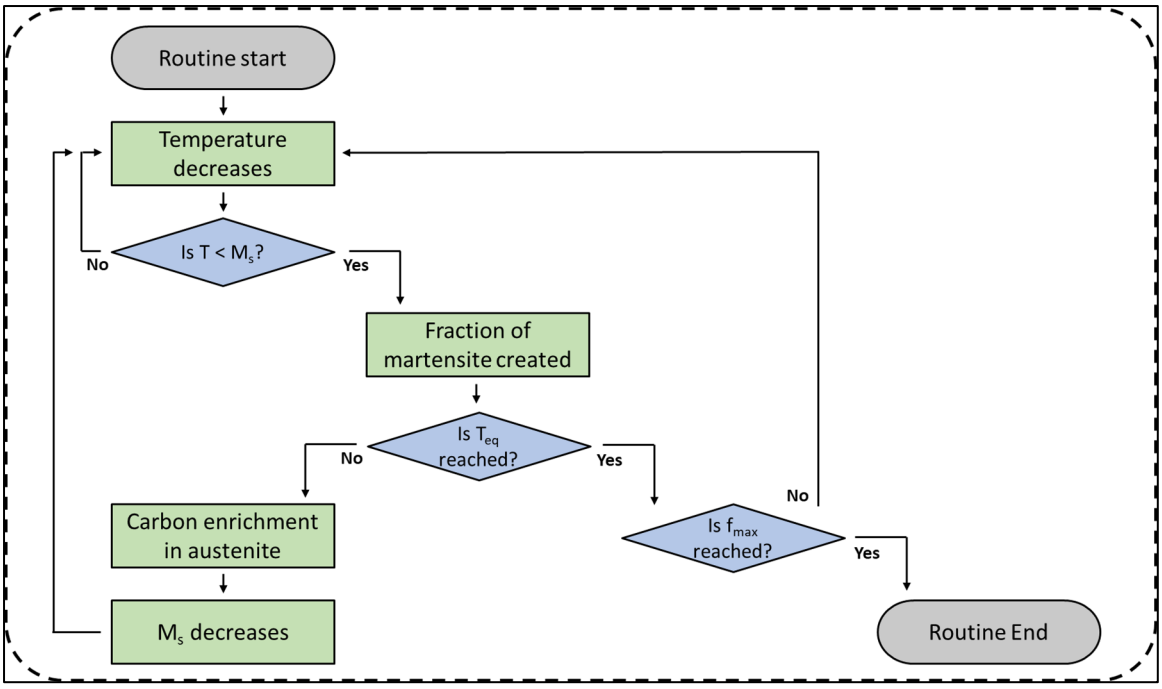

Figure 4.7 Flowchart used to predict the martensite phase transformation during a quenching process with blue diamond boxes being condition and verification boxes

In order to run this routine, several parameters and material constants are required. Using the results obtained from dilatometry, an optimization process was performed using the same routine. This optimization identifies the best parameters for the lowest summation error from the differences obtained experimentally and from the model. The optimization process is performed only on the experimental values of CR3. These parameters and constants are material related and independent of the cooling route. Therefore, the same values identified for CR3 are also applied to CR1, CR2 and CR4. The choice of CR3 as the parameter's identification candidate was arbitrary. The best values for all the required parameters obtained after optimization are reported in Table 4.2.

Table 4.2 Extracted values for parameters and constants used in the routine model

Ms_0 (K)	C (C wt. % K)	Ω_0 (K^{-1})	Q (C wt. % K^{-1})	D (C wt. % s^{-1})
558.4	18 939	0.0327	8.337	288.5
E (J mol^{-1})	L	M	N	T_{eq} (K)
41 844	1.56	2.64	8.07	385.8

All four cooling rates were modeled by applying the values of the parameters as entry values to the proposed routine. The results are shown in Figure 4.8. As observed, the current model provides an accurate prediction of the kinetics of martensitic phase transformation where decelerations and accelerations are not negligible, i.e., stages of transformation are observed. This is because the microstructural evolution is determined at every step of the quenching process and the ongoing transformation is solely dependent on the time and temperature variables.

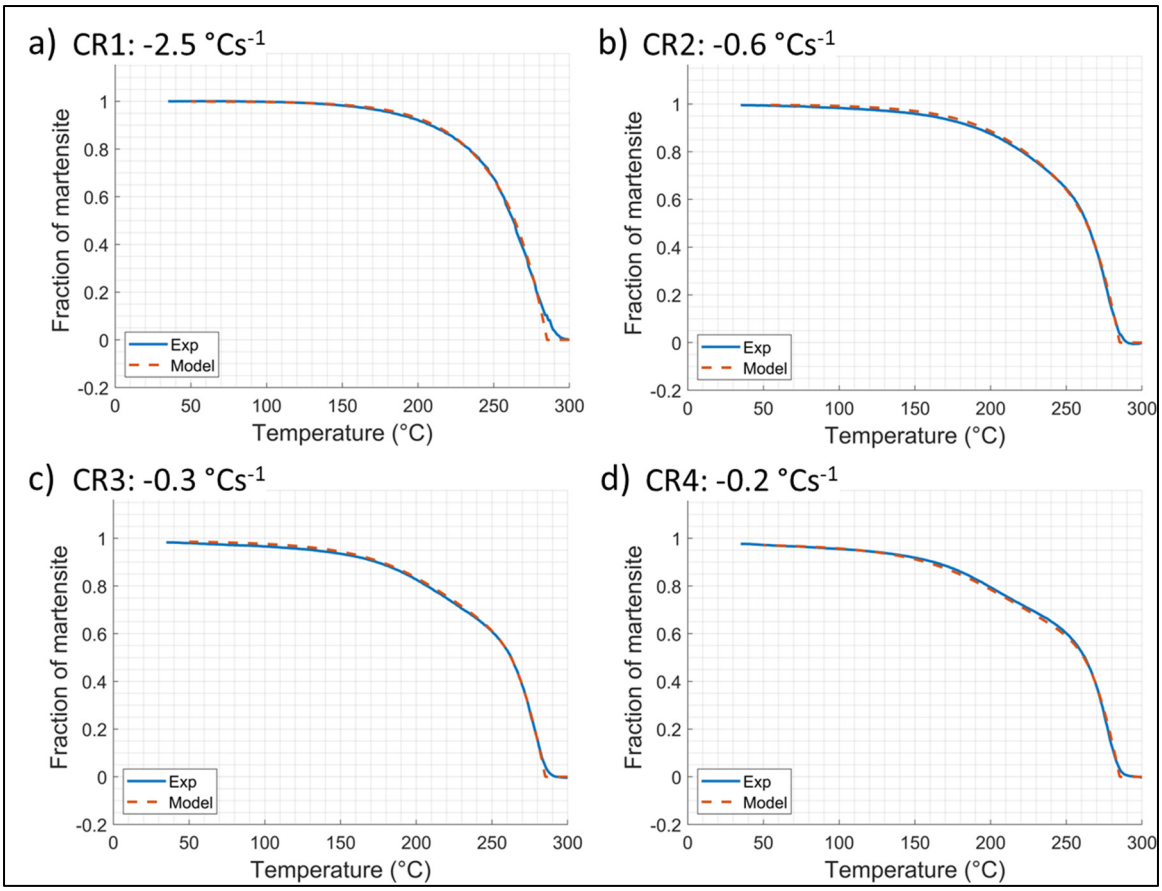

Figure 4.8 Comparison of the kinetics of martensitic transformation from results obtained by dilatometry and the martensitic phase transformation model proposed in this paper

The evolution of the carbon concentration is shown in Figure 4.9. With slower cooling rates, more time is available for carbon partitioning, increasing its concentration significantly in the remaining austenite. The highest concentration attained is close to 0.54 % for CR4 which is also the cooling rate with the most pronounced deceleration. Furthermore, CR1 shows an increase in concentration from the initial value of 0.43 % to 0.44 % despite not showing any signs of deceleration in the dilatometry curve. As mentioned earlier, within the duration of the transformation, this increase of 0.01 % is insignificant to the evolution of M_s, from 558.4 to 556.5 K (285.3 to 283.4 °C).

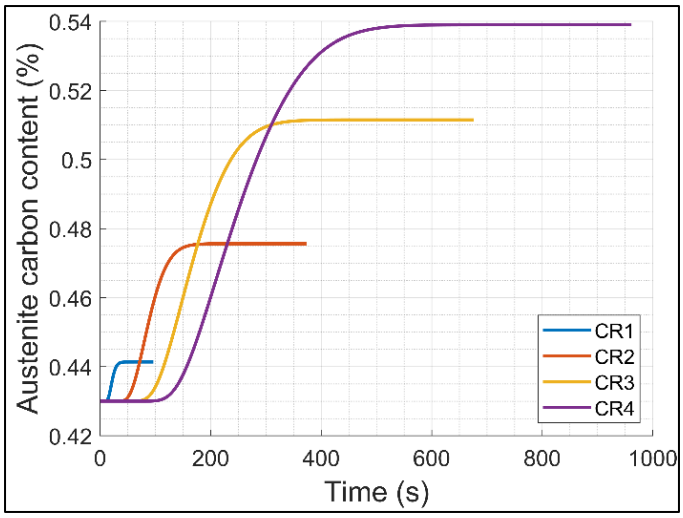

Figure 4.9 Evolution of the carbon concentration in the remaining austenite during cooling calculated from Eq.(4.6)

A deceleration doesn't necessarily mean that the temperature must be lower than M_s. In fact, examining Eq.(4.9) shows that the rate at which martensite is formed is dependent on the terms $(M_s - T)$ which is the degree of undercooling. As this difference in temperature gradually decreases, due to the decreases of M_s, a deceleration is perceived. If the temperature is above the M_s, then the transformation ceases. Figure 4.10(a) shows the evolution of M_s for CR3 as a function of the actual cooling temperature where an apparent change is observed in the time range of 100 s to 300 s.

This degree of undercooling is present in all 4 partial derivative equations, and all have independent impact to the overall rate of transformation. Figure 4.10(b) shows the rate of transformation for each partial derivative as a function of time. Without considering carbon enrichment, the rate of transformation would be entirely modeled by the blue curve, which is the standard K-M equation. However, as shown by the red, yellow, and green curves, the effect of carbon enrichment decreases the rate of transformation. As for the purple curve, it had no influence on the rate of transformation as all dilatometry tests were performed using constant cooling rates below M_s. Only the results of CR3 are shown as an example.

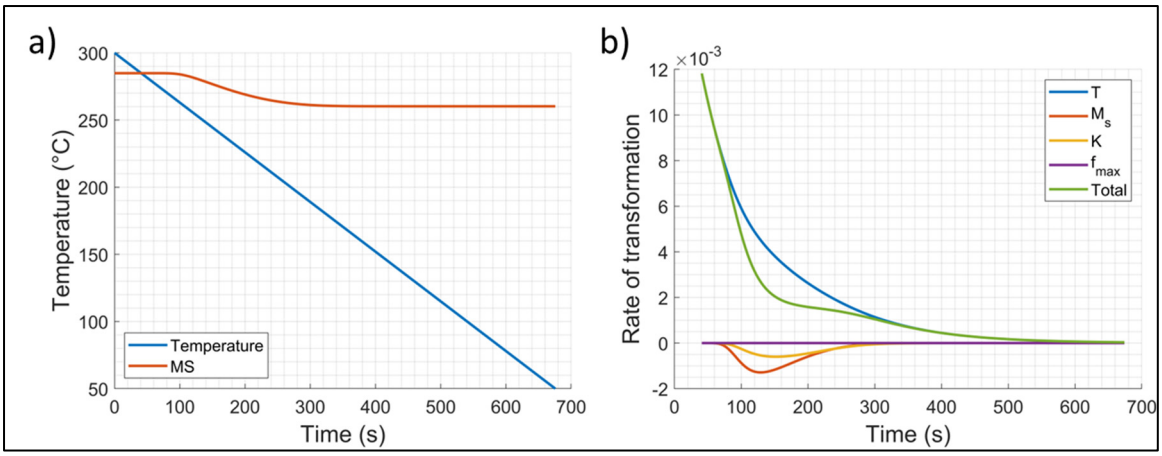

Figure 4.10 (a) Comparison between the M_s and the actual temperature during cooling for the case of CR3; (b) The rate of transformation of each partial derivative

4.5 Discussion

The study on carbon partitioning during martensite transformation is a surging interest for researchers. Newly developed models tend to include a diffusion process for the partitioning of carbon during quenching (Kaar et al., 2022; Pohjonen, Ramesh Babu, & Visuri, 2022). This carbon partitioning and austenite enrichment has also been studied via atom probe (T. Kohne, Dahlstrom, Winkelmann, Hedstrom, & Borgenstam, 2022; Ribamar et al., 2023). Kohne et al. have investigated the change in tetragonality for martensite and showed that a slower cooling rate led to a more important loss of tetragonality when the cooling rate decreases (Thomas Kohne et al., 2023). This partial loss of tetragonality was attributed to the diffusion of carbon due to an auto-tempering process that takes place progressively as the cooling rate is decreased The presence of carbides in the current study despite the high content of silicon, which is known to be a carbide suppressor, is consistent with the findings of other authors, with concentrations of silicon as high as 2.2 % (HajyAkbary, Sietsma, Miyamoto, Furuhara, & Santofimia, 2016; Pierce et al., 2015; Toji, Miyamoto, & Raabe, 2015). Furthermore, the role of silicon addition was discussed by Kim et al. (Kim, Sietsma, & Santofimia, 2017). It was shown that carbides precipitate regardless of the silicon content during tempering and a stabilization of austenite with delay decomposition was noticed in the steel with added silicon.

While there are numerous methods for predicting the martensitic transformation through modeling, most of them are unable to accurately model a two-stage transformation. Moreover, those methods only work when the entire cooling route is known beforehand (Bhadeshia, 2013; J. H. Liu et al., 2021). Therefore, the parameters are only valid for a very specific cooling condition which limits severely their usage. Models that do consider for carbon partitioning focus more on the decomposition of retained austenite during the partitioning or tempering processes (Y. Zhang, Gu, Han, Shen, & Li, 2021). In contrast to those methods, the present model focuses on the prediction of the phase transformation coupled with austenite stabilization during cooling. The predicted fractions are then only dependent on the temperature and time. This means that for this specific steel, the values of the parameters stay unchanged regardless of the cooling route.

As for the values of the parameters, the identified value of M_{s0} is slightly under the actual M_s of around 294 °C, estimated from the dilatometry curves. This difference is due to the incapacity of the K-M equation to accurately predict the onset of transformation, hence the addition of an exponent by some researchers (S.-J. Lee & Van Tyne, 2011; Mustak et al., 2016). For clarification purposes, researchers refer the M_s in K-M equation as the theoretical martensite start temperature T_{KM} (van Bohemen & Sietsma, 2014).

For Ω_0, the value optimized is clearly different than the 0.011 K^{-1} proposed initially by Koistinen for carbon steel (Koistinen & Marburger, 1959). It is now well understood that such a value cannot be applied for alloy steels. In this study, the value for the rate of transformation coefficient, Ω, decreases up to 0.0237 K^{-1} for CR4 with a corresponding carbon concentration of 0.54 %. The rate of decrease of Ω, which is positive and identified by the parameter Q, is higher than the findings reported by van Bohemen in Ref. (van Bohemen & Sietsma, 2013). The present value is 0.0836 (C wt. % K^{-1}) whereas the value reported by the above-mentioned study is 0.0107 (C wt. % K^{-1}). This discrepancy could be due to the different alloying elements that were not considered in this study, such as Mn, Ni, Cr and Mo. Seo et al. have also defined the evolution of the rate of transformation coefficient as a function of different alloying

elements (Seo et al., 2016). In their study however, the rate of decrease is negative meaning that higher carbon concentration steels have higher rate of transformation. An attempted explanation for this opposite behaviour is that the interactions between the alloying elements with carbon have not been well documented. Although, it is still unclear if the sign of this parameter is negative or positive due to the lack of studies, in the present model with only one element, the sign must be positive. Examining the values for parameters L, M and N of Eq.(4.6), shows that the rate of change for the carbon concentration is greatly dependent on the fraction of martensite by several orders as it is the source for the amount of carbon atoms that can be partitioned.

Regarding the equilibrium temperature, T_{eq}, the identified value is 385.8 K or 112.6 °C. It is known that the coefficient of diffusion is highly dependent on the temperature, the higher the temperature, the easier the diffusion. However, most studies focus on temperature ranges above 500 °C (Thibaux, Métenier, & Xhoffer, 2007). Therefore, finding any reference for our identified value was very difficult. Nonetheless, several studies have performed tempering procedures as low as 150 °C (Firrao, Matteis, & De Sario, 2019). This suggests that although carbon partitioning can still occur even at such a low temperature, its mobility is very slow (Mondière, 2018).

4.6 Conclusion

In this study, a model is proposed to accurately predict the kinetics of martensitic transformation with two-stage transformation. As opposed to other models which require a full history of the cooling route, the current model has the benefit of being in the derivative form. This allows for an accurate prediction of martensite fractions regardless of the cooling route. Furthermore, the predictions are made using the instantaneous state of the material which evolves in time. The model is based on the following assumptions, observations, and characteristics:

- The K-M has been used for the determination of the phase fractions. However, the rate of transformation parameter and the M_s are not considered as constants.

- A new equation for the evolution of the carbon concentration of austenite is proposed. The increase in carbon concentration is dependent on the temperature, the fraction of martensite and austenite.

- The increase in carbon concentration in the remaining austenite leads to its stabilization. This decreases the M_s and in return decreases the fractions formed.

- The increase in carbon concentration in the remaining austenite also decreases the rate of transformation parameter.

- Finally, the whole model is developed in its derivative form which allows for a better prediction of the kinetics of martensitic transformation for an anisothermal quenching process.

CHAPTER 5

A COMPREHENSIVE SEMI-EMPIRICAL MODEL PREDICTING THERMO-MECHANICAL BEHAVIOR DURING QUENCH OF A HIGH-STRENGTH STEEL

Jia Hong Liu[a], René Billardon[b], Denis Delagnes[c], Morteza Sadeghifar[d], Henri Champliaud[e], Antoine Tahan[f], Mohammad Jahazi[g]

[a, d, e, f, g] Department of Mechanical Engineering, École de technologie supérieure, 1100 Rue Notre-Dame Ouest, Montreal, H3C 1K3, QC, Canada

[b] Safran Group, Safran Transmission Systems, 18 boulevard Louis-Seguin, 92707 Colombes Cedex, France

[c] Institut Clément Ader (ICA), Université de Toulouse, CNRS, IMT Mines Albi, UPS, INSA, ISAE-SUPAERO, Campus Jarlard, 81013 Albi CT Cedex 09, France

Paper submitted for publication in *Mechanics of Materials*, June 2023

Abstract— Accurate and reliable prediction of quench-induced distortions requires the determination of the thermo-mechanical properties of the considered material at different stages of the quenching process. In the case of high-strength steels, with the occurrence of phase transformation, the impact of the phases must also be considered. The extracted properties are the Young's modulus, viscous stress, kinematic hardening stress, isotropic hardening stress, the yield stress, and the transformation-induced plasticity (TRIP) parameter for both the austenite and martensite phases. The above properties were determined using the thermo-mechanical simulator, Gleeble 3800. On the basis of the experimental results, models that account for the evolution of each of the identified properties as a function of temperature are proposed. The determination of the constants in each model allows for accurate prediction of quench induced distortion and the quantification of the role of each phenomenon that occurs during quenching.

Keywords— Modeling, Thermo-mechanical Properties, Viscous Stress, Kinematic Hardening Stress, Isotropic Hardening Stress, Yield Stress, Transformation-Induced Plasticity, TRIP Parameter

5.1 Introduction

Distortion is an undeniable issue of any heat treatment process and is often one of the major sources of part rework or rejection, resulting in significant time and energy costs. Therefore, predicting part distortions is of high importance for industry, particularly when it comes to large size critical components where very small distortions are tolerated after the heat treatment process. Material response to the heat treatment cycle is the determining factor for the extent and severity of the distortion which influences the selection of the heat treatment parameters and its geometrical design (Nallathambi et al., 2010; Peterli et al., 2017; C. Şimşir, 2014).

The constitutive equation describing the overall mechanical response is often expressed by the additive decomposition of strain components:

$$\varepsilon = \varepsilon^e + \varepsilon^p + \varepsilon^{th} + \varepsilon^{pt} + \varepsilon^{tr} \tag{5.1}$$

where ε is the total strain, ε^e is the elastic strain, ε^p is the plastic strain, ε^{th} is the thermal strain, ε^{pt} is the phase transformation volumetric strain and ε^{tr} is the phase transformation induced plasticity (TRIP) strain (Pietzsch, Brzoza, Kaymak, Specht, & Bertram, 2005; Shao, Yi, Tang, & Sun, 2022). Therefore, the required material properties/data are phase transformation kinetics, the thermo-physical properties, and the thermo-mechanical properties. Depending on the type of simulation, the thermo-mechanical properties include the determination of the stress components: yield stress, viscous stress, kinematic and isotropic hardening stresses. Additional assumptions are made to simplify the problem by removing some stress components such as the viscous stress during a quenching process (da Silva et al., 2012; de Oliveira, Savi, Pacheco, & de Souza, 2010).

Unfortunately, readily available data for a wide range of steel materials is not accessible. Commercial software, such as JMATPRO, can provide, with some degree of precision, some of the data; however, data on mechanical properties are still scarce and mechanical tests remain the most viable method in the determination of the thermo-mechanical properties needed for

distortion modeling. Moreover, data found in the literature for the same or slightly different material is not always acceptable due to the different manufacturing processes. The usage of material data from different sources as inputs would also lead to a mixture material, referred as “Franken-Material” with possible incompatibilities (Mustak et al., 2016).

Lack of material data or improper modeling leads to inaccurate predictions. For example, the omission of the TRIP effect led to an erroneous prediction of the stress direction, as reported in Ref. (Denis, 1996). This TRIP effect is the observed increase in strains measured during phase transformation (Fischer & Schlögl, 1995). This irreversible and permanent strain can be explained by two mechanisms, the Greenwood and Johnson or the Magee mechanisms (Greenwood & Johnson, 1965; Magee & Paxton, 1966). Although the importance of inclusion of this effect is now well understood, the determination of the TRIP parameter still remains a difficult task (Neubert, Pittner, & Rethmeier, 2016; Simsir, 2017). Moreover, most of the studies often focused on the identification of parameters for one or two stress components, such is the case for the Chaboche hardening model (Hai, Wang, Ban, Li, & Du, 2023; Ramezansefat & Shahbeyk, 2015). In such cases, its validation on a complete stress-strain curve becomes challenging or is sometimes not performed in studies.

The present paper describes a comprehensive decomposition and identification of the total measured stress in terms of stress components consisting of the viscous stress, the kinematic and isotropic hardening stresses, and the yield stress of high strength medium carbon steel. Moreover, since the results are to be used for the simulation of a quenching process, stress components for austenite and martensite phases will be identified and an empirical model proposed for their evolution as a function of temperature will be presented.

5.2 Experimental Procedures

The material investigated has the following chemical composition: Fe–0.43C–0.70Mn–1.65Si–1.80Ni–0.82Cr–0.41Mo–0.07V (wt. %). The tests were carried out using the Gleeble 3800 thermo-mechanical simulator. Due to the resistance heating and the continuous

cooling of the anvils, specimen geometry must be carefully chosen to provide minimal temperature gradient (Kardoulaki et al., 2014; Xiao et al., 2021). In this study, a cylindrical specimen with reduced section was chosen for martensite tests from room temperature (25 °C) to 300 °C, whereas a constant diameter was chosen for austenite for a temperature range of 500 °C to 800 °C. These geometries were selected based on preliminary tests conducted for the assessment and minimization of the thermal gradient to less than 5 °C in a region of 5 mm around the middle of the sample.

For tests on martensitic structures (i.e., ≤300 °C), cylindrical geometry with reduced samples section had a total length of 127 mm with a larger diameter of Ø10 mm on both ends and a reduced cross section of 5 mm in the gauge length, as shown in Figure 5.1(a). The reduced cross section served as a stress concentrator, promoting a fracture in the gauge region, and preventing any deformation and rupture from occurring in the end threads. For the tests in the austenite region, a constant diameter of 6 mm was used, as shown in Figure 5.1(b). Although no reduced section was machined in the gauge region, no deformation or rupture was observed on the threads as austenite is a low strength phase, especially at high temperatures.

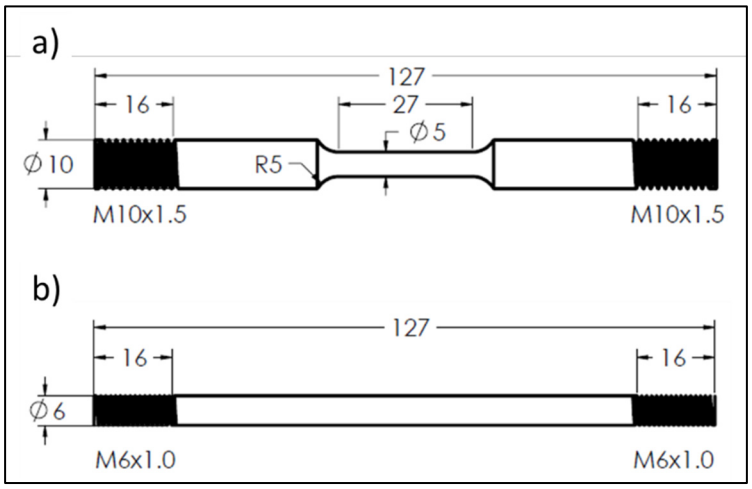

Figure 5.1 a) Geometry of the cylindrical specimen with reduced section; b) Geometry of the constant diameter specimen for test on austenite

The temperatures tested for both phases and their heat treatment cycles are illustrated in Figure 5.2. For the austenite phase, the samples were heated at a rate of 1.5 °Cs^{-1} and soaked for 600 s at 875 °C, under vacuum to prevent oxidation. It was then cooled to the respective testing temperature and held at that temperature for the duration of the test. The temperature was measured using a k-type thermocouple spot-welded at mid-length of the samples. The displacement was measured with an external strain gauge type extensometer. Argon gas was used as the quenching medium when high cooling rates were needed; otherwise, natural cooling was sufficiently fast in most tests. The rationale for the selection of the test temperatures as well as the different type of loadings will be discussed in the next section.

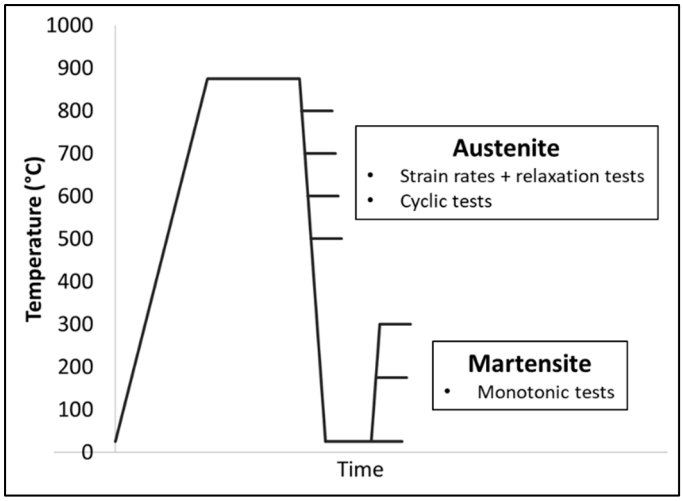

Figure 5.2 Schematic of the tests conducted to determine the thermo-mechanical properties of austenite and martensite with temperatures of 800, 700, 600, and 500 °C for austenite and room temperature, 175 and 300 °C for martensite

5.2.1 Various Strain Rates with Relaxation Tests

The rate-dependent plasticity, often correlated to the viscosity, is more apparent at high temperatures (Krempl & Lu, 1984). It was suggested that for a quenching process, elasto-plastic models would suffice for the prediction of distortions due to the fast-cooling nature of the process (Gür & Şimşir, 2012; Nallathambi et al., 2008). However, for large size components, the cooling rate slows down significantly due to the small temperature difference

between the component and the quenching medium. For this reason, the measurement and determination of the viscous stress is necessary for a softer phase, such as austenite, as it occupies a large range of temperature (Denis, 1997).

Two methods can be used to extract the viscous stress (Lemaitre, Chaboche, Benallal, & Desmorat, 2020). By using different strain rates, the jump in the measured stress from one strain rate to another corresponds to the viscous stress (S.-L. Zhang & Xuan, 2017). However, this first method is very tedious as it requires the usage of the multiple strain rates with different orders of magnitude. Another suitable method to determine the viscous stress is the use of stress relaxation tests (Altenbach, Naumenko, & Gorash, 2008; Roux & Billardon, 2007). From the curve in these tests, a large number of strain rates and their corresponding viscous stresses can be extracted. As for the results of applying multiple strain rates, the obtained stress-strain curves will be particularly useful for comparison and validation with the reconstructed stress-strain curves from all identified stress components.

The conducted tests consisted of 3 strain rates with different durations leading up to a total strain of 7 %. The tests were then followed by a relaxation test of 400 s where the displacement was fixed, and the stress was measured. The duration for each corresponding strain rate is summarised in Table 5.1. The mechanical tests for temperatures lower than 500 °C were not feasible due to phase transformation occurring during these tests.

Table 5.1 Various strain rates, durations, and total strains for the austenite phase

Temperature (°C)	Strain rate (s^{-1})	Duration (s)	Repetition
800	10^{-3}; 10^{-4}; 10^{-5}	20; 120; 300	2 times for all 3 strain rates
700	10^{-3}; 10^{-4}; 10^{-5}	23; 100; 200	2 times for all 3 strain rates
600	10^{-3}; 10^{-4}; 10^{-5}	27; 65; 300	2 times for 10^{-3} s^{-1} and 10^{-4} s^{-1}
500	10^{-3}; 10^{-4}; 10^{-5}	30; 40; 200	2 times for 10^{-3} s^{-1} and 10^{-4} s^{-1}

5.2.2 Cyclic Loadings Tests

Kinematic hardening stress, isotropic hardening stress, and the yield stress are extracted from cyclic tests. A total of 4 cycles with increments of 0.5 % strain leading to a total strain of 2 % was considered for all temperatures, as shown in Table 5.2. The choice of 4 cycles was made from the premise that in a typical quenching process, usually 1 cycle of tensile and compressive stresses is observed, and a maximum of 2 cycles can occur depending on the geometry of the component (Hossain, Stuhr, Robinson, & Truman, 2021; Masoudi, Amirian, Saeedi, & Ahmadi, 2015). The 2 additional cycles would allow for a finer modeling and interpolation of the results. A strain rate value of 10^{-4} s^{-1} was chosen as it was a good compromise between the good control of system (the change from tension to compression) and the time permitted to finish the test before any phase transformation. This permitted time will be discussed further.

Table 5.2 Strain increments and strain rates for the austenite phase

Temperature (°C)	Number of cycles	Strain increment (%)	Strain rate (s^{-1})
800	4	0.5	10^{-4}
700	4	0.5	10^{-4}
600	4	0.5	10^{-4}
500	4	0.5	10^{-4}

5.2.3 Monotonic Loadings Tests

Monotonic tests only provide data for elasto-plastic models. A general assumption is that viscosity is negligible for martensite as it is a super hard phase. Furthermore, the presence of martensite only arises at lower temperatures for a quenching process where viscosity is less pronounced. Three temperatures: room temperature, 175 °C and 300 °C, were selected to characterize martensite, as shown in Table 5.3. A constant strain rate of 10^{-4} s^{-1} was chosen for all three temperatures with a maximum strain of 6 %. The room temperature will be approximated as 25 °C for the rest of the paper.

Table 5.3 Strain rates and total strains for martensite

Temperature (°C)	Strain rate (s^{-1})	Maximum strain (%)
25	10^{-4}	6
175	10^{-4}	6
300	10^{-4}	6

5.2.4 TRIP Effect

As previously mentioned, the implementation of TRIP is crucial for any simulation of heat treatments involving a phase transformation. The main requirement for implementing the TRIP effect in a simulation is the determination of the so-called TRIP parameter or coefficient (Neubert et al., 2016; Simsir, 2017). This can be done by applying different mechanical loads below the yield stress during a phase transformation. Figure 5.3 illustrates the mechanical tests carried out for the determination of this coefficient. Six (6) different applied stresses of -55, -25, 0, 35, 55, and 75 MPa were selected based on preliminary tests, which showed a yield stress well above 120 MPa. The load was applied at 320 °C and removed at 65 °C.

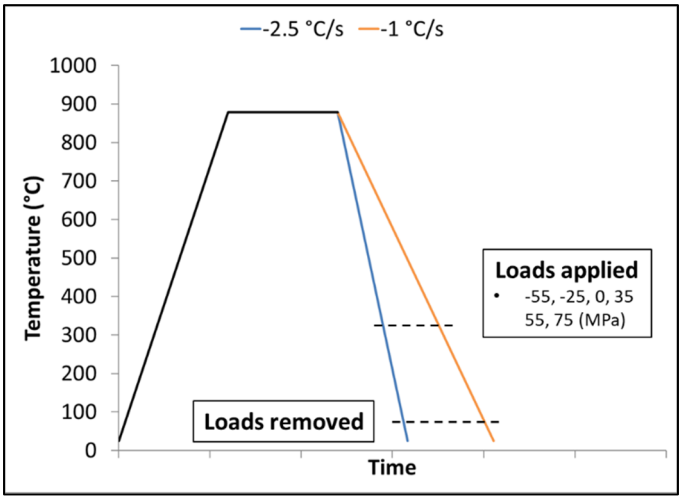

Figure 5.3 Planned metallurgical-mechanical test for the determination of the TRIP parameter

5.3 Results

The results of the previous tests are compiled in the following sections. Using the raw data of Gleeble, a methodology will be provided for the extraction of each stress component. Moreover, based on the obtained results, models are developed to provide stress components in between the tested temperatures. As tests for austenite cannot be completed at low temperatures without the occurrence of phase transformation, stress components are approximated by the values obtained from extrapolations of the proposed models.

The error bars for each measurement extracted from the raw data were calculated based on random errors regarding the measurements performed on each sample's dimensions and systematic errors during data acquisition from the Gleeble equipment. The uncertainty was calculated based on the type-A uncertainty with ±2 standard deviations, for a 95% confidence interval. As for the error bars for models' parameters, they were calculated by populating random values within the error bars of the extracted measurements and plotting the model at each iteration. A choice of 100 iterations was chosen for the dispersion of the models' parameters. The error bars were then calculated once more using ±2 standard deviations.

5.3.1 Austenite: Thermo-Elasto-Viscoplastic Behavior

The results for relaxation tests are shown in Figure 5.4. A duration of 400 s was enough to relax the specimen for the investigated steel composition as observed with the appearance of constant slope. Figure 5.4 shows that viscosity becomes more and more significant at higher temperatures. For instance, at 800 °C, a decrease of around 85 MPa in stress from 110 MPa to 25 MPa at 7 % total strain was observed. The viscous stress corresponds to roughly 77 % of the total stress. At 600 °C, this value is only 34 %, which is significantly lower.

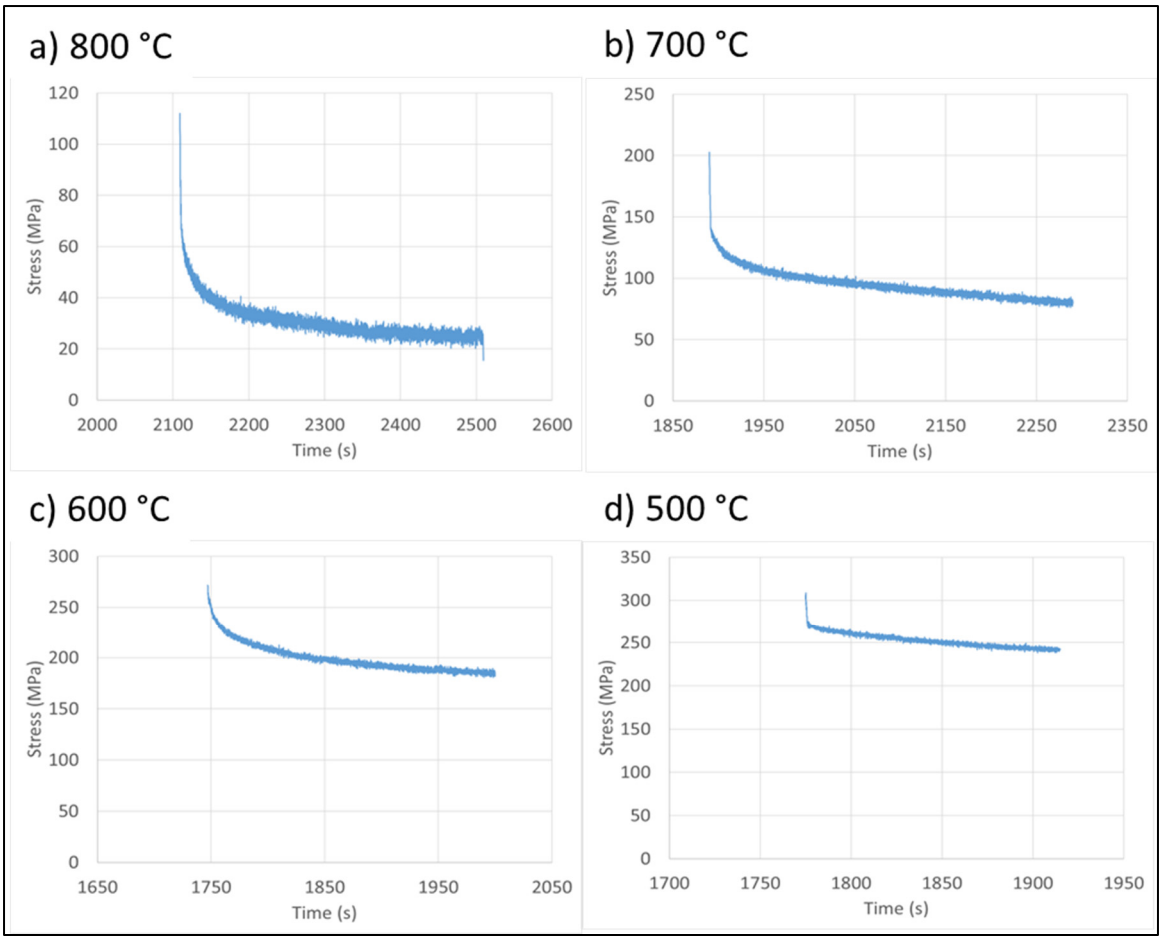

Figure 5.4 The evolution of stress relaxation at different temperatures for viscosity stress determination: a) 800 °C, b) 700 °C, c) 600 °C, and d) 500 °C

The results of the cyclic stress tests are shown in Figure 5.5. Visually, the amplitudes of the cycles at 800 °C are almost the same, whereas cyclic hardenings are observed for the temperatures of 700, 600, and 500 °C. This indicates that the isotropic hardening stress is less prominent at higher temperatures. As for the kinematic hardening stress, no conclusion could be drawn without calculation, as it is much easier to observe the change in amplitude than the translation of the cycles.

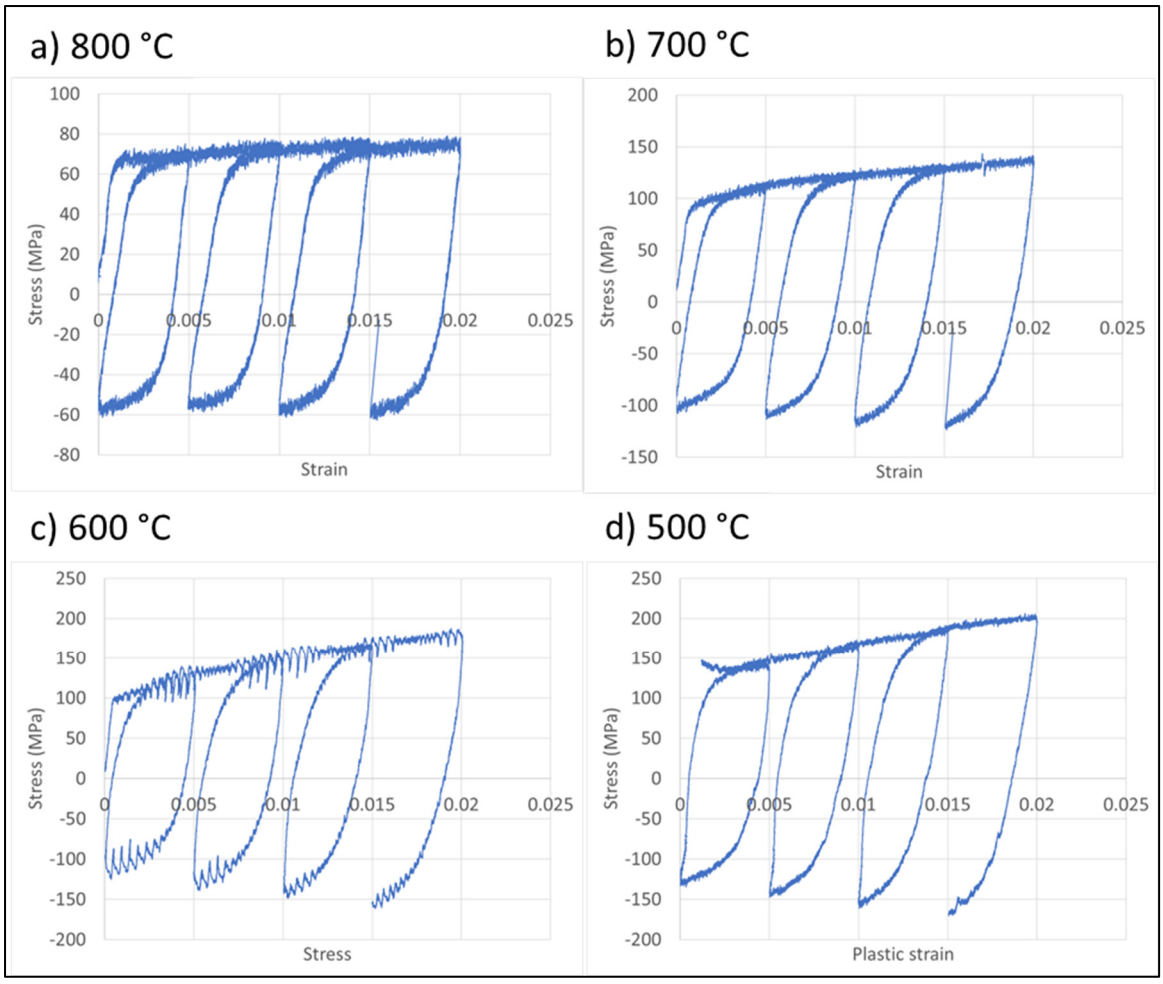

Figure 5.5 Results from cyclic tests for the austenite phase at the temperatures of 800, 700, 600, and 500 °C

5.3.1.1 Determination of the Young's Modulus (E)

The decomposition of the total stress starts with the determination of the Young's modulus. The measurement was done on the viscosity curves using a linear fit on the elastic region. The results of the determined Young's modulus are shown in Figure 5.6. Although it was impossible to complete the viscosity test at 400 °C, the elastic deformation was not affected by the phase transformation, and therefore, the measurement of the Young's modulus was possible.

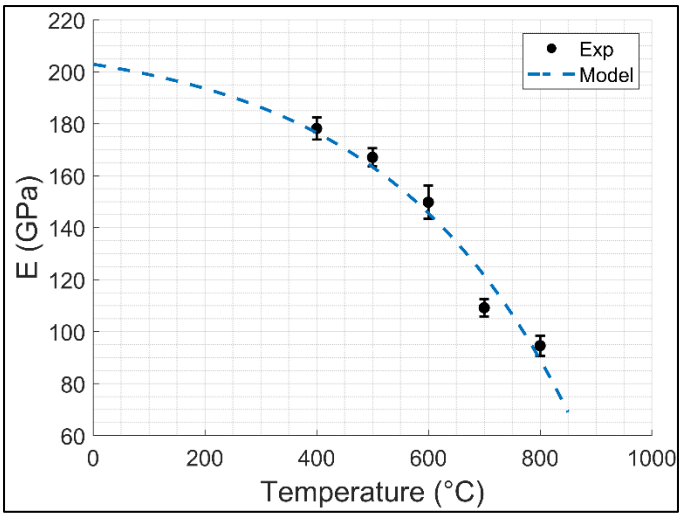

Figure 5.6 Evolution of the Young's modulus measured and modeled as a function of temperature for the austenite phase

For a quenching process, temperatures higher than 900 °C were not required; however, austenite could well be present even at room temperature (retained austenite). For lower temperatures, an extrapolation was necessary as experiments could not be done due to the phase transformation. The exponential function used in the present investigation is as follows:

$$E(T) = 11.36\,(1 - \mathrm{e}^{0.003\,T}) + 202.9 \tag{5.2}$$

with a temperature application range of $0 \leq T \leq 875\ °C$ and an adjusted R^2 of 0.93.

5.3.1.2 Determination of the Viscous Stress (σ_v)

The viscous stress in terms of strain rate could be identified using Eq.(5.3) (Roux & Billardon, 2007). This is based on the assumption that the kinematic hardening stress, isotropic hardening stress, and yield stress remain constant during the relaxation tests, and therefore, they could be subtracted from the total stress. The sum of the above three stresses is referred to as the relaxed stress and is denoted by σ_∞. Furthermore, since the total strain during a relaxation test is zero,

the elastic strain corresponds to the opposite of the visco-plastic strain. Therefore, the strain rate will simply be denoted as $\dot{\varepsilon}$.

$$\dot{\varepsilon} = -\frac{\dot{\sigma}_v}{E} \tag{5.3}$$

$$\sigma_v = \sigma - \sigma_\infty \tag{5.4}$$

The end portions of the relaxation curves were trimmed off as the extracted viscous stress with its corresponding strain rates would be in the vicinity of the strain rate of 10^{-6} s^{-1}. However, the initial portion of the relaxation curve allows a large number of viscous stresses and strain rates to be calculated. Figure 5.7(a) indicates the points used for the relaxation test at 800 °C. Only this temperature is shown as an example for the sake of brevity. For each selected point, the slope of the curve corresponds to the rate of the viscous stress. This slope was calculated using a linear approximation with 50 data points before and after the selected point. The strain rate is then calculated using Eq.(5.3) and the measured Young's modulus previously described. Figure 5.7(b) shows the viscous stress with the corresponding strain rates for all the selected points.

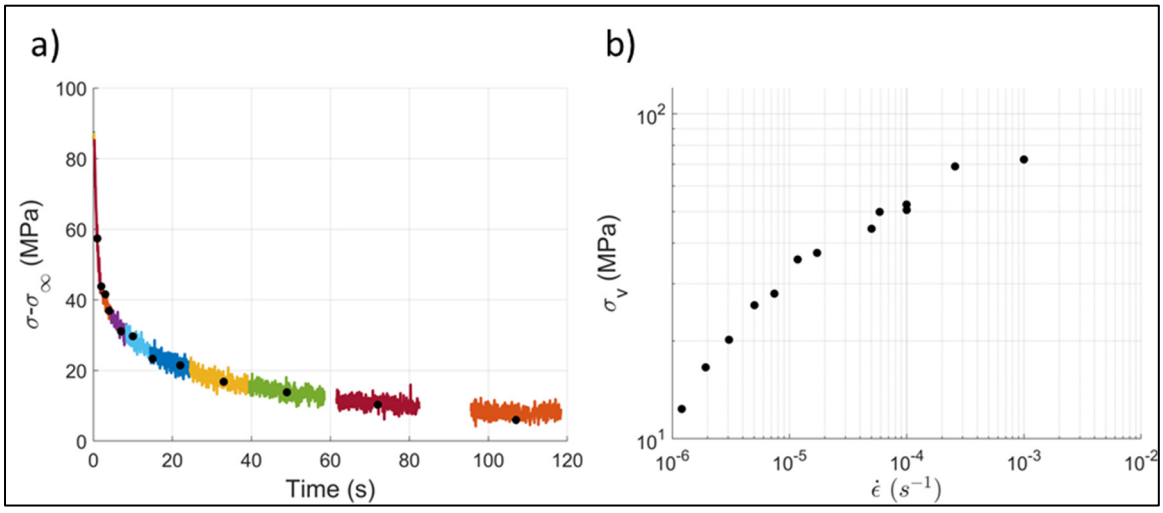

Figure 5.7 Methodology used to obtain the viscous stress from relaxation curves: a) The relaxation curve offsetted by the relaxed stress, σ_∞; b) The measured viscous stress in terms of the calculated strain rates

From the viscous stress, the depiction of the strain rate is accomplished via a linear approach over a precise range of strain rates (Norton, 1929) or a hyperbolic sine expression (W. Chen & Feng, 2015; Miller, 1976; Roux & Billardon, 2007). The results of viscous stresses for all four (4) temperatures including both expressions are shown in Figure 5.8. The choice for either equation comes down to the applicability of the equation and the computational cost. If the expected strain rates are over a small range, the Norton's equation will suffice and will be ideal as a linear formulation is easier for calculations. If the strain rate range is large, the Norton's equation will then over predict or under predict the viscous stress. The values of the parameters for both the hyperbolic sine expression and the linear Norton formula are tabulated in Table 5.4. The Norton's equation was fitted with the results for the strain rates between 10^{-5} s^{-1} and 10^{-3} s^{-1} using only the scattered red points. In Eqs.(5.5) and (5.6), A is the viscosity strain rate, and B, L, M, and N are rate-independent material parameters.

$$\sigma_v = B \sinh^{-1}\left(\left[\frac{\dot{\varepsilon}}{A}\right]^{\frac{1}{N}}\right) \tag{5.5}$$

$$\sigma_v = L\, \dot{\varepsilon}^{\frac{1}{M}} \tag{5.6}$$

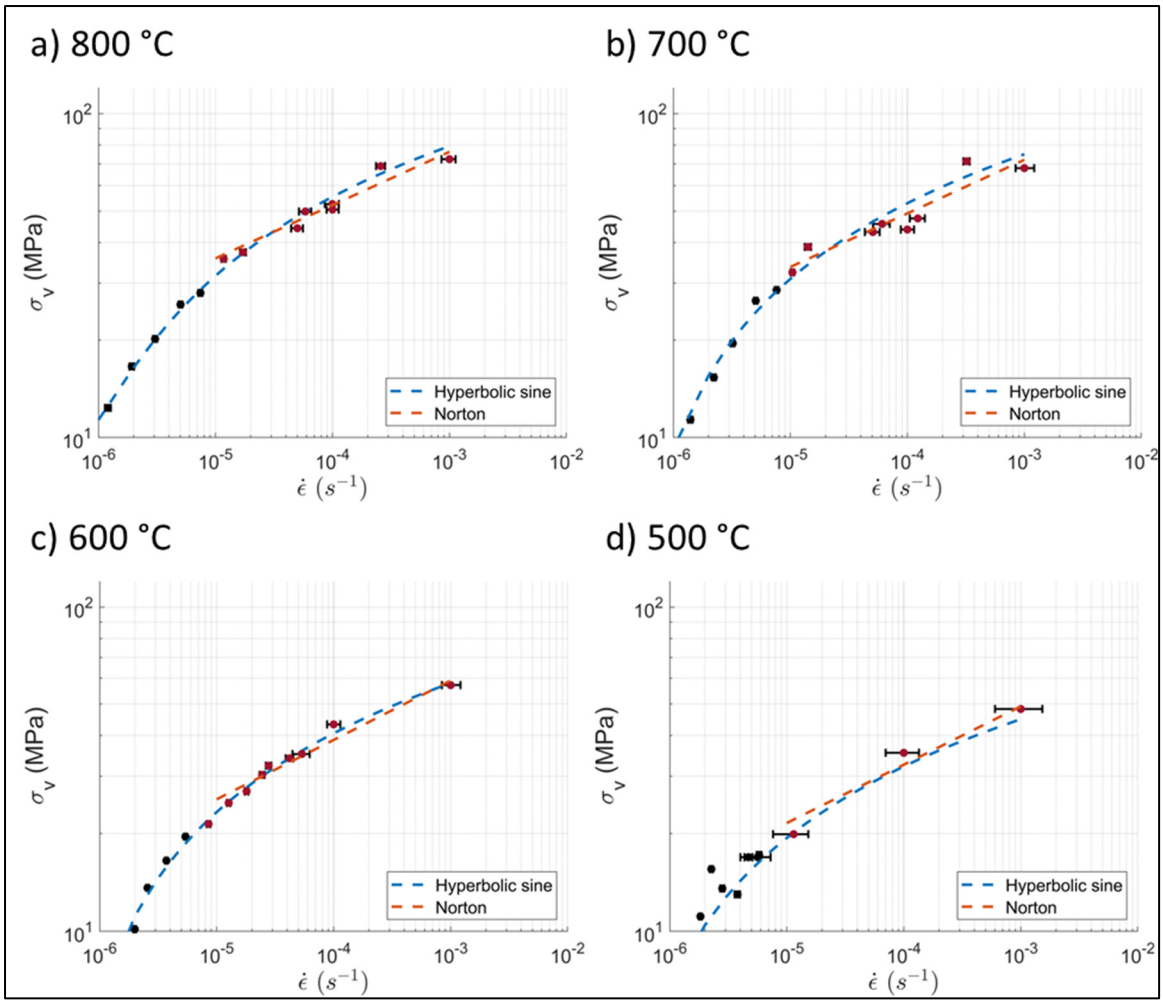

Figure 5.8 Viscous stress modeled using a hyperbolic sine expression and the linear Norton equation

Table 5.4 Extracted parameters for the modeling of the viscous stress using a hyperbolic sine expression and the linear Norton equation

Temperature (°C)	B (MPa)	N	A (s^{-1})	L (MPa $s^{1/M}$)	M
800	15.46	1.482	1.39E-6	237.4	6.082
700	6.436	0.673	6.34E-7	225.7	5.961
600	2.813	0.363	6.06E-7	192.5	5.851
500	1.668	0.301	3.72E-7	169.3	5.603

The parameters of the hyperbolic sign equation were determined using the tests at the interval between 500 and 800 °C. Similar to the determination of the Young's modulus, extrapolations are required for lower temperatures. The variation of the parameters for the hyperbolic sine expression is shown in Figure 5.9. Additional caution was undertaken to ensure that the extrapolated curve would not generate implausible values such as negative values when linear equations are used. For this reason, B, N, and A are presented with exponential regressions. Therefore, the temperature application range for Eqs.(5.7)-(5.9) is $0 \leq T \leq 875\ °C$ and with adjusted R^2 of 0.97, 0.97 and 0.94, respectively.

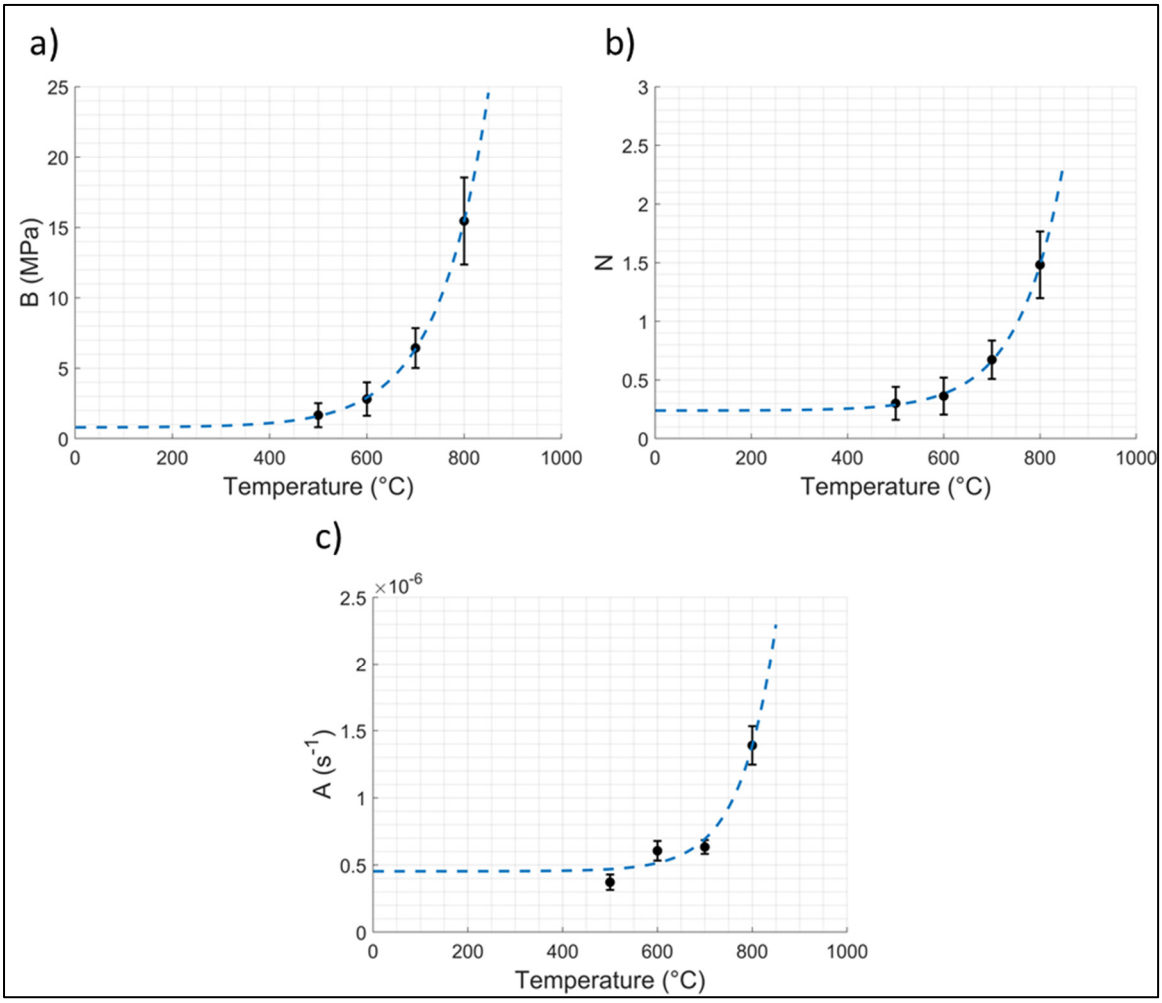

Figure 5.9 Determination of the parameters for the viscous stress

$$B(T) = 0.0064\ \mathrm{e}^{0.0097\,T} + 0.798 \tag{5.7}$$

$$N(T) = 2.25\text{E-}4\ \mathrm{e}^{0.0108\,T} + 0.240 \tag{5.8}$$

$$A(T) = 1.77\text{E-}11\ \mathrm{e}^{0.0136\,T} + 4.54\text{E-}7 \tag{5.9}$$

As for the Norton's equation, the variations of the parameters L and M as a function of temperature is shown in Figure 5.10 and expressed by Eqs.(5.10) and (5.11). Here, negative parameters were not a problem when using linear equations for the temperature range used. The same range of application is used such as $0 \leq T \leq 875\ °C$. The adjusted R^2 is 0.95 for Eq.(5.10) and 0.93 for Eq.(5.11).

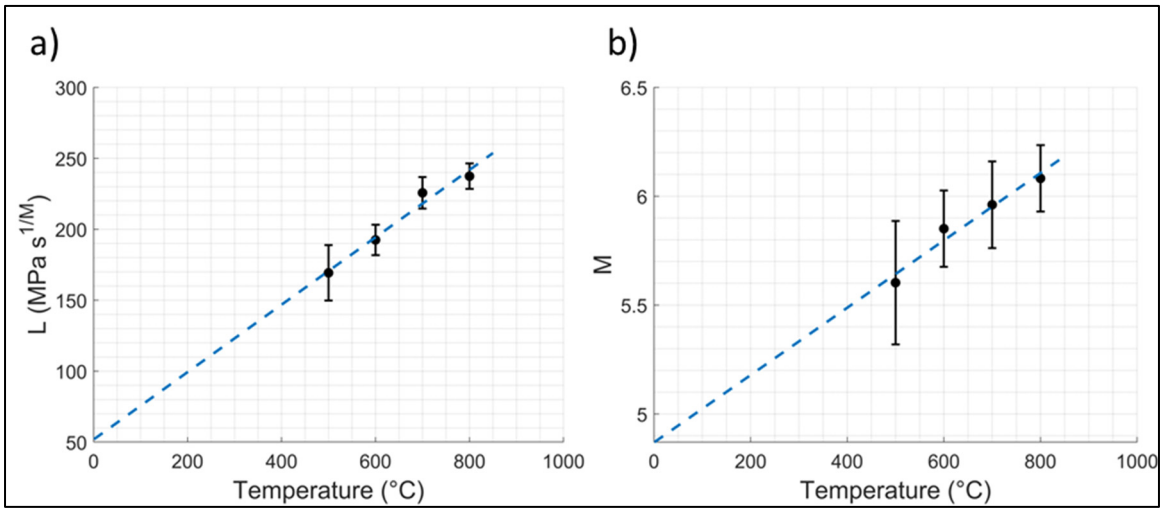

Figure 5.10 Modeling of the extracted parameters for the Norton equation using all four temperatures, a) L and b) M

$$L(T) = 0.238\,T + 51.85 \tag{5.10}$$

$$M(T) = 0.00155\,T + 4.87 \tag{5.11}$$

5.3.1.3 Determination of the Kinematic Hardening Stress (X)

The kinematic hardening stress can be obtained from the set of cyclic tests. For further decomposition of the stress spectrum, the elastic strain must be removed from the total strain and the viscous stress must be removed from the total measured stress of the cyclic tests, in tension and in compression. The resultant stress is a total stress, which is the sum of the kinematic hardening, isotropic hardening, and yield stresses. This subtraction is possible as the Young's modulus and the viscous stress were previously determined. The viscous stress removed at each temperature was calculated based on the hyperbolic sine expression, Eq.(5.5) with the strain rate of 10^{-4} s^{-1}, which was used when conducting the cyclic tests. Figure 5.11 shows how the total stress was obtained in terms of the plastic strain for the second cycle at 800 °C. The orange curve represents the change to the plastic strain. The blue curve is obtained after the removal of the viscous stress in tension and compression from the orange curve. This is with the assumption that viscous stress in tension and compression is similar. The blue point represents the identified kinematic hardening stress, denoted as X, for this cycle. It is located at the mid-distance between the tensile and the compressive yield stresses.

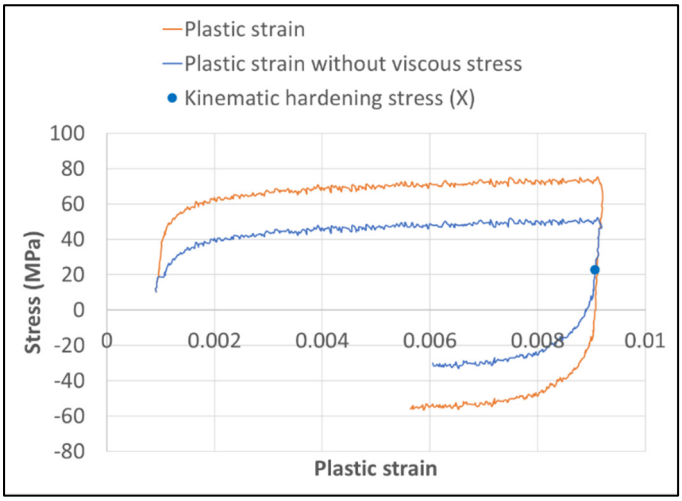

Figure 5.11 Illustration of the calculation on the second cycle at 800 °C for the extraction of the kinematic hardening stress

Figure 5.12 shows the identified kinematic hardening stress as a function of the total accumulated plastic strain, denoted as p. An additional point was added at the origin for proper modeling, indicating that there will be no kinematic hardening stress if no plastic deformation occurs. This evolution of the kinematic hardening stress can be modeled using Armstrong and Frederick plasticity type model, as expressed in Eq.(5.12) (Ashraf, Prasad Reddy, Sandhya, Laha, & Harmain, 2018; Saleh Asheghabadi & Cheng, 2020). The extracted values of the parameters for each temperature are tabulated in Table 5.5.

$$X(p) = \frac{C}{\gamma}[1 - \mathrm{e}^{-\gamma p}] \tag{5.12}$$

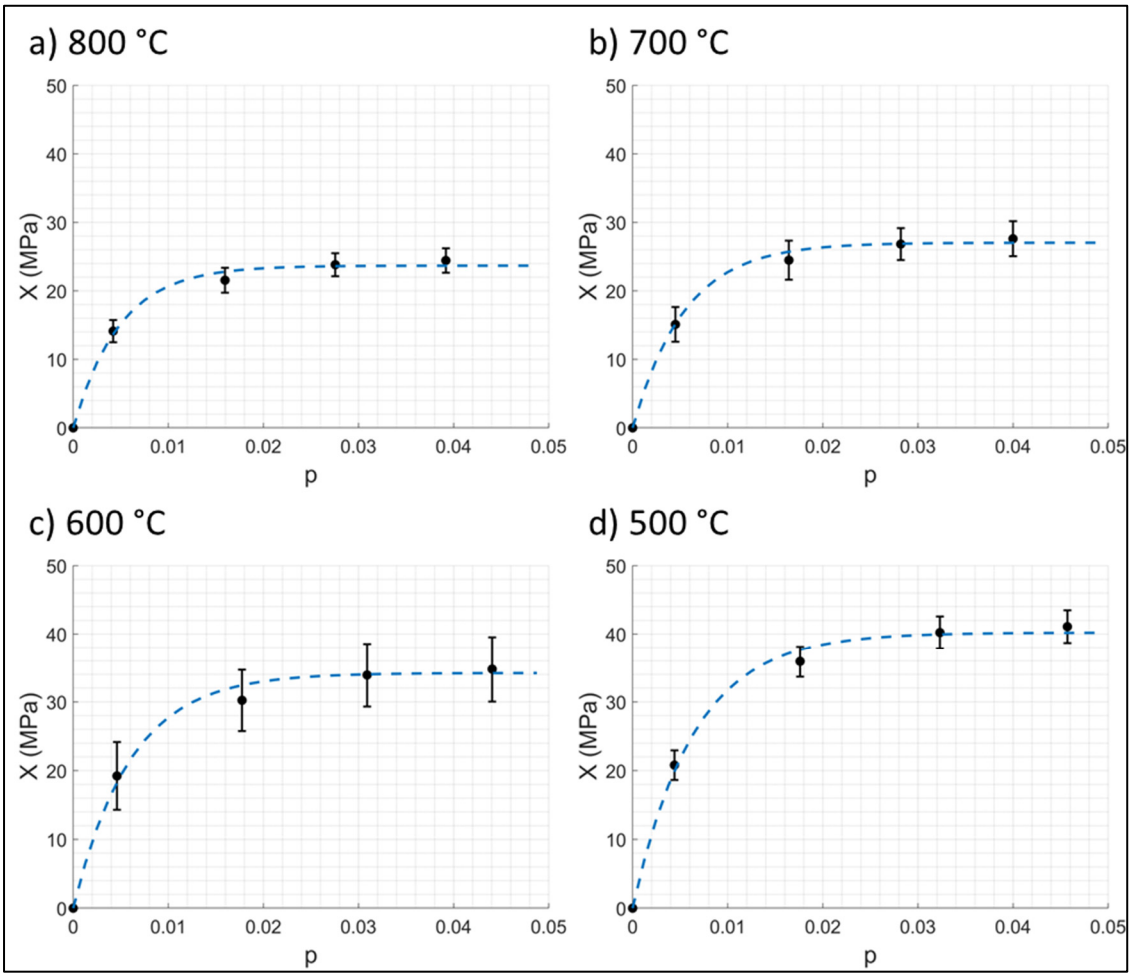

Figure 5.12 Kinematic hardening stress modeled as a function of the total plastic strain of all four cycles for all four temperatures

Table 5.5 Extracted parameters for modeling of the kinematic hardening stress

Temperature (°C)	C (MPa)	γ
800	4785	206
700	4974	184
600	5689	166
500	6269	156

Simple linear models are proposed to model C and γ, as shown in Eqs.(5.13) and (5.14) and plotted in Figure 5.13. C represents the initial kinematic hardening modulus, whereas γ represents the rate of decrease of this modulus. The ratio C/γ represents then the maximum translation of the yield surface. The extrapolated values from linear models did not indicate any improbable values, which would require setting up proper boundary conditions, thus the same temperature application range could be used $0 \leq T \leq 875\ °C$ for both equations. Their corresponding adjusted R^2 are 0.94 and 0.95.

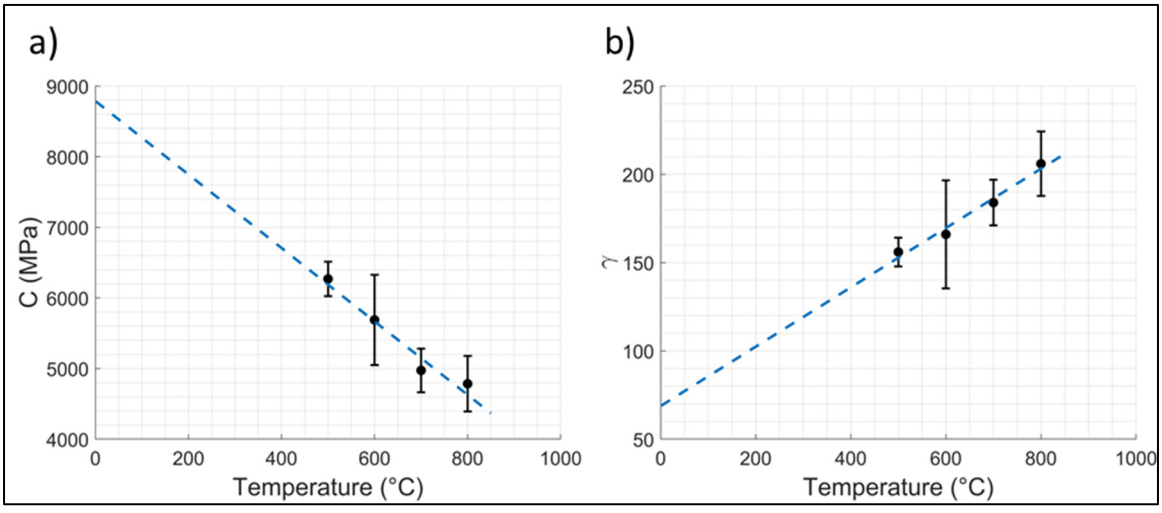

Figure 5.13 Modeling of the extracted parameters (C and γ) for the determination of the kinematic hardening stress

$$C(T) = -5.2\,T + 8788 \tag{5.13}$$

$$\gamma(T) = 0.17\,T + 69 \tag{5.14}$$

5.3.1.4 Determination of the Isotropic Hardening Stress (R)

With the kinematic hardening stress properly identified, another stress component can be removed from the cyclic tests. By doing this, the total stress as the sum of the isotropic hardening stress (R) and the mathematical yield stress (σ_y) is left. The second cycle at 800 °C is again used as an example, as displayed in Figure 5.14. The results of ($R + \sigma_y$) are plotted against the plastic strain in Figure 5.15. A linear regression, as given in Eq.(5.15), seemed sufficient to capture the evolution of the isotropic hardening stress and the mathematical yield stress. The extracted values of D and F are listed in Table 5.6. The parameter D represents the rate of change of the isotropic hardening stress and F will be discussed in the next section.

$$\sigma_y + R = D\,\varepsilon_p + F \tag{5.15}$$

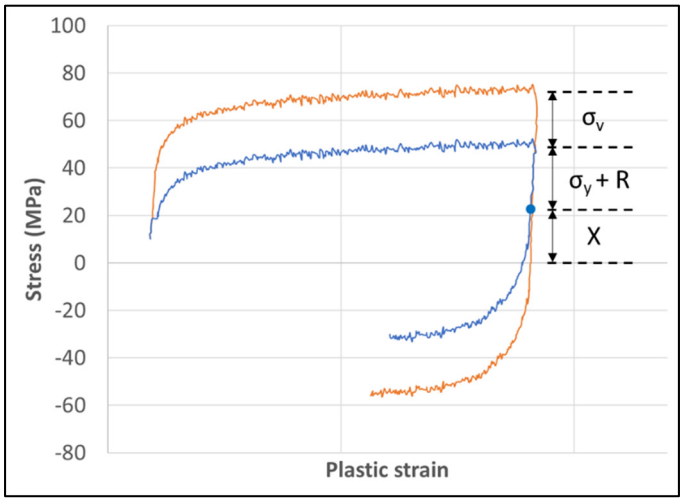

Figure 5.14 Example of the decomposition of the cyclic tests for the determination of the isotropic hardening stress (R) and the mathematical yield stress (σ_y) from the cyclic tests

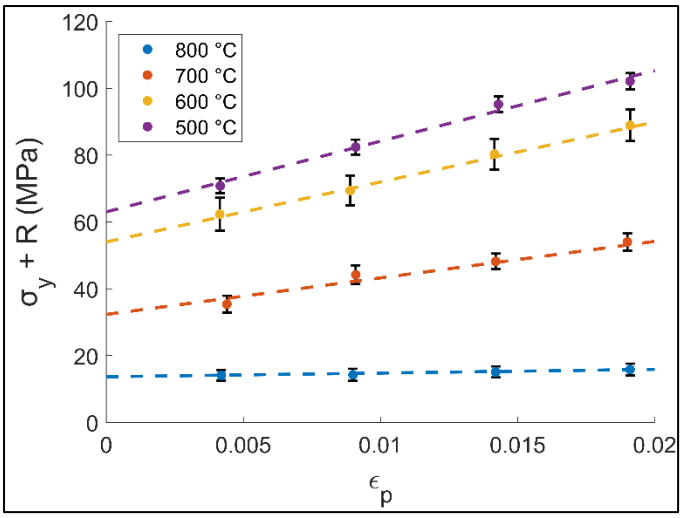

Figure 5.15 Isotropic hardening stress and mathematical yield stress modeled linearly as a function of the plastic strain for all four investigated temperatures

Table 5.6 Extracted parameters for modeling of the isotropic hardening stress and the mathematical yield stress

Temperature (°C)	D (MPa)	F (MPa)
800	110	13.7
700	1093	32.3
600	1795	54.2
500	2116	63.4

Figure 5.16 shows the extracted values of D. An exponential regression provided in Eq.(5.16) was used, which generates negative values at $T > 805\ °C$, therefore the range of application is $0 \leq T \leq 805\ °C$. For instances where the temperature is higher than 805 °C, a boundary condition should be imposed where the isotropic hardening stress would be equal to zero for higher temperatures. The adjusted R^2 for the corresponding equation is of 0.98.

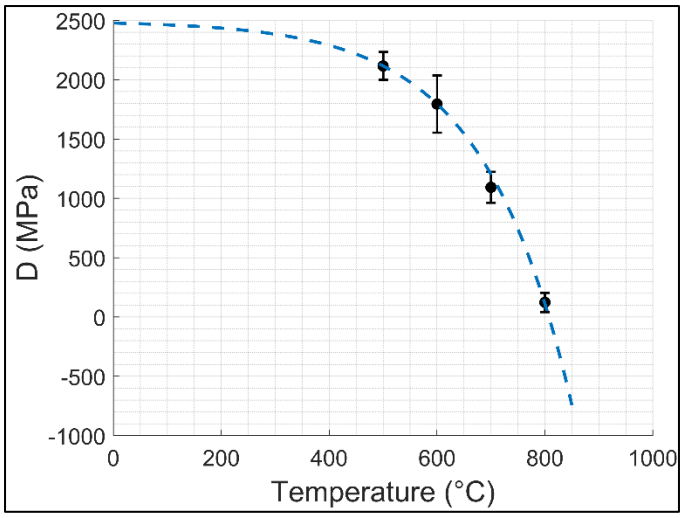

Figure 5.16 Modeling of the extracted parameter D for the determination of the isotropic hardening stress

$$D(T) = 17.75\,(1 - \mathrm{e}^{0.00613\,T}) + 2478 \tag{5.16}$$

5.3.1.5 Determination of the Mathematical Yield Stress (σ_y)

Essentially, the mathematical yield stress is identified at the same time with the isotropic hardening stress through Eq.(5.15). It corresponds to the y-intercept in Figure 5.15, where the regression function crosses the y axis (σ_y axis), or in other words, the mathematical yield stress is denoted as F. The mathematical yield stress term used throughout this paper does not correspond to the conventional yield stress. It is in fact the initial isotropic hardening stress before plastic flow. However, using an initial hardening term without any plastic deformation did not seem appropriate, and therefore, the term mathematical yield stress was used instead. The extracted values are shown in Table 5.6. An exponential equation was used for the extrapolation to lower temperatures. However, once more, boundary conditions must be set for temperatures higher than 850 °C to avoid negative values ($0 \leq T \leq 850\ °C$). The choice of an exponential equation was based on observations of the overall variations of yield stress as a function of temperature for steel from different references (Dong, Song, & Zhang, 2014; Telejko, Adrian, & Guzik, 2013; W.-y. Wang, Liu, & Kodur, 2013). The adjusted R^2 is of 0.96.

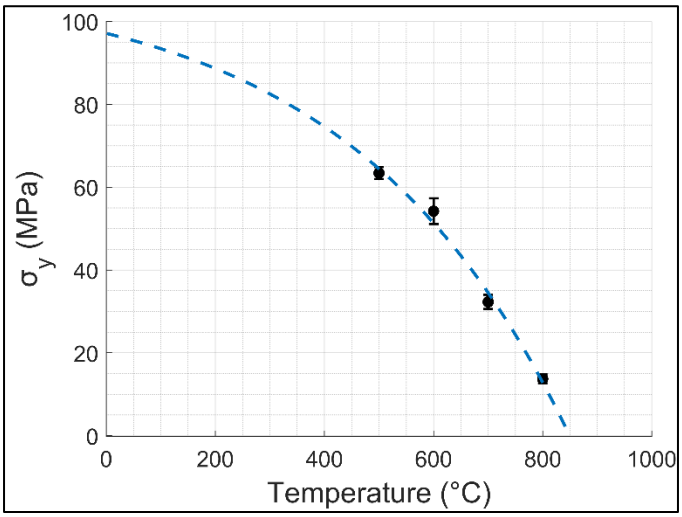

Figure 5.17 Modeling of the mathematical yield stress as a function of the temperature

$$\sigma_y(T) = 12.95\ (1 - \mathrm{e}^{0.00252\,T}) + 97.13 \tag{5.17}$$

5.3.1.6 Comparison Between Experimental and Modeled Stress Components

Figure 5.18 shows the results from experimentally applying various strain rates compared with the modeled stress-strain curve reconstructed with the previously identified stress components. The hyperbolic sine function was chosen to identify the viscous stress. The reconstruction also uses the values from the provided equations rather than the values extracted for that temperature. For instance, the Young's modulus measured at 700 °C is 109.2 GPa while the calculated Young's modulus from Eq.(5.2) is 121.6 °C. The strain rates are shown in Figure 5.18(a) as a reference.

At 600 °C, as displayed in Figure 5.18(c), the measurements become noisy. This is due to the PID control which needs to be adjusted for each temperature. Unfortunately, due to the limited number of samples, adjusting this PID by trial and error could not be done intensively.

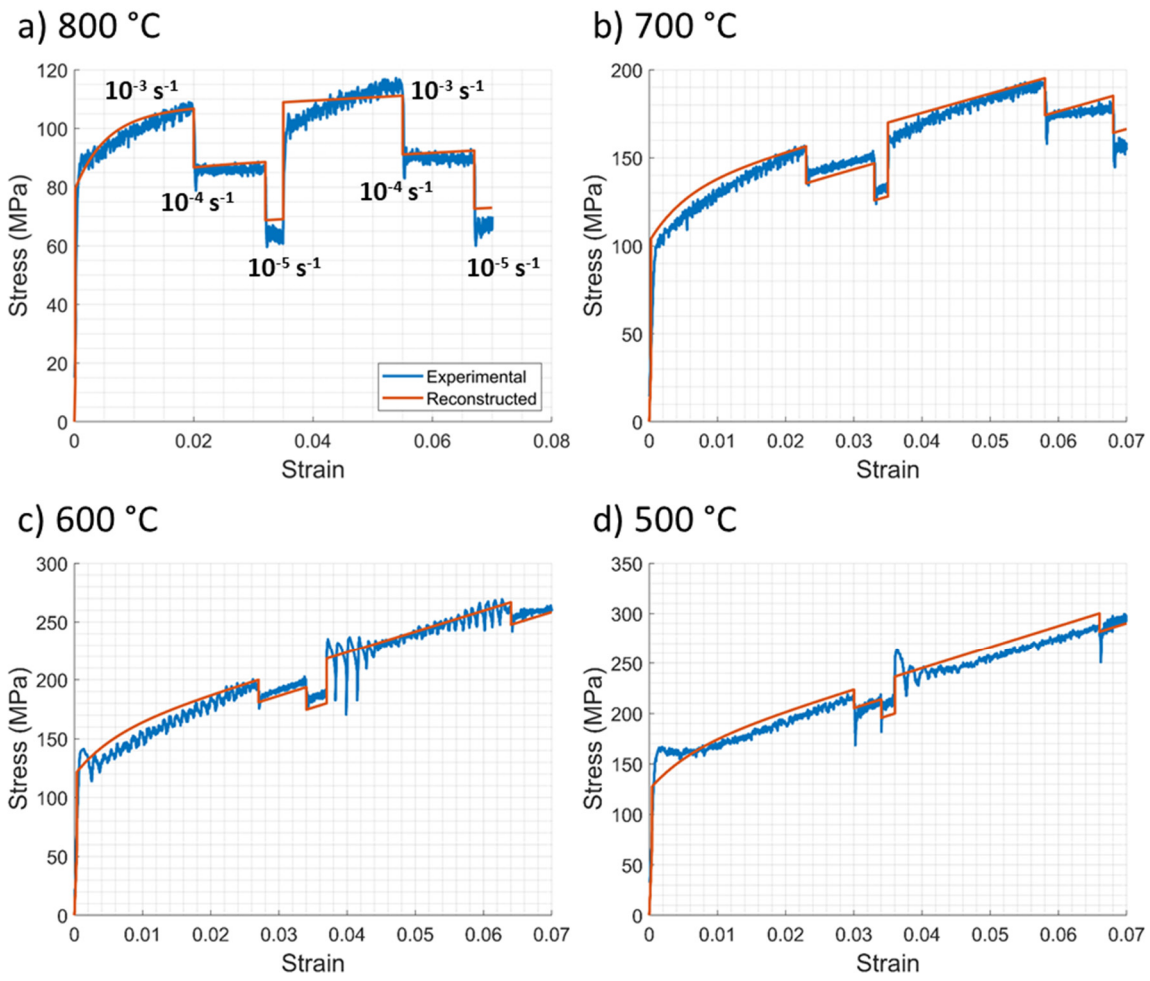

Figure 5.18 Stress results from the various strain rates applied experimentally for the austenite phase compared with the reconstructed stress-strain curves from the extracted stress components

As seen in Figure 5.18, the reconstructed stress-strain curves are in very good agreement with the experimental results. There are only some slight differences such as a higher overall predicted stress for 500 °C and slightly higher values of viscous stress for 700 °C and 600 °C. It is important to note that no optimisation process has been conducted in order to identify the closest possible values for each equation provided. As the focus of the study is to provide a methodology for the extraction of the stress components from experimental results, an optimization would therefore defeat the purpose of the present objective.

5.3.2 Martensite: Elasto-Plastic Behavior

The stress-strain curves for monotonic loadings at lower temperatures with the martensite phase is presented in Figure 5.19. The results show a decrease in the plastic stress with an increase in the temperature. From these results, an elasto-plastic model was developed with the extraction of the Young's modulus, the isotropic hardening stress, and the mathematical yield stress.

The Young's modulus (E_m) for martensite extracted from the monotonic curves using the same approach as austenite is shown in Figure 5.20 and modeled linearly with Eq.(5.18). No extrapolation to higher temperatures is needed for martensite during a quenching process. Therefore, the temperature application range is $0 \leq T \leq 300\ °C$ and with the adjusted R^2 of 0.97.

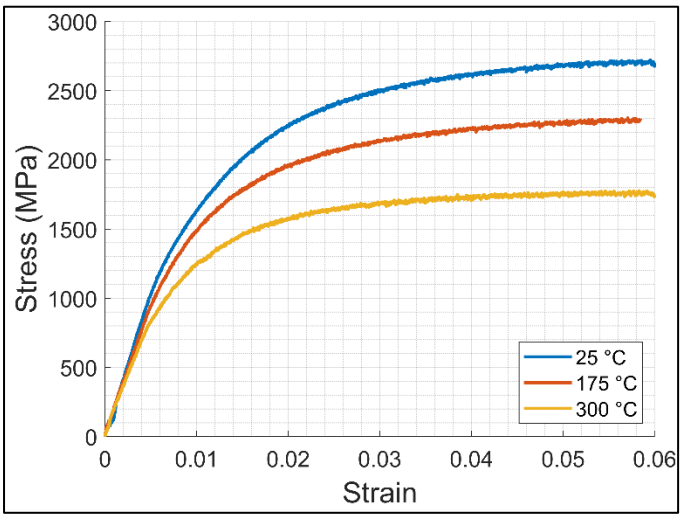

Figure 5.19 Stress results from the monotonic tests for martensite at the temperatures of 25 °C, 175 °C, and 300 °C

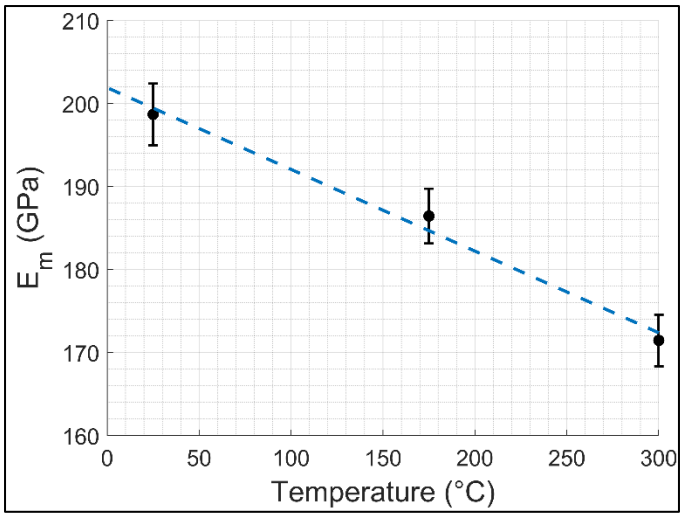

Figure 5.20 Modeling of the Young's modulus (GPa) as a function of the temperature for martensite

$$E_m = -0.09841\,T + 201.9 \tag{5.18}$$

Following the identification of the Young's modulus, the strain was converted to the plastic strain. Figure 5.21 shows the total stress as a function of the plastic strain. The isotropic hardening stress and the mathematical yield stress were again determined by using the general formulation of Eq.(5.19). The blue, red, and orange dashed linear curves for the temperatures of 25 °C, 175 °C, and 300 °C, between the interval of 0.02 and 0.045 strain, represent the linear fitted equations of Eqs.(5.20).

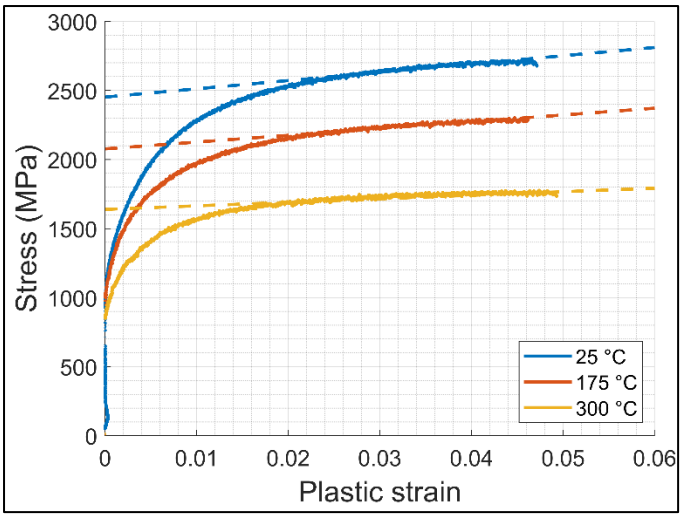

Figure 5.21 Isotropic hardening and mathematical yield stress (MPa) identification for martensite

$$\sigma_{y,m} + R_m = D_m \ \varepsilon_p + F_m \tag{5.19}$$

$$\sigma_{m,25°C} = 5987 \ \varepsilon_p + 2452 \tag{5.20}$$

$$\sigma_{m,175°C} = 4907 \ \varepsilon_p + 2077 \tag{5.21}$$

$$\sigma_{m,300°C} = 2553 \ \varepsilon_p + 1639 \tag{5.22}$$

The extracted values for the parameters D_m and $\sigma_{y,m}$ or F_m, for all the three temperatures, are plotted in Figure 5.12. A linear regression model was used for interpolation and shown by Eqs.(5.23) and (5.24). Similar to austenite, D_m represents the rate of change of the isotropic hardening stress for martensite and $\sigma_{y,m}$ and F_m are the mathematical yield stress of martensite. Once more as it is a quenching process, the temperature application range is of $0 \leq T \leq 300\ °C$ with adjusted R^2 of 0.87 and 0.98 for Eqs. (5.23) and (5.24), respectively.

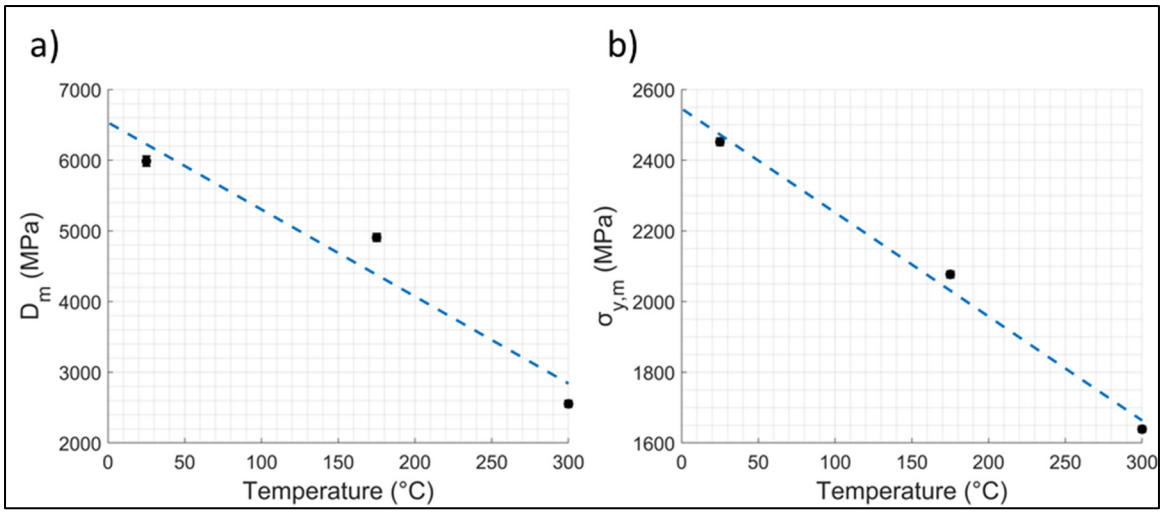

Figure 5.22 Modeling of the parameter D_m and the mathematical yield stress $\sigma_{y,m}$ of martensite

$$D_m(T) = -12.31\,T + 6534 \tag{5.23}$$

$$\sigma_{y,m}(T) = -2.941\,T + 2546 \tag{5.24}$$

5.3.3 TRIP Strain

The TRIP strain is observed as an increase in the final strain during the phase transformation due to external loads which lie below the yield stress (Fischer & Schlögl, 1995; Simsir, 2017). Figure 5.23 shows the strain, calculated with the dilatation measurements from the external extensometer, as a function of the temperature, cooling rates, and mechanical loads. The 0 MPa was used as a reference for the determination of the increase in strain with mechanical loads. This TRIP strain is denoted as ε^{tr} and was calculated based on the strain at the temperature above 75 °C, before the unloading of the mechanical loads, σ_{ext}. The TRIP strains are reported in Table 5.7.

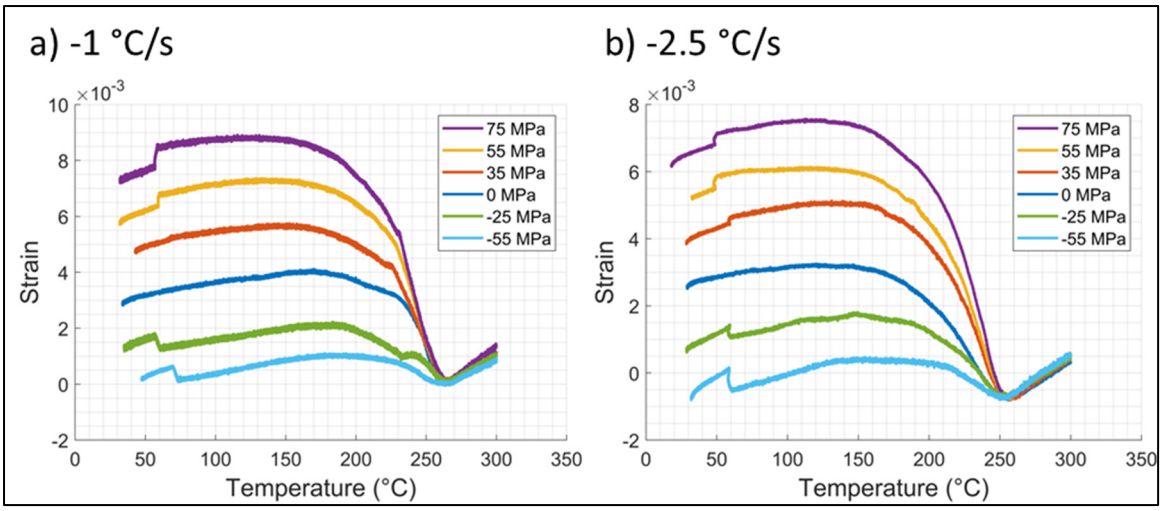

Figure 5.23 Dilatometry results from TRIP tests for cooling rates of -1 and -2.5 °C/s

Following Eq.(5.25), the TRIP parameter K can now be identified. The term $\phi(z)$ represents the progress of transformation plasticity with z being the fraction of phase transformed. In this case, $\phi(z) = 1$ as the transformation is completed. The TRIP strain as a function of the applied mechanical loadings is plotted in Figure 5.24. The application range needs to have mechanical loads inferior to the yield stress of the material in tensile and compression. In this case, the lowest estimated σ_y is around 100 MPa at 500 °C. As a precaution, the proposed application range is of $-75 \leq \sigma_{ext} \leq 75\ MPa$. The adjusted R^2 for both cooling rates is 0.99.

$$\varepsilon^{tr} = K\sigma_{ext}\phi(z) \tag{5.25}$$

Table 5.7 Measured TRIP strains for the cooling rates of -1 °Cs^{-1} and -2.5 °Cs^{-1} and the mechanical loads of -55, -25, 0, 35, 55, and 75 MPa

σ_{ext} (MPa)	ε_{-1}^{tr}	$\varepsilon_{-2.5}^{tr}$
75	0.0052	0.0043
55	0.0034	0.0030
35	0.0018	0.0017
0	0	0
-25	-0.0020	-0.0019
-55	-0.0033	-0.0034

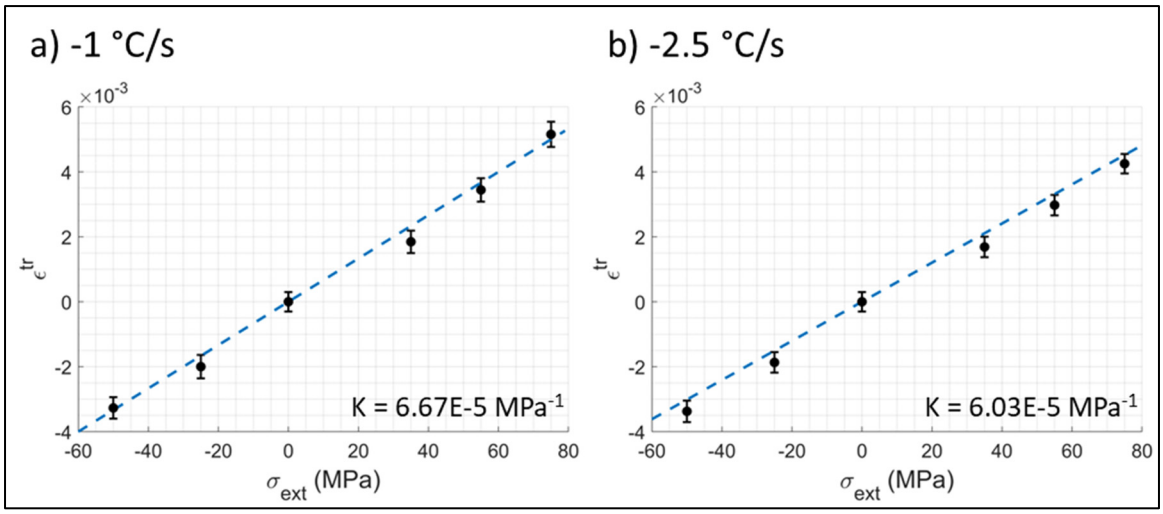

Figure 5.24 Identification of the TRIP parameter K for the cooling rates of -1 and -2.5 °C/s using a linear fit where the measured slope of the fitted equation corresponds to K

5.4 Summary and Conclusion

A major drawback of distortion predictions by simulations is the lack of material data as well as appropriate constitutive models for a wide range of temperatures. This highly material-sensitive process suffers in accuracy when the material data are approximated with data from different steel compositions or extracted from 'blackbox' material simulation software.

The present Young's modulus for austenite was modeled using an exponential equation. This was deemed more representative of its evolution, especially when extrapolated to lower temperatures. A linear approach would have caused an over prediction at room temperature (Ledbetter, Weston, & Naimon, 1975; Mustak et al., 2016). For a quenching process, an elasto-plastic model is often preferred for its simplicity. The rate independent model is convenient as the process usually does not last very long. However, for industrial applications involving large components, this would be an oversimplification. For this matter, viscous stress and strain rates were extracted from the relaxation curves. Two models were proposed: a hyperbolic sine function and the linear Norton equation (Ahmed, Barrett, & Hassan, 2016; Barrett & Hassan, 2020; Szmytka, Rémy, Maitournam, Köster, & Bourgeois, 2010). Both equations are acceptable depending on the expected strain rates during simulations. If strain rates throughout the simulation are all in close proximity, the linear model will significantly reduce the computational time with minimum compromise on the distortion prediction. The stress reversal between tension and compression due to thermal expansion and phase transformation during a quenching process is characterized by the kinematic hardening stress. It was shown that the inclusion of a kinematic hardening model provided predicted residual stresses closer to the experimental measurements (Kawaragi, Fukumoto, & Okamura, 2015).

The extrapolation and interpolation of mechanical properties at different temperatures is also an important point that was rarely discussed in literature. This is especially true for mechanical properties of phases exposed to a wide range of temperatures during the heat treatment process. Generally, the issue of utilizing mechanical properties at higher and lower temperatures without proper characterization are neither explained nor discussed. In this study, the authors provided a set of equations for the evolution of parameters in the temperature range of a quenching process. The reconstructed stress-strain curves from the identified stress components were compared with the experimental results and showed excellent agreement.

As for martensite, generally in a quenching process, the stress levels are not expected to surpass the yield stress. Therefore, elasto-plastic with an isotropic hardening models are often the main implementation choice for researchers (Gür & Tekkaya, 1998; Kang & Im, 2007). Three

temperatures were chosen for the determination of the thermo-mechanical properties as martensite only exists at temperatures lower than the Ms (estimated at 295 °C for the current steel) for a quenching process. This grants the possibility of modeling the properties linearly as most properties decrease rapidly for temperatures above 450-500 °C (Dong et al., 2014; W.-y. Wang et al., 2013).

The TRIP effect was dependent obviously on the loadings in compression and in tension. The determined TRIP strains of 6.67×10^{-5} and 6.03×10^{-5} for the cooling rates of -1 and -2.27 °C/s were consistent in terms of magnitude (Franz et al., 2005; Neubert et al., 2016; Simsir, 2017). Previous studies often focused on the determination of the TRIP parameter for different steel compositions, but it is shown here that for the same steel (identical compositions), the cooling rate also affects TRIP. The increase in TRIP strain for a slower cooling rate could be related to a higher amount of retained austenite, which is more ductile than martensite. Therefore, for similar loadings, a higher deformation would be observed for the material with higher austenite content.

In this paper, a complete methodology was presented for the determination of the thermo-mechanical properties needed for a quenching process. The data were extracted and compiled by means of experimental tests and modeling. The provided models serve to build a thermo-elasto-viscoplastic model with kinematic and isotropic hardening components for austenite, whereas a thermo-elasto-plastic model with only isotropic hardening for martensite. The TRIP strain was also measured for various mechanical loadings to determine the TRIP parameter, K. It was shown for the first time that the TRIP parameter changes with the cooling rate.

GENERAL CONCLUSION

Accurate predictions for quenched induced distortions are sought by the industry for its high potential gains, such as the elimination the time required to rework a rejected part and the reduction of the extra material machined off which was added to compensate the distortions. One of the most widespread methods of predicting these distortions during a quenching process is by simulation. This can be achieved by building models revolving around 3 main physical fields, the thermal, the metallurgical and the mechanical field. The accuracy of the prediction is directly related to the accuracy of the models implemented. The present project focuses on the characterization and modeling of two of the three major physical fields, the metallurgical and mechanical field for a low alloy medium-carbon steel.

The martensitic phase transformation has been reviewed for a quenching process involving a massive component. It was shown that a slow cooling occurred during the ongoing phase transformation, between the Ms and the Mf. This slow cooling rate led to the development of a deceleration of the phase transformation. The effect of the cooling rates under the Ms on the kinetics of martensite transformation was characterized by dilatometry which showed the presence two-stage transformation. The main phenomenon identified for the explanation of this deceleration was the carbon partitioning from the fresh martensite to the massive austenite due to auto-tempering.

With a two-stage transformation, conventional methods of modeling the kinetics of martensite transformation through the usage of the K-M equation, proved to be inaccurate. Therefore, an advanced and more robust model has been proposed in the form of a routine. It uses several equations describing the current material state, such as the carbon concentration in the remaining austenite, the variation of the Ms, the variation of the rate of transformation parameter, etc. The model also has the benefit of calculating the instantaneous fractions of martensite, allowing proper predictions for anisothermal coolings.

As for the mechanical field, a complete methodology for the determination of the thermo-mechanical properties of the investigated steel grade was showcased. Mechanical measurements were carried out using the thermo-mechanical simulator Gleeble 3800. The thermo-mechanical properties extracted for austenite are the Young's modulus, the viscous stress, the kinematic hardening stress, the isotropic hardening stress and the mathematical yield stress, which serve to build an elasto-viscoplastic model. Regarding martensite and the nature of the quench process, an elasto-plastic model was planned, requiring only the determination of the Young's modulus, the isotropic hardening stress and the mathematical stress. Equations were provided to extrapolate the extracted parameters of austenite to lower temperatures.

Finally, the TRIP parameter was successfully identified with loadings in tension and in compression for 2 distinct cooling rates. The results showed a difference which is related to the cooling rate, in consequence related to the phase transformation.

RECOMMENDATIONS

While the present project provides accurate models for the prediction of distortions in a quenching process, additional improvements can be added in order to extend the prediction capabilities to welding and tempering processes. Moreover, the deceleration observed in the kinetics of martensite transformation was based on the proposition that carbon diffusion could occur during transformation. Although the mechanism of auto-tempering has been well acknowledged in the literature, further assessment should be conducted.

- Identification of the carbon enrichment in austenite via atom probe tomography. With this state-of-the-art instrument, chemical composition measurements near the atomic resolution are made possible for surface and in-depth analysis. The results will provide quantitative information regarding the enrichment of carbon in the retained austenite, validating the effect of carbon diffusion during auto-tempering.

- While the equation, Eq.(4.6), describing the increase in carbon concentration for austenite suffices for a quenching process, its limitation is noticed for general heat treatment processes. The increase in concentration never ceases for longer cooling durations or during isothermal holding. This can be addressed with the addition of an equilibrium equation with respect to time or chemical concentration between martensite and austenite.

- Isothermal martensitic phase transformation has been documented in literature. It has been a source of arguments in which other researchers suggested it was a bainitic transformation instead. Regardless of the phase transformed, the increase in dilatation measured during isothermal transformation between the Ms and the Mf should be implemented to the existing model. The routine could also be complemented with the inclusion of a kinetics of bainite transformation model.

- Carbon was the only element used to describe the deceleration in the observed kinetics. It may be the most important element, but other elements such as the Mn, Ni, Cr and Mo have frequently been included in empirical modeling for the evolution of the Ms and the rate of transformation parameter.

- The implementation of an elasto-viscoplastic model for martensite will allow for a simulation on welding processes. Moreover, as the TRIP effect is related to phase transformation, its influence with a two-stage transformation should be investigated by using various cooling rates under Ms with different applied loads. This may however require a very high number of specimens.

ANNEX I

MATHEMATICAL MODELING OF THE STRAIN RATES FROM PHASE TRANSFORMATION

AI.1 Introduction

The austenite to martensite phase transformation can be expressed in terms of strain and subsequently, strain rates. Once the kinetics of martensite transformation have been determined, the strain can be attributed to the volumetric difference of both phases (Lement, 1959; Strangwood, 2012). This strain can be calculated from the same set of dilatometry curves previously used. In reality, the real volume change due to phase transformation cannot be obtained by dilatometry as the dilatation only measures the longitudinal changes. Therefore, the volume change is estimated by the one-dimensional length change instead.

This section follows and complements the modeling on the phase transformation. Ultimately, the prediction of distortions relies on the prediction of displacements, strain and strain rates, the modeled kinetics of martensite transformation should therefore be converted.

AI.2 Constitutive Equations

The lever rule was previously used to determine fractions of martensite transformed based on the measured dilatation during cooling. With the total length of the sample known, it can be rearranged in terms of strain as a function of the phase fractions and the thermal strains of austenite and martensite, as shown in Eq.(AI.1), where the indices *a* and *m* represent the phases, austenite and martensite, respectively.

$$\varepsilon = f_m \, \varepsilon_m + (1 - f_m) \, \varepsilon_a \tag{AI.1}$$

The derivative of the previous equation is shown in Eq.(AI.2), where $\varepsilon_{a\to m}$ is a constant and representing the strain due to volume increase for the decomposition of austenite into martensite. f_m and $\dot{f}_m$ represents the fraction of martensite and the rate of transformation, which are calculated previously from the proposed routine.

$$\dot{\varepsilon} = (f_m\, \dot{\varepsilon}_m) + \big((1 - f_m)\, \dot{\varepsilon}_a\big) + \dot{f}_m\, \varepsilon_{a\to m} \tag{AI.2}$$

Additionally, the thermal expansion rate, $\dot{\varepsilon}$, of both phases is required and can be calculated using Eq.(AI.3). $\alpha_{a/m}$ represents the CLTE for austenite or martensite. T_{ref} is the reference temperature, set at 25 °C for the room temperature.

$$\dot{\varepsilon}_{a/m} = \left[\alpha_{a/m} + \frac{\mathrm{d}\alpha_{a/m}}{\mathrm{d}T}\big(T - T_{ref}\big)\right]\dot{T} \tag{AI.3}$$

The values of $\alpha_{a/m}$ and $\frac{d\alpha_{a/m}}{dT}$ can be obtained from the work of Romain Alcaras for the exact same steel (Alcaras, 2020). The values are shown in Table AI.1. They were acquired using dilatometry tests with constant CRs of -50, -8 and -1 °C/s from the austenitization temperature. The values in the table are an average from these three tests. Moreover, the assumption of a constant CLTE for both phases has not been made, hence the usage of $\frac{\mathrm{d}\alpha_{a/m}}{\mathrm{d}T}$ in the formulation.

Table AI.1 Values of CLTE for austenite and martensite
Adapted from Alcaras (2020, p. 121)

	α ($°C^{-1}$)	$\mathrm{d}\alpha/\mathrm{d}T$ ($°C^{-2}$)
Austenite	2.52E-05	-1.69E-09
Martensite	6.80E-06	-1.10E-08

AI.3 Results

The same dilatometry results of chapter 4 are shown as a function time in Figure AI.1. As a reminder, the CRs are: -2.5 °Cs^{-1}, -0.6 °C s^{-1}, -0.3 °C s^{-1} and -0.2 °C s^{-1}. The time scale has been adjusted to the temperature of 300 °C for better visualization. This does not affect the determination of the strain rates experimentally.

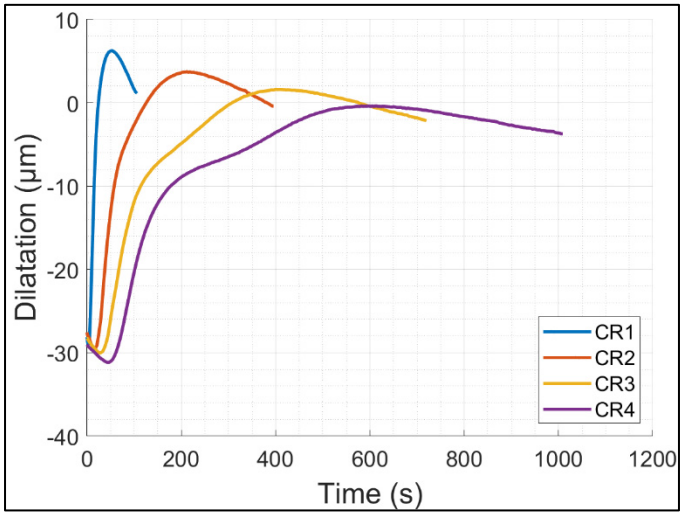

Figure AI.1 Measured dilatation from dilatometry in respect to time for the determination of the experimental strain rates

With the previously extracted kinetics of martensite transformation for each CR, the model undergoes another optimisation process for the determination of the strain from phase volume change, $\varepsilon_{a\to m}$. The determine value is of 0.00523 or 0.523%. Figure AI.2 shows the strain rates for each CR, calculated experimentally, and modeled using the kinetics of martensite transformation along with Eq.(AI.2).

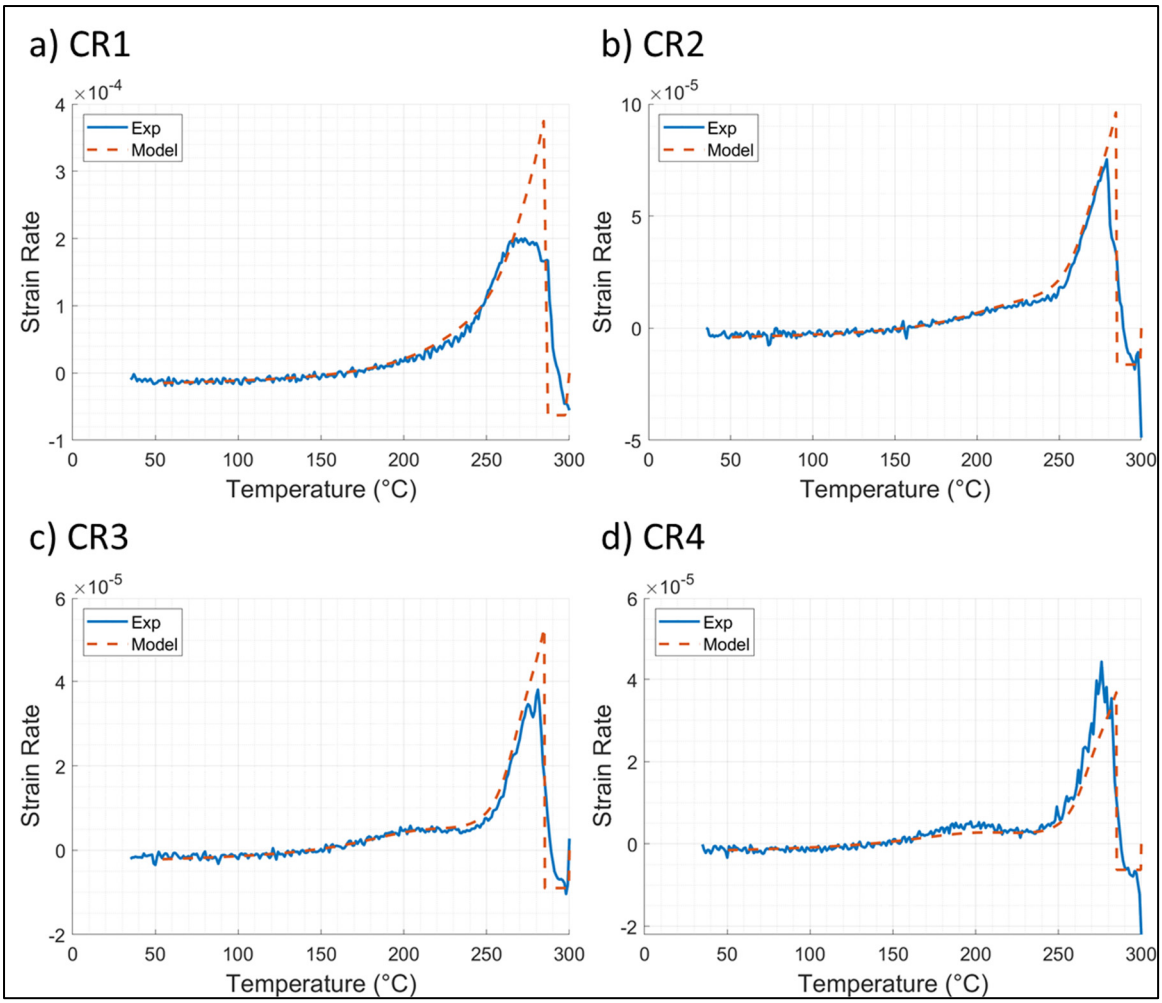

Figure AI.2 Comparison of the calculated strain rates from dilatometry and the strain rates modeled from the kinetics of martensite transformation

AI.4 Discussion and Conclusion

The strain rates from phase transformation can obtained via the lever rule from a set of dilatometry curves. The prediction of the strain rates is fairly accurate for the most part. The initial predicted strain rate due to phase transformation is rather high in comparison to the experimental. This difference is related to the usage of K-M equation where the onset of transformation cannot be accurately predicted.

The strain due to volume change was determined to be 0.523% which is consistent with the findings of Ref. (Strangwood, 2012). They suggested an increase of 0.55% instead. It is important to mention this strain, although associated with volume change during phase transformation, does not correspond to the real volume change. This is due to the missing measurement of the radius change during dilatometry tests. Moreover, the measured strain is considered as a constant for simplification purposes whereas a more appropriate strain would be dependent on the temperature.

LIST OF REFERENCES

Abrassart, F. (1972). *Influence des transformations martensitiques sur les propriétés mécaniques des alliages du système FE-NI-CR-C.* Université de Nancy, Nancy.

Advner, S. H. (2008). Chapter 8 - The Heat Treatment of Steel. In *Introduction to physical metallurgy* (pp. 249-386): Tata Mcgraw Hill.

Ahmed, R., Barrett, P. R., & Hassan, T. (2016). Unified viscoplasticity modeling for isothermal low-cycle fatigue and fatigue-creep stress–strain responses of Haynes 230. *International Journal of Solids and Structures, 88-89*, 131-145.

Alberg, H. (2003). *Material modelling for simulation of heat treatment.* Luleå tekniska universitet, Lulea.

Alcaras, R. (2020). *Influence des paramètres de trempe sur l'évolution des propriétés thermo-physiques de l'acier 300M.* École de technologie supérieure, Montréal.

Altenbach, H., Naumenko, K., & Gorash, Y. (2008). *Creep analysis for a wide stress range based on stress relaxation experiments.* Paper presented at the 9th AEPA 2008 - Engineering Plasticity and it's Applications - From Nanoscale to Macroscale, 20-24 Oct. 2008, Singapore, Singapore.

American Society for Metals. (1977). *Atlas of isothermal transformation and cooling transformation diagrams*. Metals Park, Ohio.

Ashraf, Q. J., Prasad Reddy, G. V., Sandhya, R., Laha, K., & Harmain, G. A. (2018). Simulation of low cycle fatigue stress-strain response in 316LN stainless steel using non-linear isotropic kinematic hardening model-A comparison of different approaches. *Fatigue & Fracture of Engineering Materials & Structures, 41*(2), 336-347. doi:10.1111/ffe.12683

ASTM. (2013). *ASTM E975-13 : standard practice for X-Ray determination of retained austenite in steel with near random crystallographic orientation*. Philadelphia, Pennsylvania: ASTM.

Avrami, M. (1939). Kinetics of Phase Change. I General Theory. *The Journal of Chemical Physics The Journal of Chemical Physics, 7*(12), 1103-1112.

Barralis, J. C., Louis, & Maeder, G. (1999). *Précontraintes et traitements superficiels*. Techniques de l'ingénieur

Barrett, P. R., & Hassan, T. (2020). A unified constitutive model in simulating creep strains in addition to fatigue responses of Haynes 230. *International Journal of Solids and Structures, 185-186*, 394-409.

Bhadeshia, H. (2013). Multiple, Simultaneous, Martensitic Transformations: Implications on Transformation Texture Intensities. *Materials Science Forum, 762*, 9-13.

Bhadeshia, H. (2015). Chapter 1 - Introduction. In *Bainite in steels : theory and practice* (pp. 1-15). Leeds: Maney Publishing : The Institute of Materials, Minerals and Mining.

Bhadeshia, H., & Honeycombe, R. (2006). Chapter 5 - Formation of Martensite. In *Steels: Microstructure and Properties* (pp. 95-127). Amsterdam: Elsevier Ltd.

Bhadeshia, H., & Honeycombe, R. (2017). Chapter 1 - Iron and Its Interstitial Solutions. In H. Bhadeshia & R. Honeycombe (Eds.), *Steels: Microstructure and Properties (Fourth Edition)* (pp. 1-22): Butterworth-Heinemann.

Bojack, A., Zhao, L., Morris, P. F., & Sietsma, J. (2012). In-situ determination of austenite and martensite formation in 13Cr6Ni2Mo supermartensitic stainless steel. *Materials Characterization, 71*, 77-86.

Brachet, J. C., Gavard, L., Boussidan, C., Lepoittevin, C., Denis, S., & Servant, C. (1998). Modelling of phase transformations occurring in low activation martensitic steels. *Journal of Nuclear Materials, 258-263*, 1307-1311.

Bubnoff, D. V., Carvalho, M. M. O., de Castro, J. A., & Lourenço, T. R. M. (2016). Kinetic Study on Martensite Formation in Steels 1045 and 4340 under Variable Cooling Rates. *Materials Science Forum, 869*, 550-555.

Caballero, F. G., Álvarez, L. F., Capdevila, C., & García de Andrés, C. (2003). The origin of splitting phenomena in the martensitic transformation of stainless steels. *Scripta Materialia, 49*(4), 315-320.

Caballero, F. G., Miller, M. K., Garcia-Mateo, C., & Cornide, J. (2013). New experimental evidence of the diffusionless transformation nature of bainite. *Journal of Alloys and Compounds, 577*, S626-S630.

Capdevila, C., Caballero, F. G., & García De Andrés, C. (2013). Analysis of effect of alloying elements on martensite start temperature of steels. *Materials Science and Technology, 19*(5), 581-586.

Carlone, P., Palazzo, G. S., & Pasquino, R. (2010). Finite element analysis of the steel quenching process: Temperature field and solid–solid phase change. *Computers & Mathematics with Applications, 59*(1), 585-594. doi:10.1016/j.camwa.2009.06.006

Celada-Casero, C., Sietsma, J., & Santofimia, M. J. (2019). The role of the austenite grain size in the martensitic transformation in low carbon steels. *Materials & Design, 167*, 107625. doi:10.1016/j.matdes.2019.107625

Chen, R. C., Hong, C., Li, J. J., Zheng, Z. Z., & Li, P. C. (2017). Austenite grain growth and grain size distribution in isothermal heat-treatment of 300M steel. *PROENG Procedia Engineering, 207*, 663-668.

Chen, W., & Feng, M. (2015). A study of a cyclic viscoplasticity model based on hyperbolic sine form for the inelastic strain rate. *International Journal of Mechanical Sciences, 101-102*, 155-160. doi:10.1016/j.ijmecsci.2015.07.028

Chipman, J. (1972). Thermodynamics and phase diagram of the Fe-C system. *MT Metallurgical and Materials Transactions B, 3*(1), 55-64.

Clarke, A. J., Miller, M. K., Field, R. D., Coughlin, D. R., Gibbs, P. J., Clarke, K. D., . . . Krauss, G. (2014). Atomic and nanoscale chemical and structural changes in quenched and tempered 4340 steel. *Acta Materialia, 77*, 17-27. doi:10.1016/j.actamat.2014.05.032

Conde, F. F., Escobar, J. D., Oliveira, J. P., Jardini, A. L., Bose Filho, W. W., & Avila, J. A. (2019). Austenite reversion kinetics and stability during tempering of an additively manufactured maraging 300 steel. *Additive Manufacturing, 29*. doi:10.1016/j.addma.2019.100804

da Silva, A. D., Pedrosa, T. A., Gonzalez-Mendez, J. L., Jiang, X., Cetlin, P. R., & Altan, T. (2012). Distortion in quenching an AISI 4140 C-ring – Predictions and experiments. *Materials & Design, 42*, 55-61. doi:10.1016/j.matdes.2012.05.031

de Oliveira, W. P., Savi, M. A., Pacheco, P. M. C. L., & de Souza, L. F. G. (2010). Thermomechanical analysis of steel cylinders quenching using a constitutive model with diffusional and non-diffusional phase transformations. *Mechanics of Materials, 42*(1), 31-43. doi:10.1016/j.mechmat.2009.09.006

Deng, X., & Ju, D. (2013). Modeling and Simulation of Quenching and Tempering Process in steels. *Physics Procedia, 50*, 368-374. doi:10.1016/j.phpro.2013.11.057

Denis, S. (1996). *Considering stress-phase transformation interactions in the calculation of heat treatment residual stresses.* Paper presented at the MECAMAT '95 International Seminar on Mechanics and Mechanisms of Solid-Solid Phase Transformations, 16-19 May 1995, France.

Denis, S. (1997). Prévision des contraintes résiduelles induites par traitement thermique et thermochimique. *Revue de Métallurgie, 94*(2), 157-176. doi:10.1051/metal/199794020157

Dong, P., Song, S., & Zhang, J. (2014). Analysis of residual stress relief mechanisms in post-weld heat treatment. *International Journal of Pressure Vessels and Piping, 122*, 6-14. doi:10.1016/j.ijpvp.2014.06.002

Dynamic Systems. (2023). GLEEBLE 3800-GTC. Retrieved from https://www.gleeble.com/products/gleeble-systems/gleeble-3800.html

Escobar, J. D., Faria, G. A., Maia, E. L., Oliveira, J. P., Boll, T., Seils, S., . . . Ramirez, A. J. (2019). Fundamentals of isothermal austenite reversion in a Ti-stabilized 12Cr – 6 Ni – 2 Mo super martensitic stainless steel: Thermodynamics versus experimental assessments. *Acta Materialia, 174*, 246-259. doi:10.1016/j.actamat.2019.05.026

Escobar, J. D., Faria, G. A., Wu, L., Oliveira, J. P., Mei, P. R., & Ramirez, A. J. (2017). Austenite reversion kinetics and stability during tempering of a Ti-stabilized supermartensitic stainless steel: Correlative in situ synchrotron x-ray diffraction and dilatometry. *Acta Materialia, 138*, 92-99. doi:10.1016/j.actamat.2017.07.036

Fanfoni, M., & Tomellini, M. (1998). The Johnson-Mehl-Avrami-Kolmogorov model: A brief review. *NUOVO CIMENTO- SOCIETA ITALIANA DI FISICA SEZIONE D, 20*(7/8), 1171-1182.

Fernandes, F. M. B., Denis, S., & Simon, A. (1985). Mathematical model coupling phase transformation and temperature evolution during quenching of steels. *Materials Science and Technology Materials Science and Technology, 1*(10), 838-844.

Fielding, L. C. D. (2013). The Bainite Controversy. *Materials Science and Technology, 29*(4), 383-399. doi:10.1179/1743284712y.0000000157

Firrao, D., Matteis, P., & De Sario, A. (2019). Exploring the low temperature tempering range of low alloy quenched and tempered steels. *Procedia Structural Integrity, 18*, 703-710.

Fischer, F. D., & Schlögl, S. M. (1995). The influence of material anisotropy on transformation induced plasticity in steel subject to martensitic transformation. *Mechanics of Materials, 21*(1), 1-23.

Flower, H. M. (2013). Design requirements for aerospace structural materials. In *High Performance Materials in Aerospace* (pp. 1-48): Springer Verlag.

Franz, C., Besserdich, G., Schulze, V., Müller, H., & Löhe, D. (2005). Influence of Transformation Plasticity on Residual Stresses and Distortions due to the Heat Treatment of Steels with Different Carbon Content. *Materials Science Forum, 490-491*, 47-52.

Fredj, E. B., Nanesa, H. G., Shahriari, D., Morin, J.-B., & Jahazi, M. (2017). Effect of Cooling Rate on Phase Transformation and Microstructure Evolution in a Large Size Forged Ingot of Medium Carbon Low Alloy Steel. *TMS 2017 146th Annual Meeting & Exhibition Supplemental Proceedings*, 413-423.

Frenzel, J., Wieczorek, A., Opahle, I., Maaß, B., Drautz, R., & Eggeler, G. (2015). On the effect of alloy composition on martensite start temperatures and latent heats in Ni–Ti-based shape memory alloys. *Acta Materialia, 90*, 213-231. doi:10.1016/j.actamat.2015.02.029

García de Andrés, C., Caballero, F. G., Capdevila, C., & Álvarez, L. F. (2002). Application of dilatometric analysis to the study of solid–solid phase transformations in steels. *Materials Characterization, 48*, 101-111. doi:https://doi.org/10.1016/S1044-5803(02)00259-0

Graf, M., Kuntz, M., Autenrieth, H., & Müller, R. (2020). Investigation of Size Effects Due to Different Cooling Rates of As-Quenched Martensite Microstructures in a Low-Alloy Steel. *Applied Sciences, 10*(15). doi:10.3390/app10155395

Grajcar, A., Morawiec, M., Jimenez, J. A., & Garcia-Mateo, C. (2020). Dilatometric and Microstructural Study of Martensite Tempering in 4% Mn Steel. *Materials (Basel), 13*(19). doi:10.3390/ma13194442

Greenwood, G. W., & Johnson, R. H. (1965). The deformation of metals under small stresses during phase transformations. *Proceedings of the Royal Society of London, Series A (Mathematical and Physical Sciences), 293*(1394), 403-422.

Guo, Y. B., Sui, G. F., Liu, Y. C., Chen, Y., & Zhang, D. T. (2015). Phase transformation mechanism of low-carbon high strength low alloy steel upon continuous cooling. *Materials Research Innovations, 19*, S8-416-S418-422. doi:10.1179/1432891715z.0000000001712

Guo, Z., Saunders, N., Miodownik, P., & Schille, J. P. (2009). Modelling phase transformations and material properties critical to the prediction of distortion during the heat treatment of steels. *Int. J. Microstruct. Mater. Prop. International Journal of Microstructure and Materials Properties, 4*(2), 187-195.

Gür, C. H., & Şimşir, C. (2012). Simulation of Quenching: A Review. *Materials Performance and Characterization, 1*, 1-37. doi:10.1520/mpc104479

Gür, C. H., & Tekkaya, A. E. (1998). NUMERICAL AND EXPERIMENTAL ANALYSIS OF QUENCH INDUCED STRESSES AND MICROSTRUCTURES. *9*(4), 237-256. doi:doi:10.1515/JMBM.1998.9.4.237

Gyhlesten Back, J., & Engberg, G. (2017). Investigation of Parent Austenite Grains from Martensite Structure Using EBSD in a Wear Resistant Steel. *Materials (Basel), 10*(5). doi:10.3390/ma10050453

Hai, L., Wang, Y., Ban, H., Li, G., & Du, X. (2023). A simplified prediction method on Chaboche isotropic/kinematic hardening model parameters of structural steels. *Journal of Building Engineering, 68*. doi:10.1016/j.jobe.2023.106151

HajyAkbary, F., Sietsma, J., Miyamoto, G., Furuhara, T., & Santofimia, M. J. (2016). Interaction of carbon partitioning, carbide precipitation and bainite formation during the Q&P process in a low C steel. *Acta Materialia, 104*, 72-83. doi:10.1016/j.actamat.2015.11.032

Hamada, S., Sasaki, D., Ueda, M., & Noguchi, H. (2011). *Fatigue limit evaluation considering crack initiation for lamellar pearlitic steel.* Paper presented at the 11th International Conference on the Mechanical Behavior of Materials, ICM11, Como, Italy.

Hasan, H. S. (2009). *Evaluation of Heat Transfer Coefficient during Quenching of Steels.* University of Technology, Baghdad, Iraq.

Hossain, S., Stuhr, U., Robinson, J. S., & Truman, C. E. (2021). Validating quench stresses in complex aluminium components. *The International Journal of Advanced Manufacturing Technology, 113*(11-12), 3555-3567. doi:10.1007/s00170-021-06831-y

Hsu, T. Y. (1995). Carbon Diffusion and Kinetics During the Lath Martensite Formation. *Le Journal de Physique IV, 05*, C8-351-354. doi:10.1051/jp4:1995851

Huyan, F., Hedström, P., & Borgenstam, A. (2015). Modelling of the Fraction of Martensite in Low-alloy Steels. *Materials Today: Proceedings, 2*, S561-S564. doi:10.1016/j.matpr.2015.07.347

Incropera, F. P., Bergman, T. L., DeWitt, D. P., Lavine, A., Seetharamu, K. N., & Seetharam, T. R. (2011). Chapter 1 - Introduction. In *Fundamentals of heat and mass transfer* (pp. 1-42): Wiley.

Inoue, T., & Tanaka, K. (1975). An elastic-plastic stress analysis of quenching when considering a transformation. *International Journal of Mechanical Sciences, 17*(5), 361-367. doi:https://doi.org/10.1016/0020-7403(75)90028-4

Inoue, T., & Wang, Z. G. (1986, 1986//). *Coupling between Temperature, Stress and Metallic Structures during Phase Transformation and the Analysis of Carburized Quenching of a Steel Gear.* Paper presented at the Computational Mechanics '86, Tokyo.

Isasti, N., Jorge-Badiola, D., Taheri, M. L., & Uranga, P. (2013). Phase Transformation Study in Nb-Mo Microalloyed Steels Using Dilatometry and EBSD Quantification. *Metallurgical and Materials Transactions A, 44*, 3552-3563. doi:10.1007/s11661-013-1738-3

James, J. D., Spittle, J. A., Brown, S. G. R., & Evans, R. W. (2001). A review of measurement techniques for the thermal expansion coefficient of metals and alloys at elevated temperatures. *Measurement Science and Technology, 12*(3), R1-R15.

Jung, M., Lee, S.-J., Lee, W.-B., & Moon, K. I. (2018). Finite Element Simulation and Optimization of Gas-Quenching Process for Tool Steels. *Journal of Materials Engineering and Performance, 27*, 4355-4363. doi:10.1007/s11665-018-3492-6

Jung, M., Lee, S.-J., & Lee, Y.-K. (2009). Microstructural and Dilatational Changes during Tempering and Tempering Kinetics in Martensitic Medium-Carbon Steel. *Metallurgical and Materials Transactions A, 40*, 551-559. doi:10.1007/s11661-008-9756-2

Kaar, S., Krizan, D., Schneider, R., & Sommitsch, C. (2022). On competing reactions and austenite stabilization: Advanced model for exact microstructural prediction in Q&P steels with elevated Mn-content. *Materialia, 26*. doi:10.1016/j.mtla.2022.101584

Kang, S. H., & Im, Y. T. (2007). Thermo-elasto-plastic finite element analysis of quenching process of carbon steel. *Journal of Materials Processing Technology, 192-193*, 381-390. doi:10.1016/j.jmatprotec.2007.04.101

Kardoulaki, E., Lin, J., Balint, D., & Farrugia, D. (2014). Investigation of the effects of thermal gradients present in Gleeble high-temperature tensile tests on the strain state for free cutting steel. *Journal of Strain Analysis for Engineering Design, 49*(7), 521-532. doi:10.1177/0309324714531950

Kawaragi, Y., Fukumoto, M., & Okamura, K. (2015). Effect of implicit integration scheme in residual stress analysis of quenching considering transformation plasticity and kinematic hardening. *Zairyo/Journal of the Society of Materials Science, Japan, 64*(4), 258-265. doi:10.2472/jsms.64.258

Khan, S. A., & Bhadeshia, H. K. D. (1990). Kinetics of Martensitic transformation in partially bainitic 300M steel. *Materials Science & Engineering A, 129*(2), 257-272.

Kim, B., Sietsma, J., & Santofimia, M. J. (2017). The role of silicon in carbon partitioning processes in martensite/austenite microstructures. *Materials & Design, 127*, 336-345. doi:10.1016/j.matdes.2017.04.080

Kohne, T., Dahlstrom, A., Winkelmann, A., Hedstrom, P., & Borgenstam, A. (2022). Correlation of Heterogeneous Local Martensite Tetragonality and Carbon Distribution in High Carbon Steel. *Materials (Basel), 15*(19). doi:10.3390/ma15196653

Kohne, T., Fahlkrans, J., Stormvinter, A., Maawad, E., Winkelmann, A., Hedström, P., & Borgenstam, A. (2023). Evolution of Martensite Tetragonality in High-Carbon Steels Revealed by In Situ High-Energy X-Ray Diffraction. *Metallurgical and Materials Transactions A*. doi:10.1007/s11661-022-06948-z

Koistinen, D. P., & Marburger, R. E. (1959). A general equation prescribing the extent of the austenite-martensite transformation in pure iron-carbon alloys and plain carbon steels. *Acta Metallurgica, 7*, 59-60. doi:https://doi.org/10.1016/0001-6160(59)90170-1

Krauss, G., & Marder, A. R. (1971). The morphology of martensite in iron alloys. *Metallurgical Transaction Metallurgical Transactions, 2*(9), 2343-2357.

Krempl, E., & Lu, H. (1984). The rate(time)-dependence of ductile fracture at room temperature. *Engineering Fracture Mechanics, 20*(4), 629-632.

Leblond, J. B., & Devaux, J. (1984). A new kinetic model for anisothermal metallurgical transformations in steels including effect of austenite grain size. *Acta Metallurgica, 32*(1), 137-146. doi:https://doi.org/10.1016/0001-6160(84)90211-6

Leblond, J. B., Devaux, J., & Devaux, J. C. (1989). Mathematical modelling of transformation plasticity in steels I: Case of ideal-plastic phases. *International Journal of Plasticity, 5*(6), 551-572. doi:https://doi.org/10.1016/0749-6419(89)90001-6

Leblond, J. B., Mottet, G., & Devaux, J. C. (1986a). A theoretical and numerical approach to the plastic behaviour of steels during phase transformations—I. Derivation of general relations. *Journal of the Mechanics and Physics of Solids, 34*(4), 395-409. doi:https://doi.org/10.1016/0022-5096(86)90009-8

Leblond, J. B., Mottet, G., & Devaux, J. C. (1986b). A theoretical and numerical approach to the plastic behaviour of steels during phase transformations—II. Study of classical plasticity for ideal-plastic phases. *Journal of the Mechanics and Physics of Solids, 34*(4), 411-432. doi:https://doi.org/10.1016/0022-5096(86)90010-4

Ledbetter, H. M., Weston, W. F., & Naimon, E. R. (1975). Low-temperature elastic properties of four austenitic stainless steels. *Journal of Applied Physics, 46*(9), 3855-3860. doi:10.1063/1.322182

Lee, S.-J., & Van Tyne, C. J. (2011). A Kinetics Model for Martensite Transformation in Plain Carbon and Low-Alloyed Steels. *Metallurgical and Materials Transactions A, 43*, 422-427. doi:10.1007/s11661-011-0872-z

Lee, S. J. (2013). Evaluation of Empirical Kinetics Models of Athermal Martensite Transformation in Plain Carbon and Low Alloy Steels. *Advanced Materials Research, 798-799*, 39-44.

Leidenfrost, J. G. (1966). On the fixation of water in diverse fire. *International Journal of Heat and Mass Transfer, 9*(11), 1153-1166.

Lemaitre, J., Chaboche, J. L., Benallal, A., & Desmorat, R. (2020). Élasto-viscoplasticité. In *Mécanique des matériaux solides - 3ème édition* (pp. 261-314): Dunod.

Lement, B. S. (1959). Distortion in tool steels. In *Distortion in tool steels* (pp. 39). Metals Park, Novelty, Ohio: American Society for Metals.

Li, Y., Xu, M., Jin, Y., & Lu, H. (2015). Finite-element Simulation of Low-alloy High Strength Steel Welding Incorporating Improved Martensite Transformation Kinetics and Recrystalization Annealing. *ISIJ International, 55*, 1448-1453. doi:10.2355/isijinternational.55.1448

Li, Z.-C., & Ferguson, B. L. (2011). Computer modeling and validations of steel gear heat treatment processes using commercial software DANTE. *Journal of Shanghai Jiaotong University (Science), 16*(2), 152-156. doi:10.1007/s12204-011-1117-4

Liu, C., Huang, M., Ren, Q., Ren, Y., & Zhang, L. (2022). Effect of Grain Size and Cooling Rate on the Martensite Start Temperature of Stainless Steel. *steel research international, 93*(8). doi:10.1002/srin.202200044

Liu, C., Liu, Y., Zhang, D., & Yan, Z. (2012). Research on splitting phenomenon of isochronal martensitic transformation in T91 ferritic steel. *Phase Transitions, 85*, 461-470. doi:10.1080/01411594.2011.622903

Liu, J. H., Binot, N., Delagnes, D., & Jahazi, M. (2021). Influence of the cooling rate below Ms on the martensitic transformation in a low alloy medium-carbon steel. *Journal of Materials Research and Technology, 12*, 234-242. doi:https://doi.org/10.1016/j.jmrt.2021.02.075

Liu, L., & Guo, B. (2021). Dilatometric Analysis and Kinetics Research of Martensitic Transformation under a Temperature Gradient and Stress. *Materials (Basel), 14*(23). doi:10.3390/ma14237271

Loewy, S., Rheingans, B., Meka, S. R., & Mittemeijer, E. J. (2014). Unusual martensite-formation kinetics in steels: Observation of discontinuous transformation rates. *Acta Materialia, 64*, 93-99. doi:10.1016/j.actamat.2013.11.052

Magee, C. L., & Paxton, H. W. (1966). *Transformation kinetics, microplasticity and aging of martensite in Fe-31Ni.* Carnegie Institute of Technology, Pittsburgh, Penn.

Masoudi, S., Amirian, G., Saeedi, E., & Ahmadi, M. (2015). The Effect of Quench-Induced Residual Stresses on the Distortion of Machined Thin-Walled Parts. *Journal of Materials Engineering and Performance, 24*(10), 3933-3941. doi:10.1007/s11665-015-1695-7

Miller, A. (1976). An Inelastic Constitutive Model for Monotonic, Cyclic, and Creep Deformation: Part I—Equations Development and Analytical Procedures. *Journal of Engineering Materials and Technology, 98*(2), 97-105. doi:10.1115/1.3443367

Mondière, A. l. (2018). *Contrôle des propriétés mécaniques de l'acier Ferrium® M54® par la maîtrise de sa microstructure au cours du traitement thermique dans l'optique d'applications aéronautiques.* École des mines d'Albi-Carmaux, Albi.

Morawiec, M., Wojtacha, A., & Opiela, M. (2021). Kinetics of Austenite Phase Transformations in Newly-Developed 0.17C-2Mn-1Si-0.2Mo Forging Steel with Ti and V Microadditions. *Materials, 14*(7). doi:10.3390/ma14071698

Morgan, E. R., & Ko, T. (1953). Thermal stabilization of austenite in iron-carbon-nickel alloys. *Acta Metallurgica, 1*, 36-48. doi:https://doi.org/10.1016/0001-6160(53)90008-X

Mustak, O., Evcil, E., & Simsir, C. (2016). Simulation of through-hardening of SAE 52100 steel bearings - Part I: Determination of material properties : Simulation der Durchhärtung vom Wälzlagerstahl SAE 52100 - Teil I: Bestimmung der Materialeigenschaften. *MAWE Materialwissenschaft und Werkstofftechnik, 47*, 735-745.

Nallathambi, A. K., Kaymak, Y., Specht, E., & Bertram, A. (2008). Distortion and Residual Stresses during Metal Quenching Process. 145-157. doi:10.1007/978-3-540-85715-0_12

Nallathambi, A. K., Specht, E., Bertram, A., & Kaymak, Y. (2010). Sensitivity of material properties on distortion and residual stresses during metal quenching processes. *J Mater Process Technol Journal of Materials Processing Technology, 210*(2), 204-211.

Neubert, S., Pittner, A., & Rethmeier, M. (2016). Experimental determination of TRIP-parameter K for mild- and high-strength low-alloy steels and a super martensitic filler material. *SpringerPlus SpringerPlus, 5*(1).

Nie, Z., Wang, G., Lin, Y., & Rong, Y. (2015). Precision Measurement and Modeling of Quenching-Tempering Distortion in Low-Alloy Steel Components with Internal Threads. *Journal of Materials Engineering and Performance, 24*(12), 4878-4889. doi:10.1007/s11665-015-1789-2

Ning, D., Dai, C. R., Wu, J. L., Wang, Y. D., Wang, Y. Q., Jing, Y., & Sun, J. (2021). Carbide precipitation and coarsening kinetics in low carbon and low alloy steel during quenching and subsequently tempering. *Materials Characterization, 176*. doi:10.1016/j.matchar.2021.111111

Norton, F. H. (1929). Chapter 8 - Discussion of Results. In *The Creep of Steel at High Temperatures* (pp. 67-70). New York: McGraw-Hill book Company, Incorporated.

Obasi, G., Pickering, E. J., Vasileiou, A. N., Sun, Y. L., Rathod, D., Preuss, M., . . . Smith, M. C. (2019). Measurement and Prediction of Phase Transformation Kinetics in a Nuclear Steel During Rapid Thermal Cycles. *Metallurgical and Materials Transactions A, 50*(4), 1715-1731. doi:10.1007/s11661-018-05102-y

Ooi, S. W., Cho, Y. R., Oh, J. K., & Bhadeshia, H. K. D. H. (2010). Carbon Enrichment in Residual Austenite during Martensitic. *International Conference on Martensitic Transformations (ICOMAT)*, 179-185. doi:doi:10.1002/9781118803592.ch25

Peng, F., Xu, Y., Han, D., & Gu, X. (2019). Kinetic models of multiple-stage martensite transformation and subsequent isothermal bainite formation excluding ε-carbide precipitation in intercritical quenching and partitioning steels. *Materials & Design, 183*, 108183. doi:10.1016/j.matdes.2019.108183

Pereloma, E., & V. Edmonds, D. (2012). Chapter 1 - Diffusionless Transformations. In *Phase Transformations in Steels : Diffusionless Transformations, High Strength Steels, Modelling And Advanced Analytical Techniques* (pp.1-145): Elsevier Science.

Peterli, M. N., Hora, P., & Volk, W. (2017). *Heat Treatment Simulation and Experimental Investigation of Thermal Distortion with a Special Focus on Fineblanked Parts.*

Pierce, D. T., Coughlin, D. R., Williamson, D. L., Clarke, K. D., Clarke, A. J., Speer, J. G., & De Moor, E. (2015). Characterization of transition carbides in quench and partitioned steel microstructures by Mössbauer spectroscopy and complementary techniques. *Acta Materialia, 90*, 417-430. doi:10.1016/j.actamat.2015.01.024

Pietzsch, R., Brzoza, M., Kaymak, Y., Specht, E., & Bertram, A. (2005). Minimizing the distortion of steel profiles by controlled cooling. *steel research international, 76*(5), 399-407. doi:10.1002/srin.200506028

Pietzsch, R., Brzoza, M., Kaymak, Y. i., Specht, E., & Bertram, A. (2007). Simulation of the Distortion of Long Steel Profiles During Cooling. *Journal of Applied Mechanics, 74*(3), 427. doi:10.1115/1.2338050

Pohjonen, A., Ramesh Babu, S., & Visuri, V.-V. (2022). Coupled model for carbon partitioning, diffusion, Cottrell atmosphere formation and cementite precipitation in martensite during quenching. *Computational Materials Science, 209*. doi:10.1016/j.commatsci.2022.111413

Porter, D. A., & Easterling, K. E. (2009). Chapter 6 - Diffusionless Transformations. In *Phase Transformations in Metals and Alloys* (3 ed., pp. 383-435): CRC Press, Boca Raton.

Ramezansefat, H., & Shahbeyk, S. (2015). The Chaboche hardening rule: A re-evaluation of calibration procedures and a modified rule with an evolving material parameter. *Mechanics Research Communications, 69*, 150-158. doi:10.1016/j.mechrescom.2015.08.003

Reed-Hill, R. E., & Abbaschian, R. (2009). Chapter 18 - The Iron-Carbon Alloy System. In *Physical metallurgy principles* (pp. 562-602). Boston: PWS-Kent Pub.

Ribamar, G. G., Escobar A, J. D., da Silva, A. K., Schell, N., Ávila, J. A., Nishikawa, A. S., Oliveira, J. P., Goldenstein, H. (2023). Austenite carbon enrichment and decomposition during Quenching and Tempering of high silicon high carbon bearing steel. *Acta Materialia*, 118742. doi:https://doi.org/10.1016/j.actamat.2023.118742

Roux, G., & Billardon, R. (2007). *Prévision des contraintes résiduelles induites par le soudage TIG d'un acier martensitique (X10CrMoVNb9-1).* Université Pierre et Marie Curie, Paris.

Saleh Asheghabadi, M., & Cheng, X. (2020). Analysis of Undrained Seismic Behavior of Shallow Tunnels in Soft Clay Using Nonlinear Kinematic Hardening Model. *Applied Sciences, 10*(8). doi:10.3390/app10082834

Sanchez Sarmiento, G., Gaston, A., & Totten, G. (2011). Computational modeling of heat treating processes by use of HT-mod and ABAQUS. *Lat. Am. Appl. Res. Latin American Applied Research, 41*(3), 217-224.

Schastlivtsev, V. M., Kaletina, Y. V., Fokina, E. A., & Kaletin, A. Y. (2014). Effect of cooling rate on the amount of retained austenite upon bainitic transformations. *The Physics of Metals and Metallography, 115*(10), 990-1000. doi:10.1134/s0031918x14100147

Schenk, T. (2011). *Modelling of welding distortion : the influence of clamping and sequencing.* Delft University of Technology, Delft.

Seo, E. J., Cho, L., & De Cooman, B. C. (2016). Modified Methodology for the Quench Temperature Selection in Quenching and Partitioning (Q&P) Processing of Steels. *Metallurgical and Materials Transactions A, 47*, 3797-3802. doi:10.1007/s11661-016-3579-3

Shao, W., Yi, M., Tang, J., & Sun, S. (2022). Prediction and Minimization of the Heat Treatment Induced Distortion in 8620H Steel Gear: Simulation and Experimental Verification. *Chinese Journal of Mechanical Engineering, 35*(1). doi:10.1186/s10033-022-00802-4

Simsir, C. (2017). Transformation Induced Plasticity (TRIP) of SAE 52100 Steel during Martensitic and Bainitic Transformations. *Hittite Journal of Science & Engineering, 4*(2), 125-130. doi:10.17350/hjse19030000058

Şimşir, C. (2008). *3D Finite Element Simulation of Steel Quenching in Order to Determine the Microstructure and Residual Stresses.* Middle East Technical University, Ankara.

Şimşir, C. (2014). Modeling and Simulation of Steel Heat Treatment—Prediction of Microstructure, Distortion, Residual Stresses, and Cracking. *ASM Metals Handbook, Volume 4B: Steel Heat Treating Technologies*, 409-466.

Şimşir, C., & Gür, C. H. (2008). 3D FEM simulation of steel quenching and investigation of the effect of asymmetric geometry on residual stress distribution. *Journal of Materials Processing Technology, 207*(1-3), 211-221. doi:10.1016/j.jmatprotec.2007.12.074

Şimşir, C., & Gür, C. H. (2008). A FEM based framework for simulation of thermal treatments: Application to steel quenching. *Computational Materials Science, 44*(2), 588-600. doi:10.1016/j.commatsci.2008.04.021

Skobir, D. A. (2011). High-strength low-alloy (HSLA) steels. *Materiali in tehnologije*(45), 295-301.

Soffa, W. A., & Laughlin, D. E. (2014). Diffusional Phase Transformations in the Solid State. In *Physical Metallurgy* (pp. 851-1020).

Speer, J. G., De Moor, E., & Clarke, A. J. (2014). Critical Assessment 7: Quenching and partitioning. *Materials Science and Technology, 31*(1), 3-9. doi:10.1179/1743284714y.0000000628

Stormvinter, A., Borgenstam, A., & Hedström, P. (2011). Investigation of Lath and Plate Martensite in a Carbon Steel. *Solid State Phenomena, 172-174*, 61-66. doi:10.4028/www.scientific.net/SSP.172-174.61

Strangwood, M. (2012). Fundamentals of ferrite formation in steels. In *Phase Transformations in Steels* (pp. 187-224).

Suh, D.-W., Oh, C.-S., Han, H. N., & Kim, S.-J. (2007). Dilatometric Analysis of Phase Fraction during Austenite Decomposition into Banded Microstructure in Low-Carbon Steel. *Metallurgical and Materials Transactions A, 38*(12), 2963-2973. doi:10.1007/s11661-007-9361-9

Szmytka, F., Rémy, L., Maitournam, H., Köster, A., & Bourgeois, M. (2010). New flow rules in elasto-viscoplastic constitutive models for spheroidal graphite cast-iron. *International Journal of Plasticity, 26*(6), 905-924. doi:10.1016/j.ijplas.2009.11.007

TA Instruments. (2023). DIL 805A/D. Retrieved from https://www.tainstruments.com/dil-805ad/

Takahashi, M. (2004). Recent progress: kinetics of the bainite transformation in steels. *Current Opinion in Solid State and Materials Science, 8*(3-4), 213-217. doi:10.1016/j.cossms.2004.08.003

Talebi, S. H., Jahazi, M., & Melkonyan, H. (2018). Retained Austenite Decomposition and Carbide Precipitation during Isothermal Tempering of a Medium-Carbon Low-Alloy Bainitic Steel. *Materials (Basel), 11*(8). doi:10.3390/ma11081441

Tao, X., Han, L., & Gu, J. (2015). Splitting phenomenon in martensitic transformation of X12CrMoWVNbN10-1-1 steel. *International Journal of Materials Research, 106*(6), 565-571. doi:10.3139/146.111221

Telejko, I., Adrian, H., & Guzik, B. (2013). High Temperature Brittleness of Cast Alloys / Kruchosc Wysokotemperaturowa Stopów Odlewniczych. *Archives of Metallurgy and Materials, 58*(1), 83-87. doi:10.2478/v10172-012-0155-8

Terborg, R., Kaeppel, A., Yu, B., Patzschke, M., Salge, T., & Falke, M. (2017). Advanced Chemical Analysis Using an Annular Four-Channel Silicon Drift Detector. *Microscopy Today, 25*(2), 30-35. doi:10.1017/s1551929517000141

Thibaux, P., Métenier, A., & Xhoffer, C. (2007). Carbon Diffusion Measurement in Austenite in the Temperature Range 500 °C to 900 °C. *Metallurgical and Materials Transactions A, 38*, 1169-1176. doi:10.1007/s11661-007-9150-5

Toji, Y., Miyamoto, G., & Raabe, D. (2015). Carbon partitioning during quenching and partitioning heat treatment accompanied by carbide precipitation. *Acta Materialia, 86*, 137-147. doi:10.1016/j.actamat.2014.11.049

Totten, G. E. (2007). Chapter 10 - Distortion of Heat-Treated Components. In D. o. H.-T. Components (Ed.), *Steel heat treatment handbook* (pp. 614-648). Boca Raton, FL: Taylor & Francis.

van Bohemen, S. M. C. (2013). Bainite and martensite start temperature calculated with exponential carbon dependence. *Materials Science and Technology, 28*(4), 487-495. doi:10.1179/1743284711y.0000000097

van Bohemen, S. M. C., & Sietsma, J. (2010). The kinetics of bainite and martensite formation in steels during cooling. *Materials Science and Engineering: A, 527*, 6672-6676. doi:10.1016/j.msea.2010.06.091

van Bohemen, S. M. C., & Sietsma, J. (2013). Effect of composition on kinetics of athermal martensite formation in plain carbon steels. *Materials Science and Technology, 25*, 1009-1012. doi:10.1179/174328408x365838

van Bohemen, S. M. C., & Sietsma, J. (2014). Kinetics of martensite formation in plain carbon steels: critical assessment of possible influence of austenite grain boundaries and autocatalysis. *Materials Science and Technology, 30*, 1024-1033. doi:10.1179/1743284714y.0000000532

Vander Voort, G. (2001). Microstructure of Ferrous Alloys. *68*, 28-34. doi:10.1201/9781420030365.ch3

Vanoverberghe, L. (2008). Anticipation des déformations lors du traitement thermique de pignons de boîtes de vitesses. Retrieved from http://pastel.archives-ouvertes.fr/pastel-00004771

Villa, M., Pantleon, K., Reich, M., Kessler, O., & Somers, M. A. J. (2014). Kinetics of anomalous multi-step formation of lath martensite in steel. *Acta Materialia, 80*, 468-477. doi:10.1016/j.actamat.2014.08.031

Wang, J., & Van Der Zwaag, S. (2001). Stabilization mechanisms of retained austenite in transformation-induced plasticity steel. *Metall and Mat Trans A Metallurgical and Materials Transactions A, 32*(6), 1527-1539.

Wang, W.-y., Liu, B., & Kodur, V. (2013). Effect of Temperature on Strength and Elastic Modulus of High-Strength Steel. *Journal of Materials in Civil Engineering, 25*(2), 174-182. doi:10.1061/(asce)mt.1943-5533.0000600

Wölfle, C. H., Krempaszky, C., & Werner, E. (2021). An implicit integration scheme with consistent tangent modulus for Leblond's model of transformation-induced plasticity in steels. *Continuum Mechanics and Thermodynamics, 34*(1), 321-340. doi:10.1007/s00161-021-01058-4

Xiao, H., Fan, X. G., Zhan, M., Liu, B. C., & Zhang, Z. Q. (2021). Flow stress correction for hot compression of titanium alloys considering temperature gradient induced heterogeneous deformation. *Journal of Materials Processing Technology, 288*. doi:10.1016/j.jmatprotec.2020.116868

Yang, H., & Bhadeshia, H. (2009). Austenite grain size and the martensite-start temperature. *Scripta Materialia, 60*(7), 493-495. doi:10.1016/j.scriptamat.2008.11.043

Yang, Z., Liu, Z., He, X., Qiao, S., & Xie, C. (2018). Effect of microstructure on the impact toughness and temper embrittlement of SA508Gr.4N steel for advanced pressure vessel materials. *Sci Rep, 8*(1), 207. doi:10.1038/s41598-017-18434-3

Yi, H. L., Lee, K. Y., & Bhadeshia, H. K. D. H. (2011). Mechanical stabilisation of retained austenite in -TRIP steel. *Materials Science and Engineering: A Materials Science and Engineering: A, 528*(18), 5900-5903.

Zhang, S.-L., & Xuan, F.-Z. (2017). Interaction of cyclic softening and stress relaxation of 9–12% Cr steel under strain-controlled fatigue-creep condition: Experimental and modeling. *International Journal of Plasticity, 98*, 45-64. doi:10.1016/j.ijplas.2017.06.007

Zhang, Y., Gu, J., Han, L., Shen, G., & Li, C. (2021). Thermal decomposition characteristics of retained austenite and its influence on impact toughness of B-containing 9Cr1Mo1Co(FB2) steel during the two-step tempering. *Journal of Materials Research and Technology, 12*, 2462-2475. doi:10.1016/j.jmrt.2021.03.105

Zhu, C., Xiong, X. Y., Cerezo, A., Hardwicke, R., Krauss, G., & Smith, G. D. (2007). Three-dimensional atom probe characterization of alloy element partitioning in cementite during tempering of alloy steel. *Ultramicroscopy, 107*(9), 808-812. doi:10.1016/j.ultramic.2007.02.033